Refining Limits on the Electron EDM Using Polycrystalline GdIG

Alexander W. Bridges

Advisor: Larry R. Hunter

Submitted to the Department of Physics of Amherst College
in partial fulfillment of the requirements for the degree
of Bachelor of Arts with honors.

Submitted April 30, 2007

Contents

Introduction

This thesis is the fourth describing a recent effort to measure the electron electric dipole moment (EDM) using a large, polycrystalline sample of gadolinium iron garnet. The experiment began in 2002 under the direction of Professor Larry Hunter, with Noah Charney as the first thesis student. Oliver Elliott took up the reins the next year, and Ben Heidenreich two years thereafter.

The experiment has set an upper limit on the magnitude of the electron EDM of $|d_e| < 1.5 \times 10^{-24}$ e cm, which is almost a factor of four lower than the previously reported limit [1, 2]. Our sensitivity has been limited by the presence of a large signal that is symmetric upon reversal of the sample magnetization. This thesis describes recent efforts to understand this systematic effect, which we refer to as the *M-Even effect*. Current results indicate that it may be related to the method of coupling electrodes to the sample, possibly resulting from relative motion between them.

Chapter 1 describes the mathematics of "discrete" symmetries and motivates our current pursuit. Chapter 2 discusses the theory of our experiment, beginning with the features of solid state EDM searches and the properties of gadolinium iron garnet. Certain points that were skimmed over elsewhere have been emphasized at length. Chapter 3 characterizes the M-even effect and discusses the methods used to obtain these data. Chapter 4 describes the miniature system that we have constructed to model the effect, along with preliminary results, and chapter 5 presents the most accurate data obtained. Chapter 6 concludes the thesis with preliminary analyses of the data.

Four appendices are included, the first of which presents a mathematical proof relevant to the field but not essential to this thesis. Appendix B describes the language of complex circuit analysis and builds to a description of the detector filter, which is new since the previous student. Appendix C overviews the design of the EDM apparatus, which should give the reader a picture of how everything physically connects. The final appendix includes the details of many experiments we performed.

Acknowledgments

Many individuals deserve thanks for contributing to this work, and there is an extraordinarily low probability that I will remember all of them. There is, on the other hand, no chance whatsoever that I will do sufficient justice to their efforts. The following list is therefore to be considered shamefully neglectful even as a minimum expression of appreciation.

The entire Amherst College Department of Physics has contributed to my education, though by circumstance some members more than others. Kannan Jagannathan has instructed me in more courses than any other professor, and if the occasional phrasing in this thesis is his (one or two come to mind), then I borrow it with pride. I hope only to have used it correctly. My academic advisor, William Loinaz, has dutifully reminded me of impending Commencement. He also helped me steer through various calculations. It is through Dan Krause Jr.'s teaching that I was able to construct the various braces described in this thesis. He also did all vacuum deposition described in this thesis, and built almost our entire apparatus.

Ben Heidenreich's work on the experiment has been tremendous, and, considering that he has graduated, surprisingly continuous. Previous thesis students were Noah Charney and Oliver Elliot, with both of whom I have become acquainted. Timothy Ripper was a Hughes fellow in the lab during the summer of 2006. He survived my endless attempts at wit, which places him among a select minority of needlessly tolerant people.

To my fellow physics majors, Amos Irwin, Dan Guest, Adam Kaplan, and Nicolaus Schmandt, I extend the warmest appreciation. We haven't survived anything unusual, but it seemed hard at the time. Among other classmates and friends, I am particularly grateful to Leslie Moclock, Joshua Levenson, Emily Cole, Sarah Jin, Marietta Jo, and Mia Yu. Their efforts have made a difficult year thrilling, which is better than any other thesis year I have heard described. David Stein, Michael Foss-Feig, and Rishidev Chaudhuri have encouraged my social degradation.

My father and mother supported me endlessly, which is precisely what they have always done. Their contributions to my life cannot be overestimated; without them this surely would have been impossible. I also wish to thank Joel Gordon for inspiring discussions and his tremendous ability to make complicated matters accessible. His logical approach can be felt throughout this thesis, and especially in chapter two. Above all I thank my advisor, Larry Hunter, for contributing most tangibly to my education.

Chapter 1

Discrete Symmetries

Symmetries find beautiful form in the laws of physics. They are mathematically rigorous and experimentally verified patterns, and provide more than aesthetic satisfaction: they are physically insightful. In this way, physical symmetries are similar to conservation laws. Both are on the one hand guiding principles helpful in formulating laws, and on the other consequences of the fundamental, dynamical equations. The formulation of physical law must not only be formed by, but also account for these relationships. Are symmetries, then, natural results or imposed boundary conditions?

The answer is probably a little bit of both, for, as we shall see, symmetry conservation is not as steadfast as once imagined. New theories are guided by a desire for increasingly high levels of symmetry, and experimental results endlessly challenge our devotion to them. The experiment described in this thesis is one such test of physical symmetry.

This chapter introduces a subset of symmetries referred to as *discrete*, and provides a basis for the discussions of later work. Symmetries have been important throughout the lifetime of physics, and so we will approach them from both classical and quantum perspectives. The former is more mathematically approachable than the latter, but both follow from the same basic principles. Symmetry violations and the general motivation for our research are discussed to close.

1.1 Discrete Symmetries in Classical Dynamics

The three discrete symmetries of physics are parity, time, and charge. They are all conserved in classical dynamics, which is to say that the original and symmetric worlds are both physically sensible – simply by looking at the worldlines of particles, we cannot tell the difference [3]. Let us examine each symmetry in turn.

1.1.1 Parity

Parity symmetry indicates that the laws of physics should be invariant under inversion of the spatial axes. In three-dimensional, Cartesian space, this amounts to reflecting a system through a plane and then rotating it 180° about the vector perpendicular to the plane. Generally speaking, this changes the "handedness" of a coordinate system [4, §4.6]. Consider the two coordinate systems in Figure 1.1, which are related by parity. The first is called "right-handed" because the sign of the cross product $\hat{\mathbf{x}} \times \hat{\mathbf{y}} = \hat{\mathbf{z}}$ is positive, in agreement with the right-hand rule. The second is "left-handed" for the opposite reason. In Cartesian space these definitions suffice, though we may generalize in three dimensions by considering the triple product $\hat{\mathbf{z}} \cdot (\hat{\mathbf{x}} \times \hat{\mathbf{y}})$. In right-handed coordinate systems the triple product is greater than zero, and in left-handed coordinate systems less than zero.

Parity takes $x_i \rightarrow -x_i$, where the x_i are spatial coordinates. This operation changes the signs of many vectors, such as position, velocity, momentum, and force. These are called *polar* vectors. Others, such as angular momentum $\mathbf{l} = \mathbf{r} \times \mathbf{p}$, preserve their signs and are known as *axial.* The same distinction can be made of scalar quantities, where *scalars* preserve their signs under parity and *pseudoscalars* change. As examples, the dot product of two polar vectors is scalar, but the dot product of a

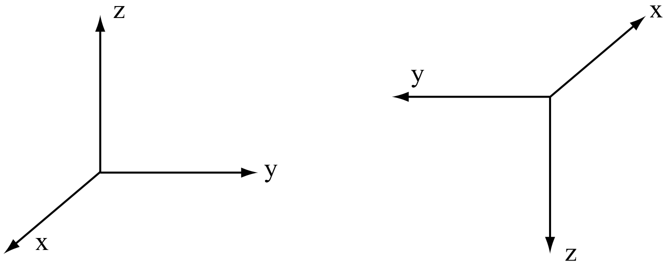

Figure 1.1: Right- and left-handed coordinate systems.

polar and an axial vector is psuedoscalar.

In order for a system to conserve parity, its vectors must change sign uniformly. This leads to an insight into classical theory: *no parity invariant theory can involve adding polar and axial vectors* [4, §4.6]. Take for example the Lorentz force law, which states

$$\mathbf{F} = q\big(\mathbf{E} + \mathbf{v} \times \mathbf{B}\big). \tag{1.1}$$

$\mathbf{E}$ is a polar vector but $\mathbf{B}$ is axial, so the two could not normally be added; however, $\mathbf{v}$ is polar and therefore $\mathbf{v} \times \mathbf{B}$ is as well. The force law of classical electromagnetism is therefore parity invariant. Gravity also is invariant under parity because its direction depends on the positions of massive bodies, whose coordinates change sign.

1.1.2 Time

Time symmetry states that the laws of physics are the same forward and backward in time. Physically this means that any process that we see occurring in one direction could also occur in reverse. This seems counter to reason; experience shows us that time certainly has an "arrow," and some events would appear ludicrous were they to occur in the opposite fashion. If physical processes are reversible, can shattered eggs miraculously reform and jump back into our hands? And if they can, why do we keep buying new ones?

Technically, this could happen. If all particles in our clumsily dropped egg were suddenly excited into precisely the opposite motion that they had before coming to rest, and all frictional and chemical energy were returned in precisely the opposite fashion to that in which it left (light, heat, sound, etc.), we would indeed have our egg once again. The likelihood of such an occurrence is incomprehensibly small, and figurative descriptions would serve only to confuse. Suffice it to say, if the reader drops an egg in his future then he is advised to find another, and not to wait for his old egg to revitalize.

But the point is that physics works forward and backward in time. The difficulties we have with the above picture are probabilistic and due to the initial conditions of a scenario [5, §2.1.2]. This is in essence a statement of entropy and our inability to control precisely the microscopic behavior of more than a few particles (a few being quite close to one).

Time-reversal replaces t with $-t$, thereby reflecting time about a certain point defined to be $t = 0$. Newton's second law depends on $d^2\mathbf{x}/dt^2$ and remains unchanged. Maxwell's equations,

$$\nabla \cdot \mathbf{E} = \frac{\rho}{\epsilon_0} \qquad \nabla \cdot \mathbf{B} = 0$$

$$\nabla \times \mathbf{E} = -\frac{\partial \mathbf{B}}{\partial t} \qquad \nabla \times \mathbf{B} = \mu_0 \mathbf{J} + \mu_0 \epsilon_0 \frac{\partial \mathbf{E}}{\partial t},$$

are similarly invariant. The magnetic field depends inherently on currents (the situation is more complex in quantum mechanics), which reverse sign under time reversal, so both **B** and **J** become negative. **E** depends on charge distributions which are unaffected by the symmetry, and so it is invariant under time-reversal. This difference between **E** and **B** is interesting to examine a bit further.

Consider the example of a charged particle moving through static, parallel, electric and magnetic fields, **E** and **B** [5, §2.2.3]. Assume that the particle is positively charged and that its motion is initially perpendicular to the applied fields, which lie along the positive z-axis. If the particle has initial velocity V_0 along the y-axis, then its equation of motion is given by the Newton and Lorentz force laws as

$$m\frac{d^2\mathbf{r}}{dt^2} = q\big(E\hat{\mathbf{z}} + V_0\hat{\mathbf{y}} \times B\hat{\mathbf{z}}\big). \tag{1.2}$$

Expanding this into three first-order, partial differential equations, we find

$$\ddot{x}(t) = \frac{qB}{m}\dot{y}, \qquad \ddot{y}(t) = -\frac{qB}{m}\dot{x}, \qquad \text{and} \qquad \ddot{z}(t) = \frac{qE}{m}, \tag{1.3}$$

which are uncoupled and solved to find the full solution

$$\mathbf{r}(t) = \frac{mV_0}{qB}\left(\cos\frac{qB}{m}t\hat{\mathbf{x}} + \sin\frac{qB}{m}t\hat{\mathbf{y}}\right) + \frac{qE}{2m}t^2\hat{\mathbf{z}}. \tag{1.4}$$

The electric field will therefore accelerate the particle vertically and the magnetic field will cause it to revolve, tracing out a left-handed helix as shown in Figure 1.2a, below. We are now in a position to examine more rigorously the behavior of the particle under time-reversal. First we must pick a point an origin t_0 about which to reflect time. In general, upon reversing time about this point $t = t_0$, the equation of motion becomes

$$\bar{\mathbf{r}}(t) = -\frac{mV_0}{qB}\left(\cos\frac{qB}{m}(t_0 - t)\hat{\mathbf{x}} - \sin\frac{qB}{m}(t_0 - t)\hat{\mathbf{y}}\right) + \frac{qE}{2m}(t_0 - t)^2\hat{\mathbf{z}}. \tag{1.5}$$

This motion retraces the steps of the original left-handed helix, just as expected.

If instead we reflect time about the initial point in the xy-plane, $t_0 = 0$, then the particle's trajectory is a *right-handed* helix (Figure 1.2b). At first this may seem odd; however, this is just the time-reversed particle continuing past the initial point (Figure 1.2c). The difference is simply one of initial conditions, and time symmetry is conserved in classical dynamics.

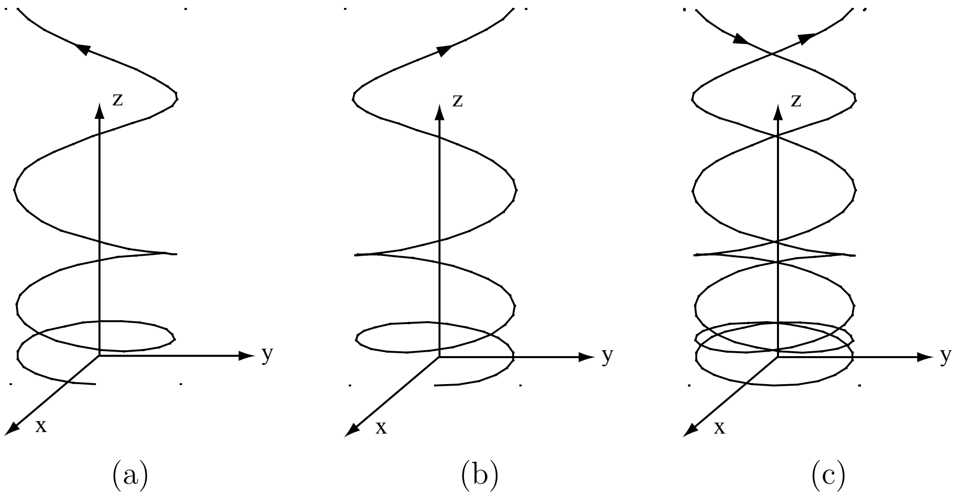

Figure 1.2: Trajectories of charged particles in parallel electric and magnetic fields. (a) A positive particle, forwardin time. (b) Time-reversed from the initial point of motion. (c) Motion in the time-reversed world retraces the steps of (a) and then continues to (b).

1.1.3 Charge

Charge symmetry states that the laws of physics are invariant under the exchange of all particles for their antiparticles, a process known as *charge conjugation*. This is intrinsically a subject of relativistic quantum mechanics and therefore beyond the scope of this thesis, but we can understand it intuitively. For the moment, consider that antimatter particles have the same masses and opposite charges as their corresponding matter particles. Coulomb's law,

$$\mathbf{F} = \frac{1}{4\pi\epsilon_0}\frac{q_1 q_2}{r^2}\hat{\mathbf{r}}, \tag{1.6}$$

is obviously invariant under a global reversal of charge, and Newton's law does not depend on it. Furthermore, electric fields, magnetic fields, and current densities all change signs under charge conjugation and Maxwell's equations are invariant [5, §2.2.1]. Classical dynamics therefore conserves the three discrete symmetries.

1.2 Discrete Symmetries in Quantum Mechanics

Discrete symmetries also find expression in the laws of quantum mechanics, but their descriptions require more mathematics of the reader. First, we will define some essential features of linear and unitary operators. We will then be in a position to discuss parity, time, and charge in more rigorous terms.

1.2.1 Linear and Unitary Operators

Linear operators are mappings between vector spaces that preserve the properties of vector addition and scalar multiplication.[1] Specifically, a linear operator $\hat{L}$ that acts on a vector $|v\rangle$ in a vector space S produces a vector $\hat{L}|v\rangle$ in another space, W. This is written more compactly as $\hat{L} : V \to W$. Linear operators satisfy the defining condition

$$\hat{L}\big(a_1|\alpha_1\rangle + \cdots + a_n|\alpha_n\rangle\big) = a_1\hat{L}|\alpha_1\rangle + \cdots + a_n\hat{L}|\alpha_n\rangle \tag{1.7}$$

for any complex constants a_n and vectors $|\alpha_n\rangle$. *Antilinear* operators switch the constants to their complex conjugates. Both sorts of operators crop up when examining discrete symmetries, so it worth examining them a bit further.

Unitary operators are a type of linear operator that perform one-to-one mappings of vectors in one space onto vectors in another space, such as

$$\hat{U}|\alpha\rangle \to |\alpha'\rangle. \tag{1.8}$$

If the operator is a matrix, then by definition its adjoint equals its inverse:

$$\hat{U}^\dagger = \hat{U}^{-1}, \tag{1.9}$$

$$\hat{U}\hat{U}^\dagger = \hat{U}^\dagger\hat{U} = \hat{I}, \tag{1.10}$$

---

[1] This section combines details from [5, 6, 7, 8].

where $\hat{I}$ is the identity matrix. Unitary operators preserve the value of the inner product,

$$\langle\alpha|\beta\rangle = \langle\alpha|\hat{I}|\beta\rangle = \big(\langle\alpha|\hat{U}^{\dagger}\big)\big(\hat{U}|\beta\rangle\big) = \langle\alpha'|\beta'\rangle, \tag{1.11}$$

and *antiunitary* operators switch it to its complex conjugate. Such operations have no effect on experimental outcome, which is a defining property of discrete symmetry transformations [5, pg. 18]. We shall therefore seek to describe parity, time, and charge through unitary or antiunitary operators.

The action of a symmetry on a specific quantity, such as position or momentum, is described by the symmetry operator acting on the observable operator. This follows because a transformation of state vectors is accompanied by a similar transformation in operators. However, the latter are slightly more complex.[2] Consider a symmetry operator $\hat{O}$ with eigenvectors $|\psi_n\rangle$ that serve as a basis. $\hat{O}$ acts linearly on each component of a vector expressed in this basis, and therefore we may consider only one component without loss of generality. Suppose then that $\hat{O}$ acts on a basis vector $|\psi\rangle$ such that $\hat{O}|\psi\rangle = \lambda|\psi\rangle$. All observable quantities are the same under symmetry transformation, so the transformed operators and vectors must be related in the same manner as the original operators and vectors, such that $\hat{O}'|\psi'\rangle = \lambda|\psi'\rangle$, where $\hat{O}'$ and $|\psi'\rangle$ are the transformed operator and vector, respectively. Replacing $|\psi'\rangle$ with $\hat{U}|\psi\rangle$ as in Eq. 1.8, we find

$$\begin{aligned} \hat{O}'\hat{U}|\psi\rangle &= \lambda\hat{U}|\psi\rangle, \\ \hat{U}^{-1}\hat{O}'\hat{U}|\psi\rangle &= \lambda\hat{U}^{-1}\hat{U}|\psi\rangle. \end{aligned} \tag{1.12}$$

---

[2] This description comes directly from Ballentine, L. E. [8, §3.1], and is reproduced here for convenience with only minor changes.

Subtracting from this the earlier result that $\hat{O}|\psi\rangle = \lambda|\psi\rangle$, Eq. 1.12 becomes

$$(\hat{U}^{-1}\hat{O}'\hat{U} - \hat{O})|\psi\rangle = 0. \tag{1.13}$$

Because $|\psi\rangle$ is an arbitrary basis vector, we may generalize and conclude (after some minor footwork) that

$$\hat{O}' = \hat{U}\hat{O}\hat{U}^{-1}. \tag{1.14}$$

This is the formal result defining a coordinate system transformation for operators, and will be referenced frequently in the coming discussion. With these mathematics behind us, we may consider the discrete symmetries in turn.

1.2.2 Parity

Parity is a unitary operator, which we show by considering the commutator of position and momentum. The momentum operator is defined as $\hat{P} = -i\hbar\nabla$, and position is simply $\hat{X}_i = x_i$ for each of the three coordinates. The commutator is given by

$$[\hat{X}_i, \hat{P}_j] = \hat{X}_i\hat{P}_j - \hat{P}_j\hat{X}_i = i\hbar\delta_{ij} \tag{1.15}$$

where δ_{ij} is the Kronecker delta. The parity operator, $\hat{\mathbf{P}}$ (boldfaced to distinguish it from momentum), switches the signs of position and momentum by definition. These signs cancel and only the right side of Eq. 1.15 will change, so by applying Eq. 1.14 we find the transformed commutator to be

$$[\hat{X}'_i, \hat{P}'_j] = \hat{X}'_i\hat{P}'_j - \hat{P}'_j\hat{X}'_i = \hat{\mathbf{P}}i\hbar\delta_{ij}\hat{\mathbf{P}}^{-1}. \tag{1.16}$$

This agrees with Eq. 1.15 only if $\hat{\mathbf{P}}i\hat{\mathbf{P}}^{-1}$ is equal to i, implying that the parity operator must be unitary, not antiunitary.

If we invert a system's parity *twice* then it remains unchanged. We express this mathematically as

$$\hat{\mathbf{P}}^2 = \hat{\mathbf{P}}\hat{\mathbf{P}} = \hat{I}, \tag{1.17}$$

which reveals that $\hat{\mathbf{P}}$ is hermitean and has eigenvalues of ± 1. (Strictly speaking, actually, one could add a complex phase $e^{i\delta}$ to the eigenvalues and still satisfy the defining condition. This can be done many times in the upcoming mathematics, but the complexities are unnecessary and do not change the results, so it is avoided whenever possible.) States with parity eigenvalue +1 are known as *even*, and those with eigenvalue -1 as *odd*.

1.2.3 Charge

Charge symmetry is also expressed by a unitary operator, as can be seen through another example of Bigi and Sanda [5, §3.2]. Consider the Hamiltonian for a charged particle in a weak electromagnetic field:

$$\hat{H} = -\frac{\hbar}{2m}\nabla - \frac{q}{2m}(\mathbf{A}\cdot\mathbf{P} + \mathbf{P}\cdot\mathbf{A}) + \frac{q^2}{2mc^2}\mathbf{A}^2 + qV. \tag{1.18}$$

Charge conjugation changes the signs of only q, $\mathbf{A}$, and V, leaving the Hamiltonian invariant. Therefore, the charge operator $\hat{\mathbf{C}}$ acting on $\hat{H}$,

$$\hat{\mathbf{C}}\hat{H}\hat{\mathbf{C}}^{-1} = \hat{H}, \tag{1.19}$$

leaves it unchanged, and $\hat{\mathbf{C}}$ must also be a unitary operator.

1.2.4 Time

Time symmetry is expressed by an antiunitary operator, which again follows from the position-momentum commutator. Time reversal inverts momentum but does not change position, so the transformed commutator is

$$\hat{\mathbf{T}}[\hat{X}_i, \hat{P}_j]\hat{\mathbf{T}}^{-1} = -[\hat{X}_i, \hat{P}_j] = \hat{\mathbf{T}}i\hbar\delta_{ij}\hat{\mathbf{T}}^{-1} = -i\hbar\delta_{ij}. \tag{1.20}$$

This will only be true if $\hat{\mathbf{T}}i\hat{\mathbf{T}}^{-1}$ is equal to $-i$, and therefore $\hat{\mathbf{T}}$ must be *antiunitary*. This immediately distinguishes it from the other discrete symmetry operators.[3]

The mathematics of discrete symmetry operators will prove essential to our discussion of electric dipole moments in fundamental particles, but first we shall consider some interesting situations under which symmetries are broken.

1.3 Symmetry Violations

With formal expressions for the discrete symmetry operators in quantum mechanics behind us, we now turn our attention to conservation and violation, both theoretical and observed. To begin, we shall address the notion of "symmetry violation" with a bit of history.

Parity, time, and charge were taken to be rigorously upheld symmetries until 1956, when Lee and Yang proposed an experiment to test parity in the weak interaction [9]. The next year, C. S. Wu observed the radioactive decay of magnetically aligned ^{60}Co and the results were definitively asymmetric [10]. More electrons were emitted *opposite* to the direction nuclear spin, which is anisotropic and therefore a parity-violating observation, as Figure 1.3 shows.

Discrete symmetries can therefore be violated, and the observed violations vary significantly by degree [4, §4.8]. Lee and Yang argued additionally that an experiment to measure parity nonconservation in β decay could also distinguish a violation of charge symmetry [11]. They made this prediction noting that no rigorous tests

---

[3] An interesting consequence of the antiunitary nature of $\hat{\mathbf{T}}$ is **Kramer's Degeneracy Theorem**. The proof and some of its consequences are outlined briefly in [5, §3.4].

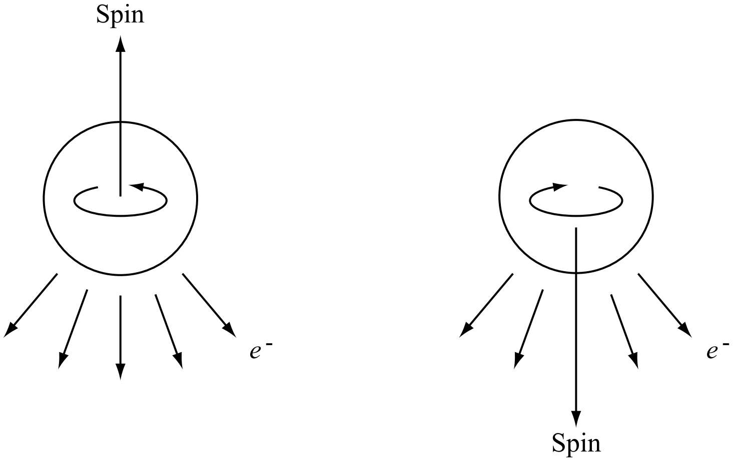

(a) (b)

Figure 1.3: Parity violation in β decay of ^{60}Co nuclei. (a) Electrons are emitted preferentially opposite to the nuclear spin axis. (b) Parity switches the spin axis relative to the preferred direction of electron emission.

of charge invariance in the weak interaction had been performed, and before the publication of observed parity nonconservation.

These violations of both parity and charge are two of several discrete symmetry violations that have now been observed. For a comprehensive overview, see [5] and [12]. There are strong experimental and theoretical reasons to believe that the combined operation **CPT**, taken in any order, is the fundamental symmetry transformation in a relativistic quantum field theory. Such a theory allows each discrete symmetry to transform a system partially, provided that the product **CPT** returns it to its original state. This naturally allows for parity and charge violation in ^{60}Co β decay, and also for the predicted parity and time violations of intrinsic EDMs, which we now proceed to discuss.

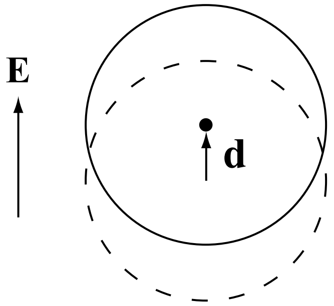

Figure 1.4: An electric field induces a parallel EDM in an atom.

1.4 Electric Dipole Moments

1.4.1 Classical, Quantum, and Intrinsic

In classical electrodynamics, an electric dipole moment (EDM) is a spatial vector pointing generally from regions of negative charge to those of positive charge. It is given the formal definition

$$\mathbf{d} = \int \mathbf{r}'\rho(\mathbf{r}')d\tau', \tag{1.21}$$

where $\mathbf{r}'$ points from the origin to a piece of charge whose density is ρ, and the integral is taken over the region of interest [13, §3.4.2]. In the context of our study of symmetry, an interesting example of an EDM is that induced in an atom exposed to a weak electric field.

Consider an atom with a spherically symmetric electron distribution and a point-like nucleus exposed to an electric field $\mathbf{E}$ [13, §4.1.2]. Neglecting shape distortions, the electron cloud shifts oppositely to the direction of $\mathbf{E}$ and the nucleus parallel to it, as in Figure 1.4. This internal asymmetry creates a field of opposite strength to that of the applied field, and thereby a dipole $\mathbf{d} = \alpha\mathbf{E}$, where α is a constant of proportionality, the value of which varies by element. The energy U of an electric dipole in a field is equal to $-\mathbf{d}\cdot\mathbf{E}$, and therefore in this case $U = -\alpha E^2$.

Parity switches the direction of both the electric field and the induced EDM, so the mirror image is still physically sensible. Charge symmetry also switches **E** and **d**, and time reversal changes nothing. This classical dipole moment therefore conserves the discrete symmetries.

In quantum mechanics, an electric dipole moment is the expectation value of the operator

$$\hat{d} = \sum_i \mathbf{r}_i q_i, \tag{1.22}$$

where the integral of Eq. 1.21 has been replaced with a sum over i discrete particles. Its energy is described by a term in the Hamiltonian of the form $\hat{H}_{dip} = -\mathbf{d}\cdot\mathbf{E}$, which, for induced and atomic EDMs, is invariant under reversal of the discrete symmetries. But what of those dipole moments whose magnitude and direction are independent of any applied field? These are called *intrinsic* EDMs and are the subject of interest in this thesis. We now consider some properties of these dipole moments in an effort to motivate our research.

1.4.2 Symmetry Violations in Intrinsic EDMs

Any fermionic EDM must point either parallel or antiparallel to the spin axis to prevent added degeneracy. The Pauli exclusion guarantees this by stating that no two fermions in a system may have the same quantum numbers. Were the dipole moment oriented in any other direction then it would grant an extra degree of freedom and require another quantum number to describe the state. No experimental evidence supports this. We therefore express the electric dipole moment as a vector proportional to the spin: $\mathbf{d} = d\hat{\sigma}$.

Were such a dipole moment to exist, it would constitute a direct violation of both parity and time symmetries. Classically the argument is quite direct, as Figure 1.5 shows. Consider an electron whose dipole moment is (arbitrarily) parallel to its spin axis. Parity ultimately reverses the direction of the dipole moment, but not that of the spin; time reversal does the opposite. Both situations result in the dipole moment *antiparallel* to the spin axis, representing a fundamentally different particle. If an intrinsic EDM were measured in a charged particle, it would therefore constitute a violation of both parity and time.

These arguments are made quantum mechanical by considering the operators $\hat{\mathbf{P}}$, $\hat{\mathbf{T}}$, and $\hat{\mathbf{C}}$ [5, ch. 3]. The **parity** operator acts on a state $|\psi\rangle$ and maps it onto $|\psi'\rangle$, such that $\hat{\mathbf{P}}|\psi\rangle \rightarrow |\psi'\rangle$. It switches the sign of $\mathbf{r}$ in Eq. 1.22, and therefore also the sign of $\hat{d}$, which we express formally as $\hat{\mathbf{P}}\hat{d}\hat{\mathbf{P}}^{-1} = -\hat{d}$. The expectation value of the electric dipole moment is then given by

$$\langle\psi|\hat{d}|\psi\rangle = \langle\psi|\hat{\mathbf{P}}^{-1}\hat{\mathbf{P}}\hat{d}\hat{\mathbf{P}}^{-1}\hat{\mathbf{P}}|\psi\rangle = \big(\langle\psi|\hat{\mathbf{P}}^{\dagger}\big)\big(\hat{\mathbf{P}}\hat{d}\hat{\mathbf{P}}^{-1}\big)\big(\hat{\mathbf{P}}|\psi\rangle\big) = -\langle\psi'|\hat{d}|\psi'\rangle. \tag{1.23}$$

In a parity symmetric theory, the first and last terms must be equal, but in this case they are opposites. The presence of an intrinsic EDM therefore constitutes a violation of parity symmetry.

Time symmetry is also violated, as we demonstrate by similar arguments. If the system is to be non-degenerate, then the expectation value of $\hat{d}$ must be proportional to that of the angular momentum operator, $\hat{J}$, because this is the only three-dimensional vector that describes the state of the system. The dipole moment is invariant under time reversal, so we find

$$\langle\psi|\hat{d}|\psi\rangle = \big(\langle\psi|\hat{\mathbf{T}}^{-1}\big)\hat{\mathbf{T}}\hat{d}\hat{\mathbf{T}}^{-1}\big(\hat{\mathbf{T}}|\psi\rangle\big) = \langle\psi'|\hat{d}|\psi'\rangle, \tag{1.24}$$

Substituting for $\hat{d} = k\hat{J}$ in the first and last terms, and noting that $\hat{J} \rightarrow -\hat{J}$ under time reversal, we find

$$k\langle\psi|\hat{J}|\psi\rangle = -k\langle\psi'|\hat{J}|\psi'\rangle, \tag{1.25}$$

which can only be true if $k = 0$. In a time-reversal symmetric theory, the dipole

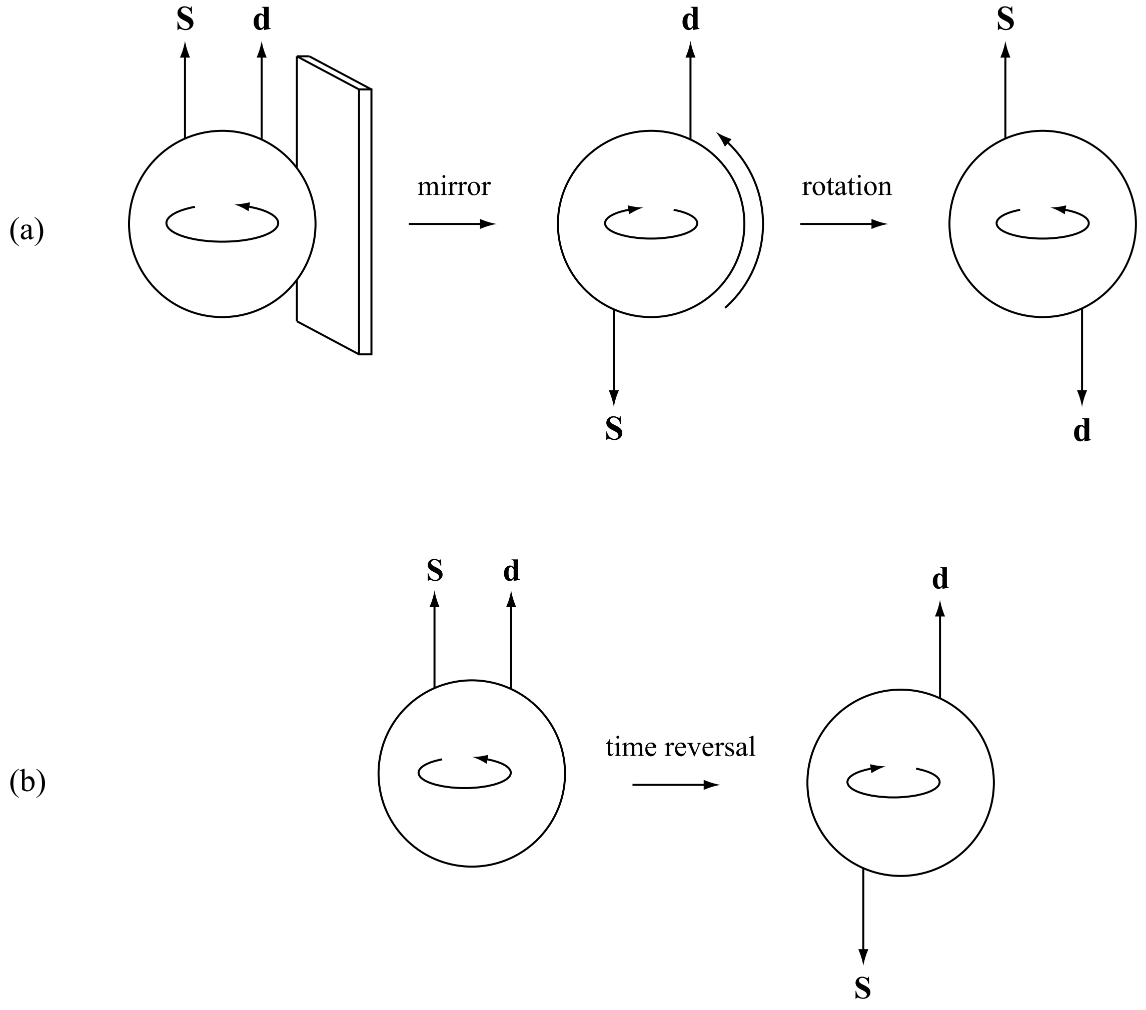

Figure 1.5: Parity and time reversal result in fundamentally different electrons than the original. (a) Parity, (b) Time.

moment must therefore be zero. If a non-zero, intrinsic EDM were measured, this would constitute a violation of both parity and time symmetries – a worthwhile field of study, indeed!

The field of intrinsic electric dipole moments has quite a history, beginning with studies of the neutron. In 1947, Havens, Rabi, and Rainwater examined the interactions of neutrons with electrons in lead [14], and their data provide a limit on the magnitude of the neutron EDM of $|d_n| < 3 \times 10^{-18}$ e cm [15]. Smith, Purcell, and Ramsey specifically intended to measure the neutron EDM and in 1957 they refined the limit to $|d_n| < 5 \times 10^{-20}$ e cm [16]. The present limit on the neutron EDM is $|d_n| < 6.3 \times 10^{-26}$ e cm, as measured by Harris *et al.* [17].

The current limit on the electron electric dipole moment is $|d_e| < 1.6 \times 10^{-27}$ e cm, as obtained by Regan *et al.* at the University of California at Berkeley [18]. Our present experiment has yielded a limit of $|d_e| < 1.5 \times 10^{-24}$ e cm as of the summer of 2006. The last published limit was $|d_e| < 5 \times 10^{-24}$ e cm [1], which is above the present limit but better than the only previous limit obtained by a solid state experiment, $|d_e| < 2 \times 10^{-22}$ e cm [19, 20].

Electric dipole moment searches have not only continued until the present but have accelerated and spread. The reason for this profound increase in the popularity of the field is that EDMs provide excellent tests of theories beyond the Standard Model. Many theories predict (however loosely) values for intrinsic EDMs that are naggingly close to the current experimental limits. This is powerfully motivating.

Chapter 2

Experimental Theory

The current Amherst experiment to measure the electron electric dipole moment uses a large, polycrystalline sample of gadolinium iron garnet. This distinguishes it immediately from nearly all other EDM searches; we are, indeed, only the second group ever to perform a solid-state EDM measurement.

The use of a solid sample has many advantages and disadvantages that merit discussion, and this chapter addresses these issues. We begin by considering the general principles of EDM measurements, and particularly those of our solid state system. The properties of gadolinium iron garnet are then described along with the design of the sample. Methods of signal detection and analysis are discussed to close.

2.1 Solid State Experiments

Fundamental particles with electric dipole moments will align in electric fields. This alignment is the signature of a non-zero EDM and therefore the focus of related experiments. Unfortunately, it comes with a bit of a snag: most fundamental particles carry charge and therefore cannot be held in stable equilibrium by electrostatic forces. It is therefore no wonder that EDM searches began with neutrons.

Atomic systems provide an attractive solution to this because they are electrically neutral and contain lots of particles (whether electrons, protons, or neutrons) held rigidly in bound states. However, in 1963 Schiff published a theorem stating that the first-order energy shift due to electric dipole moments should be completely shielded in atoms [21].[1] His proof concerns only non-relativistic particles interacting electrostatically, which led Sandars to complete a fully relativistic calculation in 1965 [22]. His results are staggering: not only does relativity allow EDMs to perturb atomic systems, but their effects are *enhanced*. The magnitude of enhancement depends intricately upon the structure of the atom, but generally scales as the atomic number cubed and can reach several orders of magnitude.

Heavy atoms therefore present ideal systems for studying the electric dipole moments of fundamental particles. To this end, our experiment uses a large, polycrystalline sample of gadolinium iron garnet (GdIG), which provides an enormous number of heavy atoms. The magnetic properties of GdIG will be discussed in the next section, but first we shall consider the principles, advantages, and limitations of solid state EDM experiments in general.

The basic principle of such experiments is that magnetic moments align in applied magnetic fields. A magnetic material has many such moments, both macroscopically in domains and microscopically in the particles that they comprise, and so it will magnetize in an applied field. This magnetization corresponds to the average alignment of the moments parallel or antiparallel to the field. In fundamental particles, the magnetic dipole moment is parallel to the spin, which, by previous arguments in §1.4.2, is also parallel to the electric dipole moment. A magnetically polarized solid will therefore be electrically polarized if its constituent particles have electric dipole moments.

The argument works equally well in reverse: electric dipole moments align in

---

[1] A derivation of his theorem is included in appendix A, but the mathematics are lengthy and would prove distracting at this point.

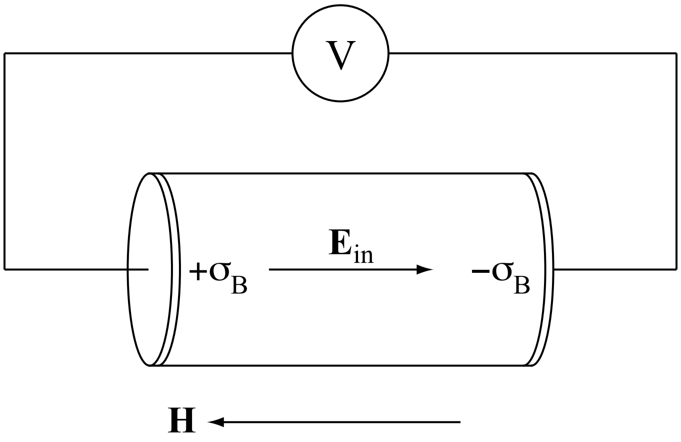

Figure 2.1: A basic design for a solid state EDM experiment. The magnetic field aligns the EDMs, electrically polarizing the sample.

applied electric fields, thereby aligning the magnetic moments. Our experiment is of the former type, in which we apply a magnetic field to our GdIG sample and measure its electrical polarization. It can be shown that an electrical polarization induces bound surface and volume charges, σ_b and ρ_b, given by

$$\sigma_b = \mathbf{P} \cdot \hat{\mathbf{n}}, \tag{2.1}$$

$$\rho_b = -\nabla \cdot \mathbf{P}, \tag{2.2}$$

where **P** is the polarization vector, defined as electric dipole moment per unit volume [13, §4.1–2]. This surface charge creates a potential difference across the sample, which we measure by capacitively coupling it to a detector. Figure 2.1 shows one such apparatus, where the polarized material is cylindrical and has its axis parallel to the applied field.

This is the essence of our experiment. Geometrical and circuitry changes aside, we magnetize a sample of gadolinium iron garnet and measure the potential across it. We must consider details such as input impedances, capacitance, noise, shielding, and other systematic effects, but the premise is identical. An improved design requires placing the system in a Faraday cage and accounting for finite input impedance, finite sample capacitance, and non-zero detector capacitance.

Our apparatus is more intricate than the one pictured in Figure 2.1, and the various differences will be explained throughout the coming sections. To give them some preparative structure, a brief overview follows. First, we use two-channel detection rather than a differential amplifier; the channels are labeled A and B. This allows us to see the behavior of each electrode individually, which is of great advantage in locating systematic effects. The data are eventually subtracted to obtain a potential difference corresponding to the electron EDM, but the ability to analyze each channel separately is important.

Second, our GdIG sample is toroidal rather than cylindrical. This decreases demagnetizing fields by closing field lines inside the magnetic material, rather than in free space. Third, the detector circuit is divided into two stages, the first of which has extremely high input impedance (approximately 10^{13} Ω). This isolates the signal and amplifies it approximately seventy-fold before sending it to a filter.[2]

Finally, our applied magnetic field is not constant, but rather alternates with pulses that flip the magnetization of the sample. This makes the EDM potential an antisymmetric which helps to distinguish it from other effects. In fact, the entire apparatus and measurement scheme are built on principles of symmetry such as this. Many things are reversed so that effects without the antisymmetric, EDM characteristic are naturally subtracted.

It is useful now to consider the magnetic properties of gadolinium iron garnet. These play a crucial role in our experimental design, and the reasons for our modifications and changes to the apparatus will be unclear without an understanding of the physics involved.

---

[2] See appendix B for explanations of complex impedance, filter analysis, and the five-pole Bessel filter used in our detector.

2.2 Gadolinium Iron Garnet

Sandars's work demonstrates that atoms enhance the effects of their constituent electric dipole moments by factors that scale roughly as the atomic number cubed. Heavy atoms therefore present ideal systems for the study of EDMs: the 1989 Amherst experiment used cesium vapor cells [23], and the current limit was set with atomic beams of thallium [18].

Our experiment uses a polycrystalline sample of gadolinium iron garnet (GdIG), which has numerous favorable qualities that merit explanation. Sensitivity to the electron electric dipole moment comes from the gadolinium, which has an atomic number of 64. The material is also highly resistive, which is necessary given the nature of our signal detection. However, it is the magnetic behavior that provides the primary motivation for our experimental methods, so we will discuss this first.

2.2.1 Magnetic Properties

The chemical formula of gadolinium iron garnet is

$$\mathrm{Gd_3}^{3+}\mathrm{Fe_2}^{3+}\mathrm{Fe_3}^{3+}\mathrm{O_{12}}^{2-}.$$

The gadolinium can be replaced by other rare-earth ions, such as yttrium or gallium, to change the thermal and magnetic properties of the material. All have the same crystal structure, which is pictured in Figure 2.2. There are three magnetic sub-lattices, which contain ions that align parallel to each other. The iron ions in lattices (a) and (d) align antiparallel to each other; lattice (c) contains the gadolinium ions, which align parallel to (a). These magnetizations always have the same relative orientations, but their magnitudes are temperature dependent, as shown in Figure 2.3. Specifically, the magnitude of gadolinium magnetization decreases rapidly with increasing temperature; compared to this, the iron changes little. The overall magnetization is the sum of those of the three sub-lattices, and because Gd varies so greatly there is an intermediate point at which the total magnetization drops to zero. This is known as the *compensation temperature.*

It is important to note that while the overall magnetization of GdIG drops to zero at the compensation temperature, this is simply because the magnetizations of the atoms add to zero; they are not individually zero. Because the direction of overall magnetization follows that of the applied field, the gadolinium and iron atoms of lattice (c) will align parallel to the field below the compensation temperature, and against it above the compensation temperature. The directions flip, but the magnitudes change smoothly; there is therefore significant microscopic order throughout [25]. These ideas are important to discussions in the next section, which explains the geometry of our sample.

As a first approach to understanding the magnetic behavior of GdIG, let us consider the general response of materials to applied magnetic fields. The magnetization $\mathbf{M}$ of a material is defined as the magnetic dipole moment per unit volume, given by

$$\mathbf{M} = \frac{1}{\mu_0}\mathbf{B} - \mathbf{H}, \tag{2.3}$$

where $\mathbf{H}$ is the applied field and $\mathbf{B}$ is the total flux density.[3] There is in general some relationship between $\mathbf{H}$ and $\mathbf{M}$, and this allows us to distinguish at least three different types of materials: *paramagnetic*, *ferromagnetic*, and *ferrimagnetic*.[4]

Paramagnetic materials magnetically align in an applied field, but do not retain their magnetizations after the field dissipates. They contribute positively to the field, and their magnetizations vary approximately proportionally to the applied field, and

---

[3] This amounts to the same thing as a field, but with a headache from unit conversions. $\mathbf{H}$ is what we apply in a controlled fashion, and $\mathbf{B}$ is the total field, which may include material contributions. They are related by Eq. 2.3, where $\mu_0 = 4\pi \times 10^{-7}$ A/m^2 is the permeability of free space.

[4] The following discussion of magnetic materials combines details from [26, 27, 28]. The last deals most directly with rare-earth garnets.

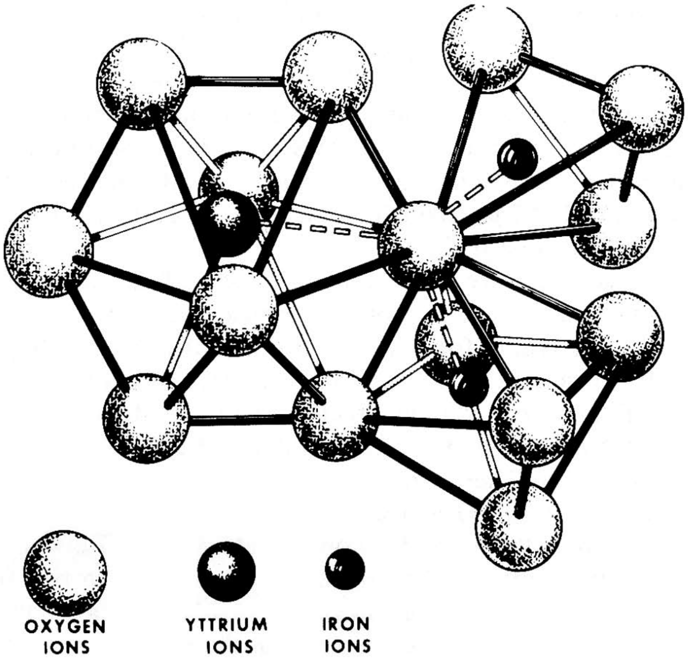

Figure 2.2: Partial crystal structure of an iron garnet, showing the immediate environment of the rare-earth ion. (After [24, Figure 5.8b].)

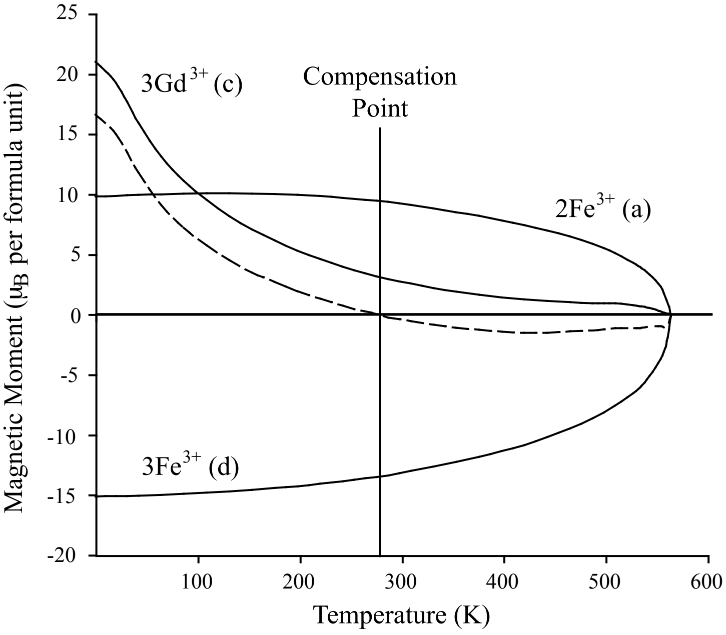

Figure 2.3: Magnetization of the GdIG sub-lattices with temperature. Total magnetization is the dashed curve, and its sign indicates the direction relative to gadolinium. (After [24, Figure 5.9].)

inversely with the temperature. This relationship,

$$M \propto \frac{H}{T}, \tag{2.4}$$

is known as **Curie's law**. Magnetization decreases with increasing temperature because thermal energy prevents complete alignment with the applied field. The relationship is only approximate in the low temperature region, because M obviously does not diverge as T approaches 0 K.

Ferromagnetic materials have many domains, each with a spontaneous moment in the absence of any applied field. This implies that the individual, paramagnetic constituents align in parallel, and that their exchange interactions are strong enough to maintain the alignment and preserve the field. However, increasing thermal energy decreases the alignment of the domains, and there is a temperature at which ferromagnets lose their spontaneous moments. This is known as the **Curie point**, T_C, above which ferromagnets behave paramagnetically [13, §6.4.2]. From Figure 2.3 we see that the Curie temperature for GdIG is roughly 560 K.

Ferrimagnetic materials are ferromagnets whose total magnetization at $T = 0$ K does not correspond to complete parallel alignment of all constituent moments (spins). This implies that some magnetic moments must align antiparallel to others, decreasing $\mathbf{M}$. GdIG is ferrimagnetic because the iron ions in lattices (a) and (d) are ferromagnetic, but orient oppositely. To demonstrate this, we again refer back to Figure 2.3 and examine the magnetic moments of the ions at $T = 0$ K. Gd has seven unpaired $4f$ and one unpaired $5d$ electron, giving it the highest spin of any element in the Lanthanide series. Its electron structure is

$$\text{Gd: } 1s^2\ 2s^2\ 2p^6\ 3s^2\ 3p^6\ 3d^{10}\ 4s^2\ 4p^6\ 4d^{10}\ 4f^7\ 5s^2\ 5p^6\ (5d^1)\ (6s^2),$$

where the bracketed $4d$ and $6s$ shells are completely removed in the trivalent ion. Gd^{3+} therefore has total spin $\frac{7}{2}$, and contributes 7 μ_B to the overall GdIG moment.

The electron structure of iron is

$$\text{Fe: } 1s^2\ 2s^2\ 2p^6\ 3s^2\ 3p^6\ (3d^6)\ (4s^2),$$

where the trivalent ion lacks its entire $4s$ shell, and one electron from the $3d$ shell. Fe^{3+} therefore has spin $\frac{5}{2}$ and contributes 5 μ_B to the overall moment. Were GdIG a uniformly aligned ferromagnet, the total spin would be the sum of the moments of each atom, giving $S = 46\ \mu_B$ per formula unit. However, the extrapolated moment at $T = 0$ K is only 16 μ_B, which is the predicted value if three of the five iron ions are oriented oppositely to the Gd^{3+}. Gadolinium iron garnet is therefore best described as a ferrimagnetic.

Gadolinium ions in GdIG experience fields primarily due to the aligned iron ions [25]. Within a magnetized sample at 100 K, the interaction between iron and gadolinium ions is around seven times stronger than the interactions between gadolinium ions; the iron-iron interactions are another order of magnitude stronger. Because iron is ferromagnetic it maintains its magnetization after an applied field has dissipated, and its field is strong enough to keep the gadolinium aligned roughly as $1/T$ (Figure 2.3). The domains of GdIG therefore act as ferrimagnets, whereas the gadolinium atoms would act as paramagnets in isolation. This is useful because our sample remains magnetized without our having to maintain an applied field, as will be discussed further in §2.4.

2.2.2 EDM Enhancement

The *enhancement factor* of an atom is the amount by which the effects of its constituent EDMs are scaled due to the particulars of the atomic structure. As a first approach, consider that the enhancement factor of the electron EDM, k, scales approximately as $\alpha^2 Z^3$, where $\alpha \approx 1/137$ is the fine structure constant and Z is the atomic number [29]. For gadolinium this gives $k \approx 14$ but for iron only $k \approx 1$ (oxygen is negligible); gadolinium has the largest effect by far, so EDMs in the other atoms are neglected. However, in GdIG the gadolinium atoms are located within a lattice of oxygen atoms small enough that their wave functions overlap. A more precise calculation is therefore required to determine the exact enhancement factor of Gd in the garnet structure.

T. N. Mukhamedjanov *et al.* performed this calculation in 2003 [30]. Their approach was to calculate the perturbation that the presence of electron electric dipoles would have on the lattice energy of GdIG; these perturbations are then later related to physically observable quantities. We will discuss their work by emphasizing the logic used and the approximations made, but without delving into the mathematics. The elastic properties of GdIG are discussed first, to prepare for a direct consideration of the quantum mechanical description of gadolinium ions in GdIG. By introducing electron EDMs we state, but do not derive, a result relating the lattice distortion energy to the magnitude of the electron EDM. Finally, this is related to a macroscopic polarization.

For small disturbances, GdIG should behave in an approximately spring-like manner, giving it a potential response of the form

$$U(x) = \frac{1}{2}kx^2, \tag{2.5}$$

where k is a constant and x is the magnitude of some displacement that occurs in the position of the Gd^{3+}. The energy minimum in this case clearly occurs at $x = 0$. However, if the system is perturbed by some energy $\Delta U(x)$, then the potential becomes

$$U(x) = \frac{1}{2}kx^2 + \Delta U(x) \tag{2.6}$$

and the minimum must be recalculated. EDMs have this effect in GdIG, as we now proceed to show.

First, the potential in which the gadolinium electrons reside must be calculated. Gd^{3+} is a trivalent ion whose potential can be described by an *effective potential* with parameters chosen to match observed energy levels. The potential is given by

$$V_{\mathrm{Gd}}(\mathbf{r}) = \frac{1}{r}\frac{(Z_i - Z)(e^{-\mu/d} + 1)}{(1+\eta r)^2(e^{(r-\mu)/d} + 1)} - \frac{Z_i}{r}, \tag{2.7}$$

where μ, d, and η are fit values, and Z_i is the charge of ionic gadolinium core ($Z_i = 4$ for Gd^{3+}, as reported). Solving the Dirac equation with the above potential, the authors find energy levels for single-electron states that differ by approximately 2% from the observed values in isolated Gd^{3+} ions. Eq. 2.7 is therefore considered to be a good model of free, trivalent gadolinium ions.

As Figures 2.2 and 2.4 show, the oxygen atoms surround gadolinium in a dodecahedral shape resembling a twisted cube. To make the calculations manageable, the authors approximate the effects of these oxygens as a spherically symmetric, attractive potential around the gadolinium. This potential is of the form

$$V_{\mathrm{O}}(\mathbf{r}) = -A_0 e^{-\left(\frac{r-r_0}{D}\right)^2}, \tag{2.8}$$

where r_0 is the distance of separation between Gd and O, and A_0 and D are fit parameters. The total potential in which the gadolinium electrons are located is the sum of Eqs. 2.7 and 2.8, and the fit parameters of the latter are chosen such that the total potential approximates observed energy levels of gadolinium in GdIG.

Further calculation shows that the shift in lattice energy due to electron EDMs,

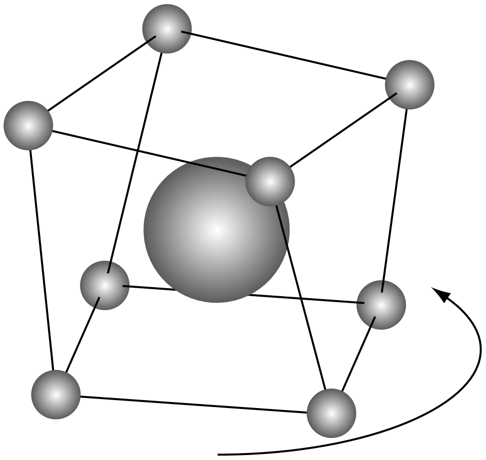

Figure 2.4: Oxygen atoms form a dodecahedral structure around gadolinium, analogous to a twisted cube. (After [30, Figure 1].)

when gadolinium is displaced by a distance x, is given by

$$\Delta U(x) = -A\frac{x}{a_B}\left(\frac{d_e}{ea_B}\right)E_0(\hat{\mathbf{n}}_{\mathrm{S}} \cdot \hat{\mathbf{x}}), \tag{2.9}$$

where A is a calculated parameter, e is the fundamental unit of charge, a_B is the Bohr radius, $\hat{\mathbf{n}}_{\mathrm{S}}$ is a unit vector in the direction of the Gd spin, and $\hat{\mathbf{x}}$ is a unit vector along the direction of displacement. A is calculated to be approximately 0.095, as a lower bound. The energy shift due to a displacement of Gd by a distance x is therefore given by Eqs. 2.6 and 2.9 as

$$U(x) = \frac{1}{2}kx^2 - A\frac{x}{a_B}\left(\frac{d_e}{ea_B}\right)E_0. \tag{2.10}$$

U will naturally be minimized, but to calculate the value of x that does this we must know more about the effective spring constant k. Mukhamedjanov *et al.* choose a value of

$$k = 0.095\frac{E_0}{{a_B}^2} \tag{2.11}$$

based on infrared spectroscopy data of GdIG and YIG. By coincidence, the dimensionless factor above is equal to the lower bound of A in Eq. 2.9, and so the value of x that minimizes U is

$$x \approx \frac{d_e}{e}, \tag{2.12}$$

which is a remarkably simple relationship. This is the fundamental result of Mukhamedjanov *et al.*'s calculation, and may be manipulated directly to yield an observable polarization.

The electrical polarization $\mathbf{P}$ is defined as the dipole moment per unit volume. For a point particle the dipole moment is $\mathbf{d} = q\mathbf{r}$, where q is the particle's charge and $\mathbf{r}$ is its position relative to some origin. In our case, trivalent gadolinium ions are displaced by a distance $x \approx d_e/e$, so we have $q = 3e$ and $r = x$. The macroscopic polarization is therefore given by

$$\boxed{\mathbf{P} = 3n_{\mathrm{Gd}} d_e \hat{\sigma},} \tag{2.13}$$

where $n_{\mathrm{Gd}} = 1.235 \times 10^{22}$ atoms/cm^3 is the number of gadolinium ions per unit volume in GdIG, and $\hat{\sigma}$ is a unit vector along the direction of Gd spin.[5]

This result incorporates the complete response of GdIG to the alignment of electron EDMs. We emphasize this because GdIG is a dielectric material, and one might be led incorrectly to assume that the polarization in Eq. 2.13 induces a dielectric response. On the contrary, such behavior has already been explicitly included in the calculation of x, which involved modeling the lattice elasticity. Earlier work by the same group used the dielectric constant in these approximations [31], but this has been exchanged for spectroscopic data.

---

[5] Interestingly, this is exactly what we would have gotten by assuming that each unpaired electron in Gd^{3+} contributes d_e to the overall dipole moment.

2.2.3 A Rough Prediction

To get a sense of the magnitudes of the involved numbers, Mukhamedjanov *et al.* consider the example of a 10 cm long sample of pure GdIG magnetized at $T = 0$ K. Eq. 2.13 gives the polarization in unspecified units, but we revert to SI for consistency. The internal electrical field in a uniformly polarized cylinder is given by

$$\mathbf{E}_{\text{in}} = -\frac{1}{\epsilon_0}\mathbf{P}_{\text{in}}, \tag{2.14}$$

where $\epsilon_0 \approx 8.85 \times 10^{-12}$ C^2/Nm^2 is the permittivity of free space [13, 30]. If the polarization is approximately constant within the cylinder, the potential difference between its ends will be simply $\Delta V = El$, where $l = 10$ cm is the length of the cylinder. If we take the size of d_e to be the upper bound of the current world limit, $|d_e| < 1.6 \times 10^{-27}$ e cm, the potential is

$$\Delta V = \int \mathbf{E}\cdot\mathbf{dl} = -\frac{1}{\epsilon_0}P_{\text{edm}}l = -\frac{1}{\epsilon_0}3d_e n_{\text{Gd}}l \approx -1.1 \text{ nV}, \tag{2.15}$$

which agrees with the reported result.

Roughly speaking, our experiment is ten times *less* sensitive to the EDM, the details of which will be discussed toward the end of this chapter. To reach the world limit we would have to measure a potential difference on the order of 0.1 nV, which is arrestingly small. Our present measurements are accurate to the level around 0.1 μV, and so our limit is approximately 10^{-24} e cm.

In the final sections of this chapter, we will return to this result and relate our measured potential asymmetry to a value of the electron EDM more specifically. For now, we must modify this picture a bit further by considering the geometry of our sample. The logic behind the present construction depends heavily on the temperature dependence of the various sub-lattices's magnetizations. We will consequently refer back to Figure 2.3 frequently to justify certain decisions and claims.

2.3 Sample Structure

This section describes the geometry and composition of our polycrystalline GdIG sample, focusing on two new concepts. The first is toroidal geometry, which changes our approach to the EDM search considerably. The second is sample doping, in which the concentration of gadolinium is decreased and some yttrium added in its place.

2.3.1 Toroidal Geometry

The cylindrical model presented in Figure 2.1 has the disadvantage of strong demagnetizing fields. In one sense this means that the field it produces must be maintained in free space to close field lines, which is energetically disfavored. Microscopically, when a sample is magnetized its poles align parallel to the applied field and enhance it. However, finite samples have ends where opposite poles will effectively “build up.” A field opposing the magnetization will therefore form and tend to cancel it, as in Figure 2.5a [32]. This is called the *demagnetizing field* and is typically given the symbol $\mathbf{H}_\mathrm{D}$.

A toroidal geometry avoids these difficulties by closing field lines within the material, as in Figure 2.5b. Poles do not build up at endpoints because there simply aren’t any. However, this is immediately the source of another problem: endpoints are necessary for a potential difference! In a pure toroid magnetized circularly about it axis, there will be no point at which surface charge can build up unopposed. To counter this difficulty we introduce the topic of sample doping.

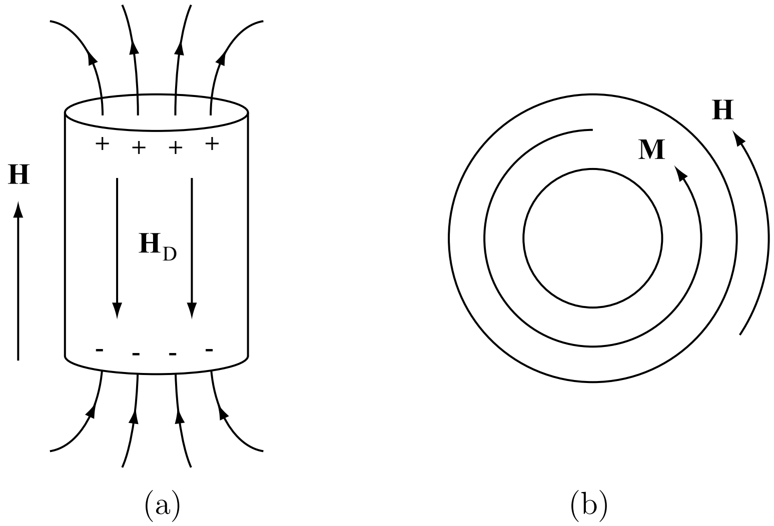

Figure 2.5: Demagnetizing fields. (a) Poles build up on the ends of a sample, creating a demagnetizing field. (b) Field lines close within a toroidal sample.

2.3.2 Gadolinium-Yttrium Doping

Mixed rare-earth garnets are commonly made, and involve two or more trivalent ions mixed together in a single sample. The chemical formula for such a mixture of compounds A and B is

$$A_xB_{3\text{-}x}Fe_5O_{12},$$

where $0 \leq x \leq 3$ indicates the average number of A per formula unit. Our sample includes a mixture of gadolinium and yttrium, which is commercially available and is in fact less expensive than pure GdIG. Yttrium is nonmagnetic, so any sample of GdIG doped with yttrium will have less net magnetization from gadolinium. (In Figure 2.3 this translates into vertically scaling down the Gd^{3+} curve.) As the gadolinium concentration is decreased, the compensation temperature decreases. Eventually there is not enough gadolinium to counter the iron (d) lattice and there is no actual point of net zero magnetization. The limits for this construction are $0.73 \leq x_{Gd} \leq 3$ [25].

To take advantage of toroidal geometry while still maintaining a potential difference between two points, we use a vertically separated, split-toroid of two differently doped halves. Each has a different compensation temperature, and so between the two there is a temperature at which the gadolinium magnetizations are oppositely directed. The overall magnetization of the sample is continuous, but in one half the Gd moments point parallel to the applied field and in the other half antiparallel. We therefore identify three temperature regions of interest:

1. **Below both compensation temperatures**: Gadolinium magnetization dominates in both halves, and the Gd moments are parallel to the applied field.
2. **Between compensation temperatures**: One half has Gd moments parallel to the applied field, the other half against. They oppose at the interface.
3. **Above both compensation temperatures**: Iron (d) dominates in both halves. Gd moments are parallel to each other and antiparallel to the field.

These temperature regions are important because our sensitivity to the electron EDM comes from gadolinium. Yttrium is nonmagnetic, so it does not align in applied fields and creates no observable signal. The direction of the gadolinium magnetization is therefore the direction of electrical polarization.

Each region is interesting because the EDM signal should appear differently at each temperature. (We will return to an exact calculation of these differences in §2.5.2.) By varying the sample temperature between the three regions we can isolate temperature-dependent effects and non-EDM signals, and subtract them to improve our resolution. We consequently have chosen to use a sample with one half of 1.8 Gd^{3+} ions per formula unit, and another with 1.35. This places their compensation temperatures at approximately 153 K and 104 K, respectively, as shown in Figure 2.6.[6]

These compensation temperatures allow for a lower measurement above the boiling point of liquid nitrogen (77 K), which is a convenient cold reservoir in our experiment.

---

[6] The experimental methods used to obtain these data are described in [2, §5.8].

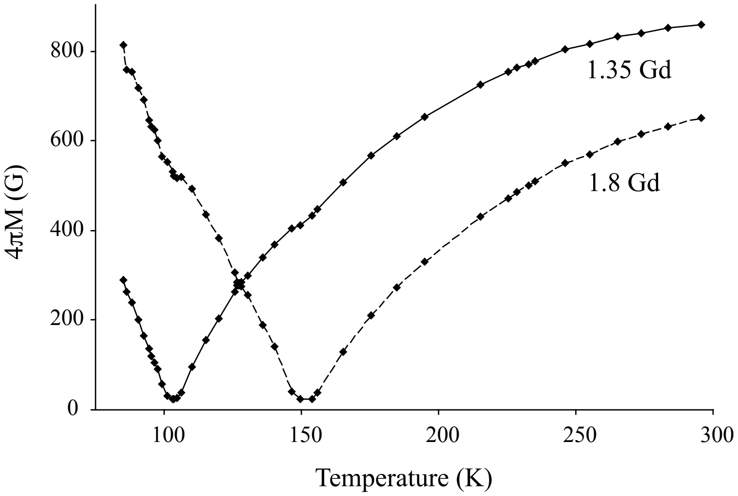

Figure 2.6: Magnetization of the toroid halves with temperature. (After [2, Figure 4.9]).

The intermediate region falls in the ideal operating range of JFETs, which are the high-impedance devices used in our detector; the upper temperature is fairly arbitrary. The three temperatures at which we operate are chosen to be 88 K, 127 K, and 178 K for these reasons. A schematic showing the relative magnetizations of the ions in the various sub-lattices in GdIG is shown in Figure 2.7. The positive and negative signs are chosen because $\mathbf{d}_e$ points towards positive charge by convention.

The physical toroid has a rectangular, vertical cross section. Its outer diameter is 4", inner diameter 2", and height 2". We have glued it to a ceramic mount that has extremely high resistance and a thermal expansion coefficient near that of GdIG. As the temperature of the apparatus is cycled from room temperature to its minimum point of 88 K, the mount tends to shrink with the GdIG, thereby reducing stress and limiting the possibility of fracture. Figure 2.8 shows the construction in schematic. The electrode plates are 0.002" thick copper attached to the sample with silver-doped, conductive epoxy.

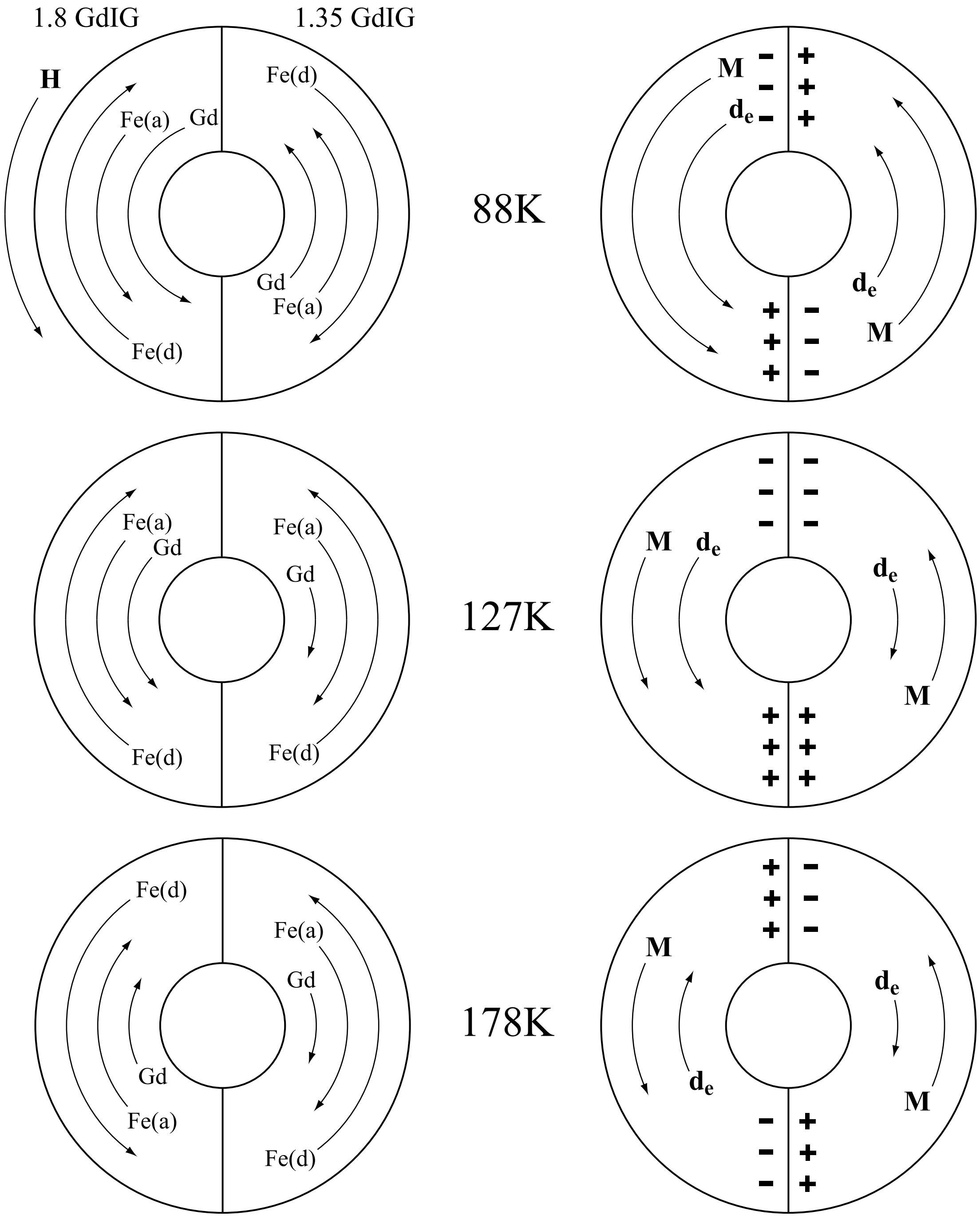

(a) (b)

Figure 2.7: Magnetization of the split toroid at different temperatures. (a) Magnetizations of the different sub-lattices. (b) Total magnetization and electron EDM.

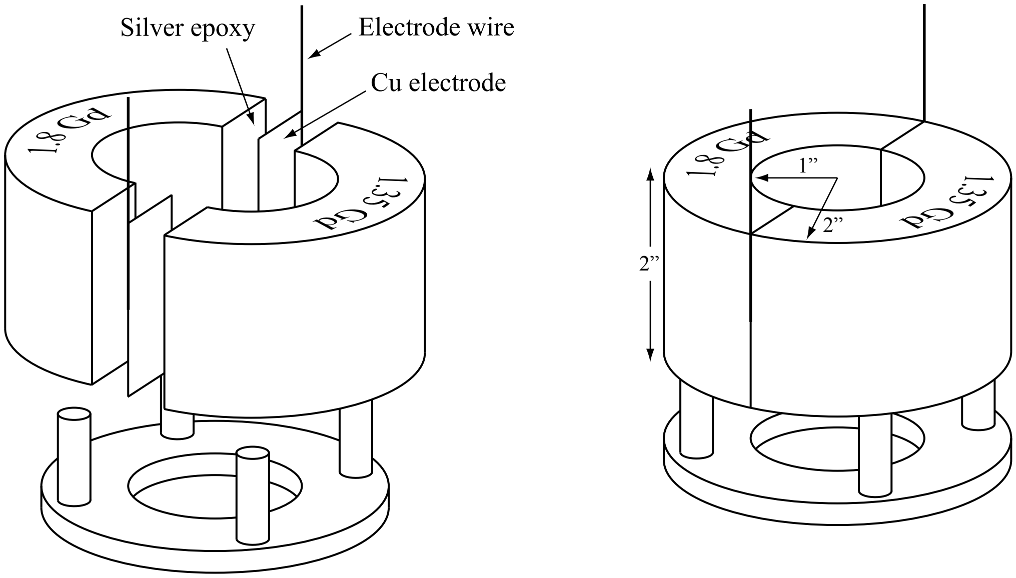

Figure 2.8: Schematic of the physical toroid.

2.3.3 Magnetization Calculations

It is instructive at this point to present a calculation of the predicted magnetizations of the different halves of our toroid. The actual data are presented in Figure 2.6, but we should have a basis for understanding if they are reasonable.

The magnetization of a material is defined as magnetic dipole moment per unit volume, or in terms of the applied field **H** and the flux density **B** as

$$\mathbf{M} = \frac{1}{\mu_0}\mathbf{B} - \mathbf{H}. \tag{2.16}$$

The magnetic moment can be expressed in many units, but a convenient choice is Bohr magnetons, as given in Figure 2.3 for each sub-lattice in GdIG. The figure shows that the total moment density depends on both the temperature and the gadolinium concentration. In fact, the contributions of the iron atoms change barely at all at low temperatures, and so any variation is due primarily to the gadolinium.

To calculate the magnetization we begin with the curves shown in Figure 2.3, and add up the individual contributions at a specific temperature and doping; let us choose the 1.8 Gd half at 100 K, as an example. The iron ions in lattice (d) contribute -15 μ_B and those in (a) 10 μ_B, for a total of -5 μ_B from iron. Gadolinium would contribute approximately 10 μ_B, but its concentration is decreased by a factor of $1.8/3 = 0.6$, so it contributes 6 μ_B. The total magnetic moment is therefore approximately 1 μ_B per formula unit. There are 3 Gd^{3+} per formula unit in GdIG, so the volume density of formula units is $n_{\mathrm{Gd}}/3$. (Recall from §2.2.2 that $n_{\mathrm{Gd}} = 1.235 \times 10^{22}$ atoms/cm^3 is the volume density of Gd^{3+} in pure GdIG.)

The magnetization of the 1.8 Gd half at 100 K is therefore

$$M \approx \left(\frac{1\ \mu_B}{\text{formula unit}}\right)\frac{1}{3}n_{\mathrm{Gd}}. \tag{2.17}$$

By directly substituting $1\ \mu_B = 9.274 \times 10^{-24}$ J/T and converting n_{Gd} to units of m^{-3}, we find the magnetization in SI to be

$$M = 3.8 \times 10^4\ \frac{\mathrm{A}}{\mathrm{m}}, \tag{2.18}$$

which has units of magnetic *field*. While this result is correct, expressing it in SI units is not typical. The preferred units are Gauss, which are the analogue of Tesla in Gaussian units (1 T = 10^4 G). Gauss and Tesla are units of magnetic *flux density*, so converting the above result to Gauss requires switching both to the new set of units and from field to flux density.

In Gaussian units the magnetization is given by

$$4\pi\mathbf{M} = \mathbf{B} - \mathbf{H}, \tag{2.19}$$

where the product $4\pi M$ is in units of Gauss, which takes care of the field to flux conversion. Therefore, we need only convert between SI and Gaussian field units, the conversion for which is 1 A/m = $4\pi \times 10^{-3}$ Oe [13, App. C]. Multiplying the result of Eq. 2.18 by this factor gives $4\pi M = 480$ G, in close agreement with the measured values of Figure 2.6.

Calculations of this sort, involving scaling the magnetization of the ions in GdIG differently, are used frequently in the final sections of this chapter, which deal with signal analysis. Before getting there, we will discuss the methods by which the sample is magnetized and the signal detected. This is a complicated process and merits a thorough examination.

2.4 Applied Field and Signal Detection

With a good sense of how the sample works magnetically, we now examine how its magnetization is periodically flipped and the signal detected. Because of the toroidal geometry and ferrimagnetic nature of the material, we do not bother to maintain the applied field during measurement. Instead, we magnetize the sample largely to saturation with a "pulse" of applied field, and then switch it off during data collection. When the sample magnetization flips, our circuity responds inductively with large pulses; the detector has been modified to deal with these problems.

2.4.1 Inductive Pulses and Optical Switches

Inductive pulses are simply a manifestation of Faraday's law, which relates time-varying magnetic fields and electrical potentials. The sample magnetization creates a large field that changes rapidly, so $\partial \mathbf{B}/\partial t$ is also large. The loops through which this changing flux occurs are not immediately obvious. They involve the detector circuitry and capacitance to ground in order to be complete, but they are very real. When the potential due to this changing flux appears on the input, it sends an extremely large signal to the detector, which decays quite slowly.

To counter these signals, a detector has been designed that incorporates optical

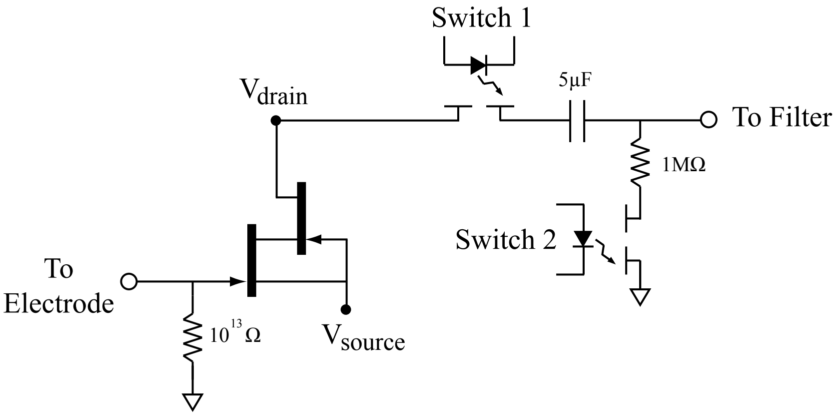

Figure 2.9: Optical switches isolate the second stage both from the electrode and from ground.

switches to isolate various stages of the circuit during the pulses (Figure 2.9). These switches have high input impedance, but nowhere near the range of our JFETs and 10^{13} Ω resistors. We therefore place them in the circuitry *after* the transistor outputs to maintain our high impedance to ground at the input. When a "blanking pulse" is sent to the detector, the switches open and provide an excellent signal block. Otherwise, they provide a negligible 7 Ω of resistance [33].

The first switch is located directly after the transistor output stage, blocking the rest of the circuitry from the signal. The second switch blocks the input of the second stage from ground, thereby preserving the signal level before the pulse. This reduces capacitive charging and discharging during the blanking period. The electrode signal ideally should change very little between pulses, so it is useful to maintain the charge on the capacitors.

2.4.2 Triggering Scheme

The overall sequence of events in magnetizing the sample and taking data is as follows:

Switches open → Field pulse → Switches close → Measure potential →
Reverse polarity → Repeat.

Our triggering scheme successfully accomplishes this by using one master function generator as the global sync. It sends out a square wave signal at some frequency f into a 555 timer circuit that emits a 5 ms pulse, which we refer to as the *sync pulse*. This pulse triggers two other function generators, one of which controls the switches (blanking) and the other the magnetic field. The blanking generator triggers at the beginning of the sync pulse, and opens the switches for approximately 50 ms. This length of time must be significantly longer than the pulse time, so that the detector sees as little of the inductive pulses as possible, but short enough that the data region is adequately long. The field generator triggers at the end of the sync pulse and turns the current on for approximately 12 ms. This time is chosen to allow the field generator to reach a current necessary to fully magnetize the sample. The overall triggering scheme for one field flip is shown in Figure 2.10a.

The blanking and field generators run at just over twice the frequency of the master generator, so that they complete one full cycle before the next sync pulse arrives (the difference is about 1%). The blanking pulses repeat normally, but the field pulses have an additional stage to alternate their signs. A DC current switch directs this process, taking current from a large current supply and directing it via the signal from the field pulse generator, but alternating the sign with its own, internal circuity. A diagram of this triggering scheme is shown in Figure 2.10b.

2.4.3 Signal Detection

The signal that we detect should be a slight potential asymmetry that is antisymmetric upon reversal of the applied field. The surface charge difference will be constant while the sample is magnetized in one direction, but our detector measures the potential relative to ground across a 10^{13} Ω resistor that does allow some charge to flow from the electrode plate. Each channel also has capacitance to ground of approximately 20 pF [2, §6.5]. The signal will therefore have an RC time of approximately

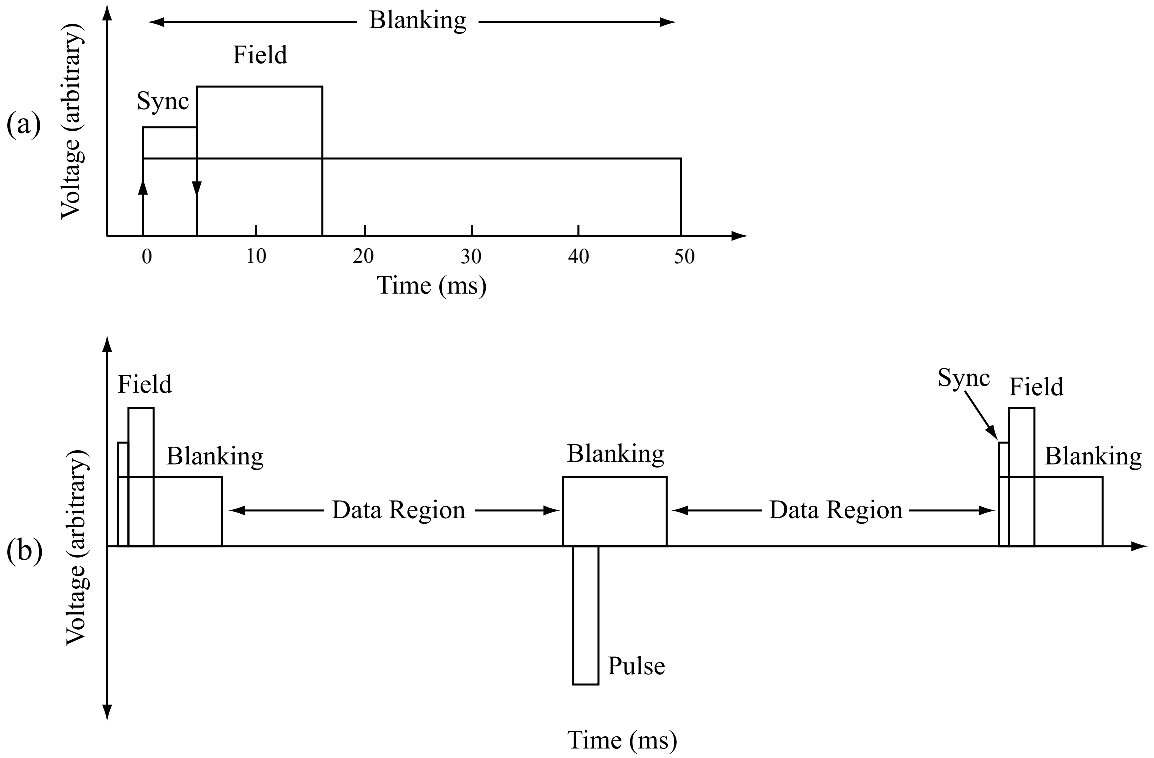

Figure 2.10: Triggering scheme for the pulsed waveform. (a) One cycle for positive field pulse, showing exact timing. (b) Extended plot showing complete process with a positive, negative, and another positive pulse.

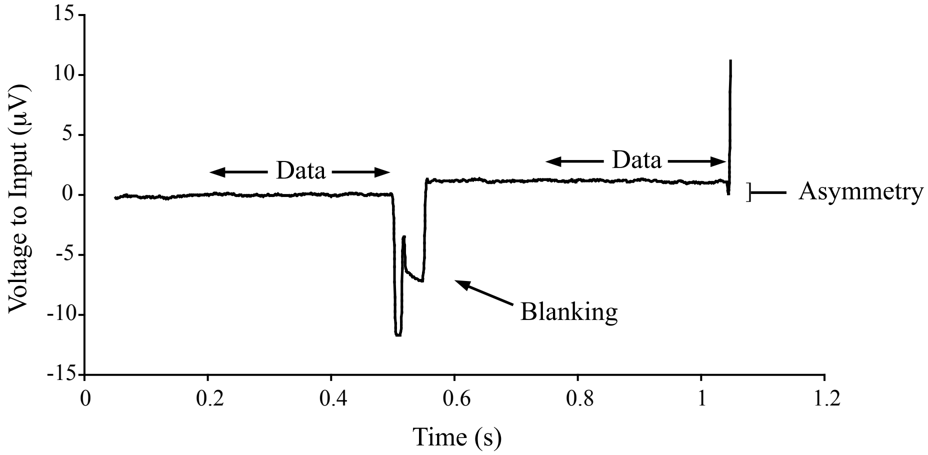

Figure 2.11: A typical trace taken at 2.3 Hz, showing both up and down pulses. This trace is averaged 512 times, and displayed voltages are compensated for gain.

$(10^{13}\ \Omega)(20 \times 10^{-12}\ \mathrm{F}) = 200$ s, and so the delay between pulses must be significantly less than this. However, we must also give time for the inductive pulses to decay, and the balance that we choose is a frequency between 1.2 and 2.3 Hz.

The detector measures each channel independently relative to ground; we designate them A and B. This is advantageous because the apparatus is intended to be perfectly symmetric, so any differences between the two channels point to accidental asymmetries. Each signal undergoes separate but identical amplification and filtration, and the final results are eventually subtracted on a computer. Figure 2.11 shows a typical trace taken at 127 K; the bumps near the middle are noise introduced by the optical switches, and the relatively flat regions provide the actual data.

The most common and harmful noise sources are microphonics, which are characterized as the signals created by charges physically oscillating in electrical fields. To address this, essentially anything that can move in the circuit has been bolted down, but ringing still occurs and creates havoc when it does. Physically preventing motion is the most effective way to reduce the signals, but once this approach has reached its limits we may electronically filter out certain pesky frequencies.

Acoustic noise, typically in the range of around 200–600 Hz, is especially irritating.

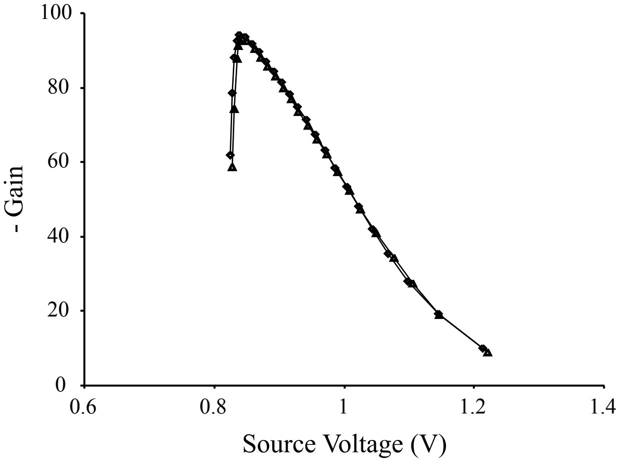

Figure 2.12: Gain of the pre-amplifier at 127 K as a function of gate-source voltage. (After [2, Figure 6.14].)

Our detector circuit therefore contains a five-pole Bessel filter designed to filter these frequencies. A discussion of complex impedances, transfer functions, and our detector filter can be found in appendix B, but for now we will mention the following results. The filter has its -3dB point at 80 Hz and by 200 Hz the gain has dropped to 1/10. There is minimal waveform distortion in the pass-band region because it is a Bessel filter, and acoustic noise is effectively filtered.

Total amplification from the detector is typically around -4,200. The first stage, known as the *pre-amplifier*, is kept within a temperature-controlled Faraday cage above the sample. Ben Heidenreich discusses the mathematics behind this circuit in his thesis [2, ch. 6], but the results are plotted in Figure 2.12. At 127 K, with the gate-source voltage held at approximately 0.95 V, the pre-amplifier has a gain of around -75. The second stage has a constant gain of 56 and is located outside of the apparatus. To analyze the signal we must account for these gains and discuss voltage at the detector *input*. Accordingly, all future analyses discuss voltage to the input unless otherwise specified.

2.5 Data Analysis

A complete data set includes measurements made at a variety of temperatures, field strengths, and sample orientations. We therefore cycle the sample temperature between the three operating points, 88 K, 127 K, and 178 K, and take averaged data at varying maximum field strengths. We then warm the apparatus to room temperature, rotate the toroid by 180°, and repeat the process. This procedure allows us to correct for asymmetries due to temperature fluctuations and sample orientation, significantly increasing our resolution.

2.5.1 Fitting the Data

Data are taken at various maximum values of the applied field because we find that the measured potential asymmetry varies with the magnetization of the sample, decreasing at higher fields. An EDM potential should do just the opposite, and *increase* as more dipoles align. The measurements are well described by a function of the form

$$\Delta V_{asym} = \frac{a}{H_{max}} + \Delta V, \tag{2.20}$$

where H_{max} is the maximum value of the applied field, and a and ΔV are fit parameters. We select this fit because the decay appears related to the overall magnetization of the sample, and the magnetization of materials approaching saturation fits a function of the form [34]

$$M = M_0 - \frac{b}{H} - \frac{c}{H^2}. \tag{2.21}$$

Including the last term increases variation in the other parameters and yields a poor description of our data, so we neglect it. Theoretically, we expect the potential asymmetry to be independent of the magnitude of the applied field, when the sample is magnetized. Therefore, in Eq. 2.20, a should be zero and ΔV should correspond

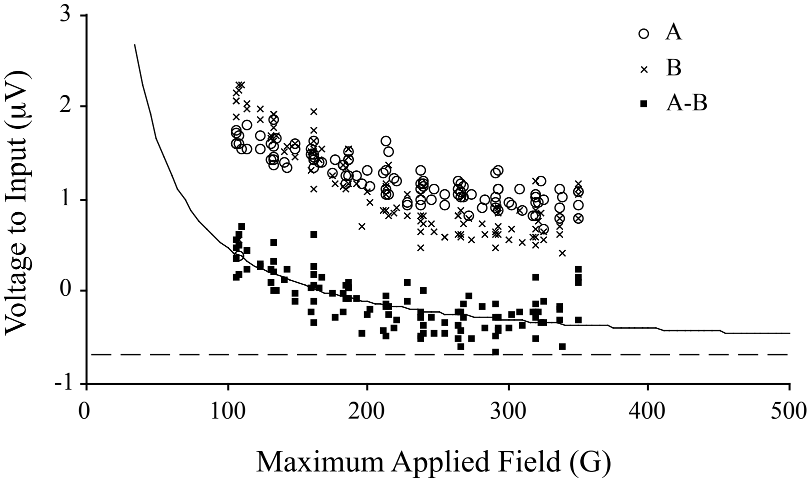

Figure 2.13: Asymmetry versus field data at 127 K from summer 2006. The solid line is the a/H fit, and the dashed line the high field asymptote ΔV.

directly to the EDM potential. However, a is non-zero and we must fit the data to extrapolate to the "high field" limit where $\Delta V_{asym} \approx \Delta V$. Figure 2.13 shows a typical plot of asymmetry versus field at 127 K; these data were part of the complete set used to establish our current limit in the summer of 2006.

In the past this fit has worked well to describe the gathered data, but, after several changes were made to the sample in early 2006, the decay became smaller and less clear. The data are improved and the calculated limit on d_e has dropped by a factor of four, but the trends are less obvious. The changes that were made to the sample are discussed in chapter 3.

2.5.2 Sensitivity to the EDM

We must now calculate the connection between the calculated, high-field asymmetry ΔV and the magnitude of the electron EDM. This potential depends on the electrical polarization of the sample, which in turn depends on the magnetization of gadolinium. The latter varies both with temperature and the concentration of Gd, so we must account for these effects.

The electrical polarization of a magnetized sample of GdIG due to the electron EDM is given by Eq. 2.13, as calculated by Mukhamedjanov *et al.* It states

$$P = 3d_e n_{\mathrm{Gd}}, \tag{2.22}$$

where d_e is the magnitude of the electron EDM and n_{Gd} is the number density of Gd^{3+} ions in GdIG. In our experiment, we use differently doped samples at a variety of temperatures, so this polarization must be scaled appropriately. Four principle effects contribute to these changes:

1. **Temperature:** The magnetic alignment of Gd decreases with increasing temperature.
2. **Doping:** The concentration of Gd is different in each half of the toroid.
3. **Flux matching:** The magnetizations of the two halves vary differently with temperature, so they are in general not matched in their flux.
4. **Pulsed field:** The magnetic field is turned off during measurement, so magnetization is not externally maintained.

The **temperature dependence** of gadolinium magnetization can be determined by comparing the magnetization at a given temperature to that at $T = 0$ K.[7] From Figure 2.3, we find approximate values at the operating temperatures, as listed in Table 2.1. The function representing the relative magnetization of Gd as a function of temperature will be assigned the name $R(T)$.

Doping scales the polarization by the relative concentration of Gd^{3+} ions. In our sample, this decreases n_{Gd} by a factor of $1.8/3 = 0.6$ in one half, and $1.35/3 = 0.45$

---

[7] Recall that gadolinium behaves paramagnetically in the field created by the iron ions in GdIG, so its magnetization varies roughly as $1/T$.

Temperature	μ_B/formula unit	Relative Gd Magnetization
0 K	21	1
88 K	11	0.5
127 K	8	0.4
178 K	6	0.3

Table 2.1: Gadolinium magnetization at the operating temperatures, from Figure 2.3. Magnetic moments have been approximated to the nearest integer value.

in the other. This scaling will be represented by the variable c, and its effects are plotted in Figure 2.14a.

Flux matching is the result of different gadolinium concentrations in the two halves of the toroid. Each has a different magnetization at any given temperature (Figure 2.6), so, when the applied field dissipates, the unmatched poles at the electrodes create demagnetizing fields. Observation shows that the magnetization of the more magnetized half rapidly decreases to match the level of the lesser. At 88 K, which is below both compensation temperatures, the relative magnetization is determined by Gd concentration; the 1.35 side is less magnetized because it has fewer Gd per formula unit. At 127 K the magnetizations are equal (it was chosen for this reason), and at 178 K, which is above both compensation temperatures, the 1.8 side is less magnetized because more gadolinium ions oppose the iron (d) ions. These predicted magnetizations are plotted in Figure 2.14b. To mathematically describe the decrease that results from flux matching, we introduce the function $\lambda(T)$, defined by

$$\lambda(T) = \left| \frac{M_{1.8}(T)}{M_{1.35}(T)} \right|, \tag{2.23}$$

where $M_{1.8}$ and $M_{1.35}$ are the predicted magnetizations before flux matching (Figure 2.14c). The magnetization of the stronger side is scaled by λ appropriately so that it equals that of the weaker side. In the temperature region $0\text{ K} < T < 127\text{ K}$, $M_{1.8}$ must decrease to equal $M_{1.35}$ and so we scale it by $\frac{1}{\lambda}$. Above 127 K we must scale

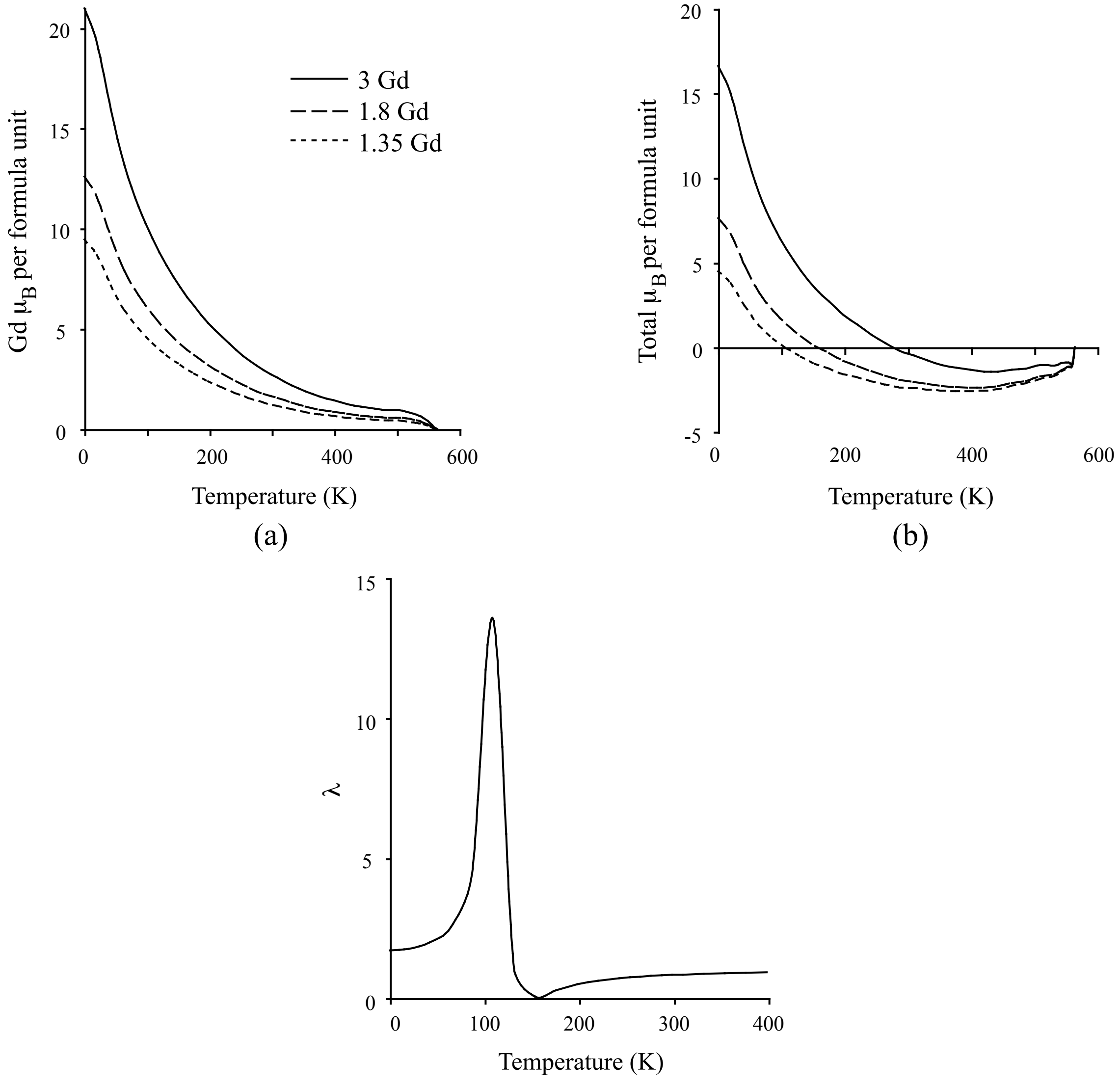

(a)

(b)

(c)

Figure 2.14: Plots of various scalings to the EDM polarization. (a) Doping decreases the total magnetization due to Gd^{3+}. (b) Total magnetization of each half; flux matching sets M at that of the less magnetized half. (c) Continuous values of λ, the ratio of unmatched magnetizations.

down $M_{1.35}$ directly by λ. These results are summarized below:

Temperature Range	Effective Magnetizations
$T < 127$ K	$M'_{1.8} = \frac{1}{\lambda} M_{1.8}, \quad M'_{1.35} = M_{1.35}$
$T > 127$ K	$M'_{1.8} = M_{1.8}, \quad M'_{1.35} = \lambda M_{1.35}.$

Pulsing the applied field allows the sample to partially demagnetize before data are collected. This is mainly because the polycrystalline sample comprises many magnetic domains, each of which has its preferred axis oriented in a different spatial direction. An applied field can push these magnetizations closer into alignment, but, when it dissipates, the moments relax and **M** partially decreases. We observe a 23% decrease due to this effect, such that the total remaining magnetization is only 77% of that of the lesser magnetized half [2, §7.6]. We will symbolize this demagnetization by the factor D.

2.5.3 Scaling Factors

If we consider all of the above four effects (temperature variation, doping, flux matching, and pulsed field) as factors that scale the EDM polarization, then **P** can be re-expressed as

$$\mathbf{P} = \big(Rc\lambda' D\big) 3 d_e n_{\mathrm{Gd}} = 3\gamma_c^T n_{\mathrm{Gd}} d_e. \tag{2.24}$$

Here R represents the relative magnetization of Gd^{3+} in pure GdIG as a function of temperature, c is the doping factor, λ' symbolizes the effect of flux matching (multiplication by λ, if necessary), and D is the demagnetization factor. The temperature- and doping-dependent variable $\gamma_c^T = Rc\lambda' D$ has been introduced to keep track of the product of these four factors. From now on, we will refer to the γ_c^T as *scaling factors*.[8]

Before continuing to calculate explicit values of the scaling factors, let us establish a sign convention. Figure 2.7 shows that at 88 K the EDMs align parallel to **M**; we

---

[8] Superscripts will be used to indicate the temperature at which a variable is evaluated, and subscripts will generally indicate the doping of GdIG, where 3 is the maximum.

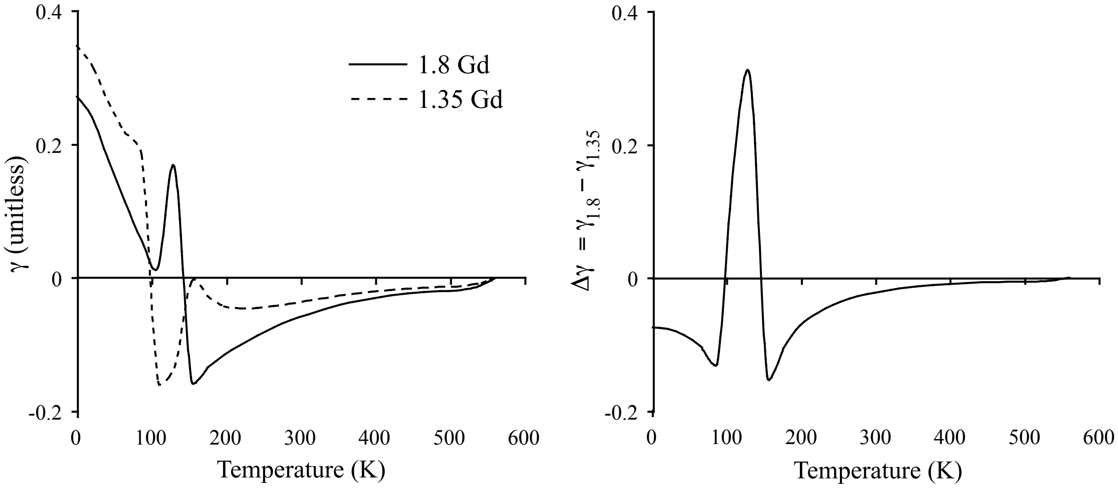

(a) (b)

Figure 2.15: Scaling factors for the EDM signal over the range of temperatures. (a) γ_c^T of each half of the toroid. (b) Difference in scaling factors, $\Delta\gamma^T = \gamma_{1.8}^T - \gamma_{1.35}^T$.

will take this direction to be *positive*, such that each half flips to negative polarization above its compensation temperature. (The sign of the γ_c^T is therefore the same as the sign of M_c^T from Figure 2.14b.) Accounting for this sign convention, we calculate the scaling factors as shown in Figure 2.15a.

With a sign convention established, we may now examine the behavior of induced surface charges and charge flow on the electrodes.

2.5.4 Electrodes and Capacitance

When an EDM polarization forms in the sample at a given temperature, it induces surface charge density on the ends of the toroid halves, as in Figure 2.7. This charge density is given formally by Eq. 2.1, which states

$$\sigma_b = \mathbf{P} \cdot \hat{\mathbf{n}}. \tag{2.25}$$

The sample magnetization is toroidal overall, but perpendicular to the electrode plates, such that $\hat{\mathbf{n}}$ is parallel to $\mathbf{P}$. The surface charge at the electrode due to the EDM polarization is therefore equal to P. Additionally, each electrode sees surface charge from both halves of the toroid, so according to our sign convention the total electric charge should be

$$\Delta q^T_{edm} = \left(\sigma^T_{1.8} - \sigma^T_{1.35}\right) A = \left(P^T_{1.8} - P^T_{1.35}\right) A, \tag{2.26}$$

where $A = 11.7\ \mathrm{cm}^2$ is the area of the plate, and the P^T_c are the EDM polarizations. However, the presence of electrodes introduces free charge into the system, which fundamentally alters the calculation.

The bound charge due to P will induce free charge flow q_f onto the electrodes, which will in turn induce a dielectric response in the GdIG. This response reduces the internal field due to the free charge, $\mathbf{E}_f$, by a factor of $\kappa = \chi + 1$.[9] For convenience, we define the *effective charge* to be the free charge that must flow from one electrode to the other in order to to fully cancel out the signal between them.[10]

If we approximate the assembly as a parallel plate capacitor, then the relationship between the free charge q_f and the electric field $\mathbf{E}_f$ that it creates is quite simple:

$$E_f = \frac{1}{\epsilon_0}\sigma_f = \frac{q_f}{\epsilon_0 A}, \tag{2.27}$$

where A is the area of one of the capacitor plates. The EDM polarization is approximately uniform within the sample, and therefore creates a field given by Eq. 2.14, which here states

$$\mathbf{E}_{\mathrm{edm}} = -\frac{1}{\epsilon_0}\mathbf{P}_{\mathrm{edm}}, \tag{2.28}$$

where $\mathbf{P}_{\mathrm{edm}} = 3n_{\mathrm{Gd}}d_e\hat{\sigma}_{\mathrm{Gd}}$ is the polarization calculated in Eq. 2.13. (We recall that this polarization already considers the dielectric response of GdIG to the alignment

---

[9] Both GdIG and YIG have approximately the same dielectric constant, so κ should be the same for each half of the toroid [30, 35].

[10] This definition derives from [2, §2.7–8].

of the electron EDMs.) Substituting the field in Eq. 2.27 for $\mathbf{E}_{\mathrm{edm}}$ above, we find the free charge that will cancel the field due to the EDM polarization to be $q_f = P_{\mathrm{edm}}A$. The effective charge is a factor of κ larger than this:

$$q_{\mathrm{eff}} = \kappa P_{\mathrm{edm}} A. \tag{2.29}$$

The product κP_{edm} is referred to as the *effective polarization* in the previous work.

The effective charge that flows onto the electrodes due to the EDM polarization, at a particular temperature, is given by

$$\begin{aligned}\Delta q_{\mathrm{eff}}^T &= 2\kappa\left(\sigma_{1.8}^T - \sigma_{1.35}^T\right)A = 2\kappa\left(P_{1.8}^T - P_{1.35}^T\right)A \\ &= 6\kappa n_{\mathrm{Gd}} d_e A\left(\gamma_{1.8}^T - \gamma_{1.35}^T\right). \end{aligned} \tag{2.30}$$

The factor of two has been added because the polarizations flip from negative to positive during measurement, so twice the charge must flow. The negative sign arises because of our sign convention, which states that the EDM polarizations are parallel at 88 K, and therefore will point *oppositely* at an electrode plate. For clarity, let us state this directly: *the direction of the EDM relative to its 88 K direction is contained within the scaling factor*. Eq. 2.30 should hold at every temperature provided that we have been careful when evaluating the γ_c^T.

It is therefore the difference in scaling factors in which we are interested; a plot of these values is shown in Figure 2.15b. From this plot, we find the *differential sensitivities* to the EDM at each operating temperature, relative to $\gamma_3^{0\mathrm{K}} = 1$. The approximate values are listed in Table 2.2.

The actual circuit within our apparatus can be modeled by treating the electrodes as capacitors to ground, connected together by a capacitance due to the detector. This circuit is shown in Figure 2.16. Ben Heidenreich explicitly calculates the relationship

Temperature	$\gamma_{1.8}$	$\gamma_{1.35}$	$\Delta\gamma = \gamma_{1.8} - \gamma_{1.35}$
0 K	0.25	0.35	-0.1
88 K	0.05	0.2	-0.15
127 K	0.15	-0.15	0.30
178 K	-0.15	-0.05	-0.1

Table 2.2: Scaling factors γ_c^T at the various operating temperatures.

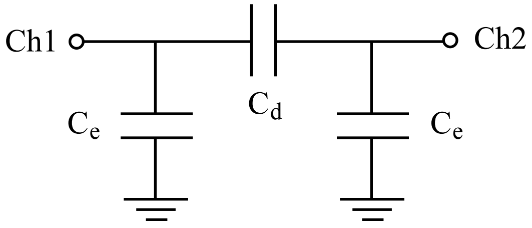

Figure 2.16: Circuit diagram of the electrodes as capacitors to ground. C_e are the electrode capacitances, and C_d is the capacitance between the electrodes.

between the effective charge Δq_{eff} and the potential ΔV on the electrodes in his thesis, and finds

$$\Delta V = \frac{\Delta q_{\mathrm{eff}}}{C_e + C_g/2}, \tag{2.31}$$

where $C_e = 3.5$ pF is the capacitance between the electrodes, due to the sample and the detector circuitry, and $C_g = 20$ pF is the capacitance of each electrode to ground.[11] By combining this result with Eq. 2.30 and rearranging slightly, we find

$$\Delta V^T = \frac{6\kappa n_{\mathrm{Gd}} A}{C_d + C_e/2}\left(\gamma_{1.8}^T - \gamma_{1.35}^T\right) d_e. \tag{2.32}$$

Direct substitution of the values $\kappa = 15$ [35, 30], $A = 11.7$ cm^2, $n_{\mathrm{Gd}} = 1.235 \times 10^{22}$ atoms/cm^3, $C_d = 3.5$ pF, and $C_e = 20$ pF simplifies Eq. 2.32 to the more applicable form

$$\Delta V^T = \left(1.7 \times 10^{17} \,\frac{\mathrm{V}}{e\ \mathrm{cm}}\right)\left(\gamma_{1.8}^T - \gamma_{1.35}^T\right) d_e, \tag{2.33}$$

where the constant has been adjusted so that d_e is in units of e cm.

---

[11] This equation is from §7.1, but draws on earlier calculations from §4.9 [2].

Eq. 2.32 in principle will yield a value of the electron electric dipole moment at any temperature we choose, provided that ΔV^T is due entirely to the EDM polarization. This is extremely unlikely; in fact, all of the data points taken over the summer of 2006 would have yielded non-zero EDMs on the order of 10^{-23} e cm had we analyzed the data by only this method. Rather, we combine the data in such a way as to subtract any first-order, non-EDM potentials due to sample orientation and temperature. We now describe these analyses.

2.5.5 Data Analysis and Basic Systematics

A complete data set comprises measurements of ΔV_{asym} (from Eq. 2.20) at every combination of operating temperature and sample orientation, and at many values of H_{max}. We cycle the sample temperature between 88 K, 127 K, and 178 K, and flip the orientation of the sample between two states. H_{max} varies between $100 \text{ G} < H < 350 \text{ G}$ in roughly 25 G intervals, for a total of at least 10 values. This leads to a total data set of at least 60 values of ΔV_{asym}, and typically many more for improved statistics.

The potential asymmetries versus applied field, at constant temperature and sample orientation, are fit to Eq. 2.20, from which we obtain a "high field" value of ΔV^T. (The superscript T has been added because we now see that this value is a function of temperature.) There are six combinations of temperature and sample orientation, for a total of six ΔV^T. As previously mentioned, these data do not yield consistent values of d_e from Eq. 2.33 until they are combined to remove zeroth- and first-order effects in temperature and sample orientation. Suppose, then, that each of the measured asymmetries ΔV^T actually comprise four terms, given by

$$\Delta V^T = \Delta V^T_{edm} + O + (\alpha T + \beta), \tag{2.34}$$

where ΔV^T_{edm} indicates the asymmetry due to the EDM polarization, and is the value that eventually will be used in evaluating Eq. 2.33. Here O is a term that switches sign upon reversal of the toroid, and $(\alpha T + \beta)$ accounts for offsets that are linear and constant in the temperature. Other terms may perturb our results, including high-order terms in T, but we may at least deal with those given above.

We account for the **sample orientation** term O by averaging the values of ΔV^T at each orientation, to get something between the two that is probably more accurate. Rotating the toroid switches the inputs at the detector (e.g. channel A of the sample corresponds to channel B of the detector), so we switch the sign of the reversed measurement to compensate, such that

$$\Delta V^T_{avg} = \frac{1}{2}\Big(\Delta V^T_{normal} - \Delta V^T_{reversed}\Big). \tag{2.35}$$

To eliminate the **temperature** dependent terms, we must have measurements at three temperatures equally spaced by some amount $\Delta T = \epsilon$. Subtracting the average of the lower and higher measurements from the middle one, all non-EDM terms vanish from ΔV^T_{avg}. The temperatures 88 K, 127 K, and 178 K *approximately* satisfy this condition, with $\epsilon \approx 45K$. The data combination used to eliminate these effects is therefore

$$\Delta V^{127\text{K}}_{avg} - \frac{1}{2}\Big(\Delta V^{88\text{K}}_{avg} + \Delta V^{178\text{K}}_{avg}\Big) = \Delta V^{127\text{K}}_{edm} - \frac{1}{2}\Big(\Delta V^{88\text{K}}_{edm} + \Delta V^{178\text{K}}_{edm}\Big), \tag{2.36}$$

where the left side involves measured data, and the right side purely EDM potentials.

Eq. 2.33 gives the relationship between the measured potential asymmetry due to the EDM and the magnitude of d_e, so combining this with Eq. 2.36 we find

$$\Delta V^{127\text{K}}_{avg} - \frac{\Delta V^{88\text{K}}_{avg} + \Delta V^{178\text{K}}_{avg}}{2} = \left(1.7 \times 10^{17}\ \frac{\text{V}}{e\ \text{cm}}\right)\left(\Delta\gamma^{127\text{K}} - \frac{\Delta\gamma^{88\text{K}} + \Delta\gamma^{178\text{K}}}{2}\right) d_e,$$

where $\Delta\gamma^T = \gamma^T_{1.8} - \gamma^T_{1.35}$. Substituting these values from Table 2.2 and isolating d_e, we find the final result for the relationship between the extrapolated, high-field asymmetries, averaged over orientation, and the electron EDM:

$$\boxed{d_e = \left(1.8 \times 10^{-17}\ \frac{e\ \mathrm{cm}}{\mathrm{V}}\right)\left(\Delta V^{127\mathrm{K}}_{avg} - \frac{1}{2}\left(\Delta V^{88\mathrm{K}}_{avg} + \Delta V^{178\mathrm{K}}_{avg}\right)\right).} \tag{2.37}$$

These are the mathematics used in analyzing the asymmetry data that we collect. As previously mentioned, the ΔV^T reflect potentials at the *input*. Measured potentials must therefore be scaled to compensate for gain, which is typically around -4,200 total as discussed in §2.4.3. We now present the most recent data set, both to serve as an example of how the preceding methods are used, and also to establish the current status of the experiment.

2.6 Present Limit

The sample was last cooled down in July and August of 2006, when a complete set of data was taken. Three major modifications had been made to the sample since the previous cool down. First, 3/16" was ground off of the top, where the 1.8 Gd half had been chipped after arriving at the Los Alamos receiving room. Secondly, the electrodes were completely reconstructed. New wires were soldered rigidly to the electrode plates, fixing a break in channel A that occurred in the preceding years. The plates were thickened from 0.001" to 0.002" copper, and were re-attached to the sample with a different epoxy.

The data for these cool downs (one with each sample orientation) are shown in Figure 2.17, and the calculated values of ΔV^T and ΔV^T_{avg} are shown in Table 2.3. These data yield a limit on d_e, according to Eq. 2.37, of

$$d_e = (-0.18 \pm 1.33) \times 10^{-24}\ e\ \mathrm{cm}. \tag{2.38}$$

Temperature	Orientation	ΔV (μV)	ΔV_{avg} (μV)
88 K	normal	-0.05 ± 0.13	0.48 ± 0.09
	reversed	-1.01 ± 0.13	
127 K	normal	0.70 ± 0.05	0.45 ± 0.05
	reversed	-0.19 ± 0.08	
178 K	normal	0.10 ± 0.08	0.43 ± 0.07
	reversed	-0.76 ± 0.11	

Table 2.3: Data from the summer of 2006. Potentials are compensated for gain to reflect the signal at the input. ΔV for the reversed orientation are shown as measured, but in the average their signs switch.

We set a limit on the size by assuming that d_e must be less than its highest possible value, and so our reported result is

$$\boxed{|d_e| < 1.5 \times 10^{-24}\ e\ \text{cm.}} \tag{2.39}$$

As previously mentioned, this is three orders of magnitude larger than the world limit, but it represents improvement by almost a factor of four over the previous result published in December 2005 [1].

The data in Table 2.3 show a dependence on sample orientation. Consider, for example, the measurements at 88 K. Reversing the orientation takes ΔV from 0.05 to 1.01 μV, an increase of almost twenty fold; this trend is also apparent at the other temperatures. If we average to account for sample orientation, then this dependence is significantly reduced. Nevertheless, it is indicative of troubling asymmetries within the apparatus.

The most important systematic effect evident from these data is what we refer to as the *M-even effect*, which we believe to be the source of the observed $1/H$ decay of ΔV. This effect is a potential asymmetry that is symmetric upon reversal of the magnetic field and therefore does not display the same sign-dependence as the EDM potential. However, the effect is not identical on the two channels. Chapter 3 discusses the properties of this effect in greater detail.

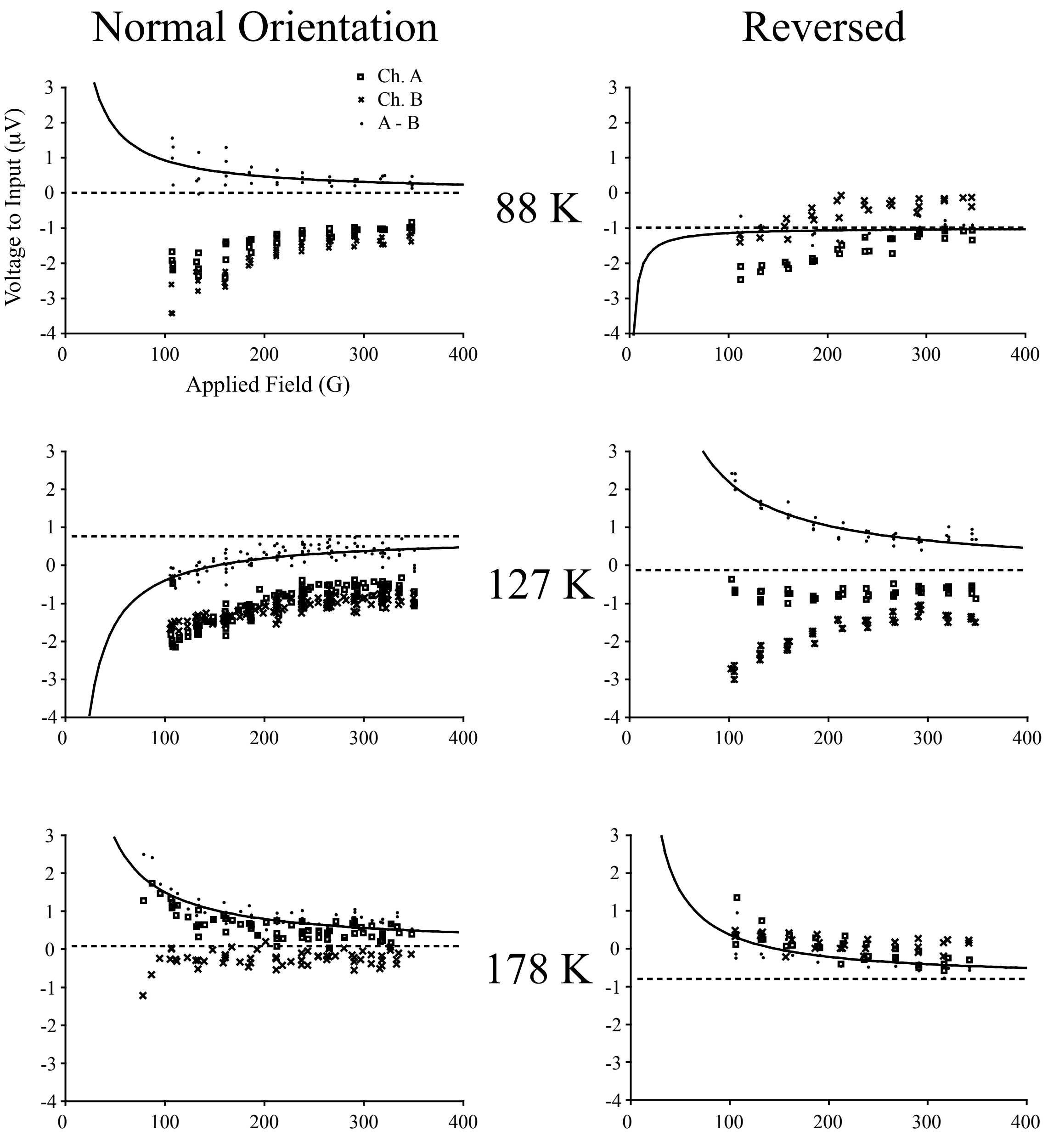

Figure 2.17: Asymmetry versus field plots from the summer of 2006. The solid curves are regressions according to Eq. 2.20, the data for which are given in Table 2.3.

Chapter 3

M-Even Effect

This chapter discusses many characteristics of the particular systematic effect on which all current work has focused. The qualities of so-called “symmetric” and “antisymmetric” effects are discussed in the context of our experiment, along with relevant examples. We then proceed to characterize the effect as it is currently understood, explaining methods that have been adopted to minimize the disturbance.

3.1 Symmetric and Antisymmetric Effects

To begin a discussion of systematic effects, we should address some initial vocabulary. First let us distinguish between *effects* and *noise*. The former are reproducible, yet undesirable and often mysterious, signals that somehow end up on our oscilloscope during data collection. The latter is defined vaguely as small, irreproducible fluctuations that are, above all else, not correlated to the signal of interest. This becomes a little hazy when dealing with microphonic ringing, but we tend to isolate that in its own category.

Noise can be significantly reduced by averaging over long periods of time. This works because the noise signals have no phase or frequency relationship to the experimental signal, and so after sufficient iterations their sum approaches zero. However, the most effective approach is always either to shield the apparatus from the signal, or to reduce the noise at its source. For example, to free our system of 60 Hz oscillations due to the wall voltage, we place the apparatus in a Faraday cage. Other noise sources, such as Johnson noise and shot noise, plague any real electrical system; both of these are described at length in Ben's thesis [2, ch. 4].

Systematic effects are distinguishable from noise because they are not random, and averaging does nothing to reduce their signal size. Instead, they perturb the signal in such a way that either the system must be physically changed or the data cleverly subtracted. A few examples of these are described in §2.5.5; data analysis does well at eliminating these effects, but we would do better if they weren't there in the first place.

Effects may also be characterized by their symmetry. *Symmetric* (even) effects are identical after something has been reversed, whereas *antisymmetric* (odd) effects switch sign. Mathematically, this says that for some symmetric and antisymmetric functions $f_{sym}(x)$ and $f_{anti}(x)$, taking $x \to -x$ gives

$$f_{sym}(-x) = f_{sym}(x), \tag{3.1}$$

$$f_{anti}(-x) = -f_{anti}(x). \tag{3.2}$$

If we have some composite function $f = f_{sym} + f_{anti}$, we may isolate its contributions with the following identities:

$$f_{sym}(x) = \frac{1}{2}\big(f(x) + f(-x)\big), \tag{3.3}$$

$$f_{anti}(x) = \frac{1}{2}\big(f(x) - f(-x)\big). \tag{3.4}$$

Figure 3.1 shows one such signal and its decomposition.

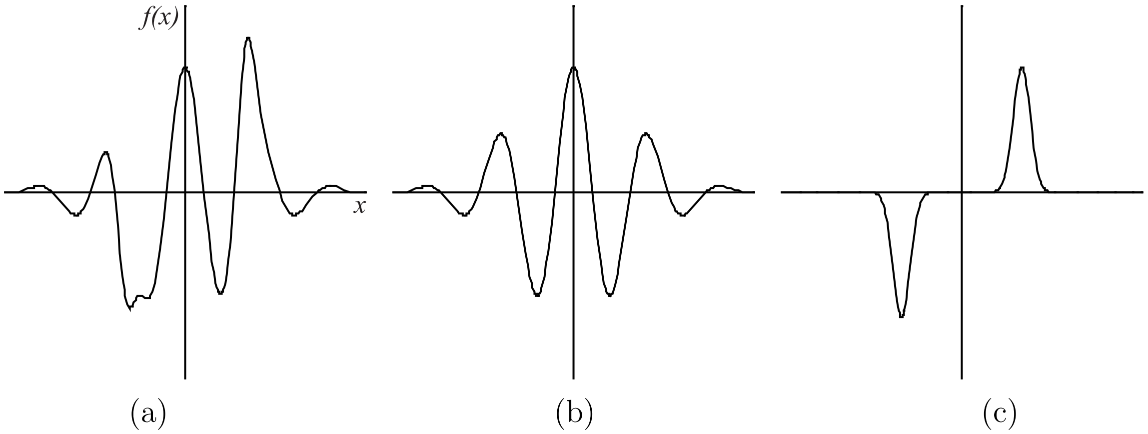

Figure 3.1: Any function can be broken down into symmetric and antisymmetric contributions: (a) total function, (b) symmetric contribution, and (c) antisymmetric contribution.

To decompose a signal in the manner of Eqs. 3.3 and 3.4, the physical variable represented by x and its origin must be chosen. Regarding the current work, we choose the strength of the applied field and the point $\mathbf{H} = 0$, respectively. Both the EDM signal and inductive pulses, for example, are antisymmetric signals.

As discussed in the previous chapter, our apparatus and methods of data analysis are designed to eliminate many non-EDM effects, both symmetric and antisymmetric. **Offsets** are even because they remain unchanged upon reversal of either the applied field or the sample orientation; each is separately considered. The EDM signal is odd upon the reversal of **sample orientation**, so we average the odd contributions from each orientation. **Temperature** effects can be even and odd because we account for both linear and constant terms, and these can be modeled by purely even and odd contributions.

The apparatus is also designed with symmetry in mind; specifically, it is largely symmetric under rotation about the vertical axis.[1] This places the two electrodes in similar environments and ensures that each undergoes identical amplification and fil-

---

[1] This requires qualification: much of the apparatus is continuously symmetric under such rotation, but the circuitry is only symmetric under 180° rotation.

tration. However, despite these internal symmetries, a symmetric effect has bothered us for the past year.

3.2 Even Systematic

We have already encountered the most profound evidence for this systematic in the previous chapter, when discussing the $1/H$ decay of the measured voltage asymmetry (§2.5.1, Eq. 2.20, Figure 2.13). This behavior is present on each channel separately, but not identically; hence, subtracting the data decreases, but does not eliminate, the effect.

These data compare the measured voltage asymmetry to the maximum strength of the applied field, but each point is collected separately. We have found that a more revealing (and much faster) method for measuring the effect is to use a triangular, field waveform because it progresses through all field strengths linearly. A plot of the signal under these conditions is shown in Figure 3.2. The detector signal is clearly asymmetric, yet we would expect it to be perfectly antisymmetric with contributions from both the inductive pulses and the EDM potential. Before decomposing the signal into its symmetric and antisymmetric parts, we must understand precisely what the curves imply.

3.2.1 Hysteresis

As discussed in §2.4.1, when the GdIG toroid's magnetization flips, the surrounding circuitry responds inductively with large pulses. The field coil surrounding the sample also responds, as Figure 3.2 shows. Notice that the field trace suffers a slight perturbation to its linearity after the points at which $H = 0$. This is evidence of sample *hysteresis*, which is the tendency of a system not to follow immediately the forces applied to it [32, §2.1]. Ferromagnetic materials, for example, exhibit hysteresis

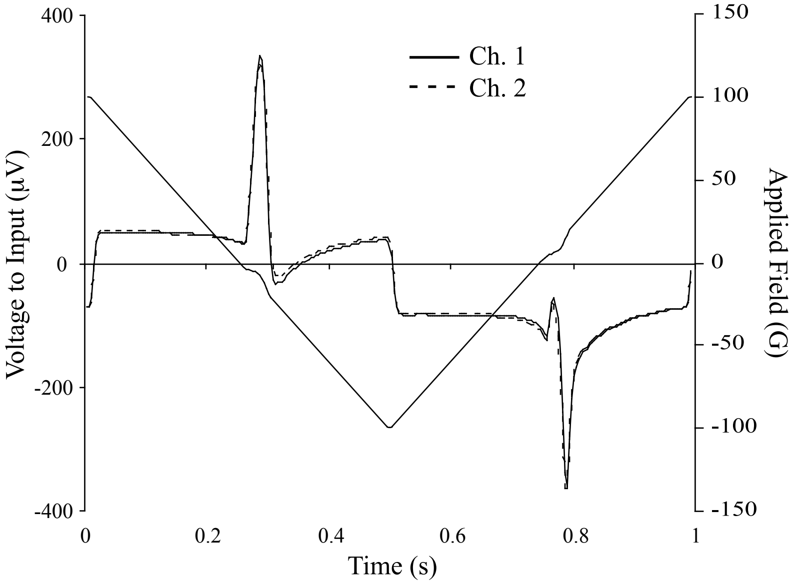

Figure 3.2: Output signal when the applied field has a triangular waveform (127 K, $H_{max} = 100$ G, $f = 1.02$ Hz, from summer 2006). The applied field is the triangular curve, scaled against the secondary axis.

because they have spontaneous moments in the absence of applied fields. They resist demagnetizing until H has reached a material-specific level known as the *coercive field*, H_c.

The distinction between paramagnetism and ferromagnetism can be recast in terms of hysteresis.[2] Paramagnets exhibit no hysteretic effects because they fully demagnetize as the applied field drops to zero. Ferromagnets resist these changes until their temperature reaches the Curie point. The magnetization of ferromagnets is therefore a function of more than H; it depends on the magnetic history as well. A *hysteresis loop*, such as Figure 3.3, shows the behavior of magnetization as the applied field changes, and may be divided into the following segments.

1. $\mathbf{H}$ increases positively from zero and $\mathbf{M}$ saturates.

2. $\mathbf{H}$ decreases to zero but $\mathbf{M}$ remains largely unchanged.

---

[2] Recall that our ferrimagnetic material behaves ferromagnetically, except that the gadolinium ions have paramagnetic temperature dependence. A hysteresis loop for the GdIG toroid is shown in Figure 6.1.

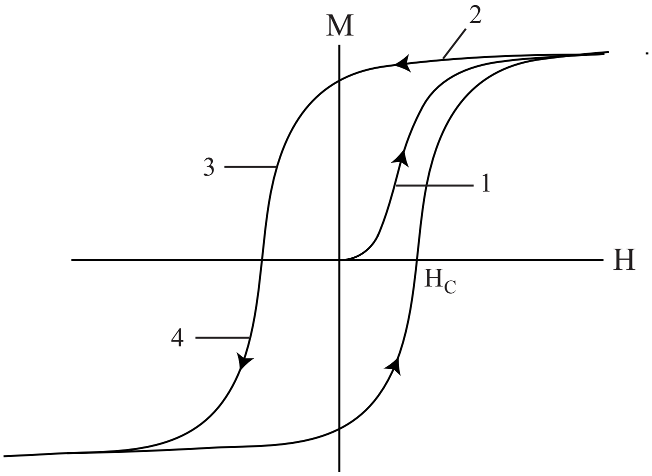

Figure 3.3: Hysteresis loop for ferromagnetic materials. (After [32, Figure 2.3].)

3. **H** reaches the coercive field and **M** drops to zero.
4. **H** decreases to its minimum and **M** saturates, now in the opposite direction.

These steps repeat after the initial magnetization and create a small lag time between **H** and **M** each time the field flips direction. The small bumps in the field trace of Figure 3.2 are evidence of this delay; when the sample magnetization eventually flips, the driving coil responds inductively and its current increase momentarily slows.

The field trace in Figure 3.2 therefore does not directly reflect the behavior of the sample's magnetization in time. A qualitative version of such a plot is shown in Figure 3.4, from which it is evident that the magnetization is always asymmetric about the point $\mathbf{H} = 0$. Rather, the magnetization is antisymmetric *forward in time* and so we decompose the signal by comparing points one half-cycle apart. This is expressed as

$$M(t) = -M(t + \tau/2), \tag{3.5}$$

where $\tau = 1/f$ is the period. The applied field, with its small disturbance due to the sample's field, actually exhibits this type of symmetry as well. **H** reaches the coercive field at the same time after it crosses through zero, so the dips occur at equal points

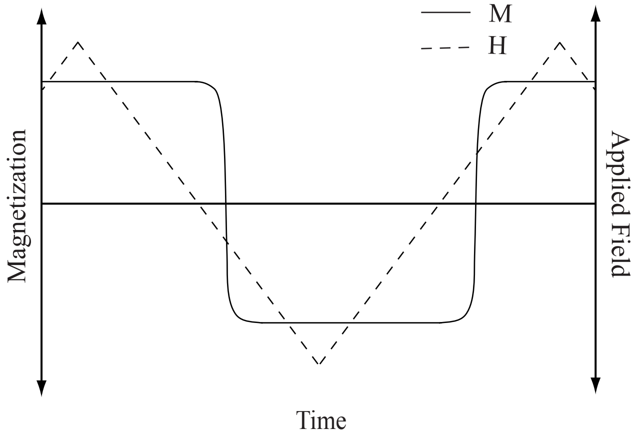

Figure 3.4: Qualitative plot of sample magnetization versus time. Magnetization is the solid curve, and applied field is the dashed curve.

in time after the direction of the field flips. It therefore obeys the same symmetry as in Eq. 3.5, such that $H(t) = -H(t + \tau/2)$.

3.2.2 Decomposition

Based on these symmetries, we decompose the signal from the triangular waveform into contributions that are symmetric and antisymmetric in the magnetization:

$$V_{sym}(t) = \frac{1}{2}\big(V(t) + V(t + \tau/2)\big), \tag{3.6}$$

$$V_{anti}(t) = \frac{1}{2}\big(V(t) - V(t + \tau/2)\big). \tag{3.7}$$

These mathematics provide the basis of many figures and analyses throughout the remainder of this thesis. Applying them to the data in Figure 3.2, we find the symmetric and antisymmetric contributions to the detector signal, as shown in Figure 3.5. The antisymmetric signal comprises a step when $\partial\mathbf{H}/\partial t$ changes abruptly, and an inductive pulse when the sample magnetization flips. The symmetric contribution is what we refer to as the *M-Even effect*; it has been given this name precisely because of these analyses.

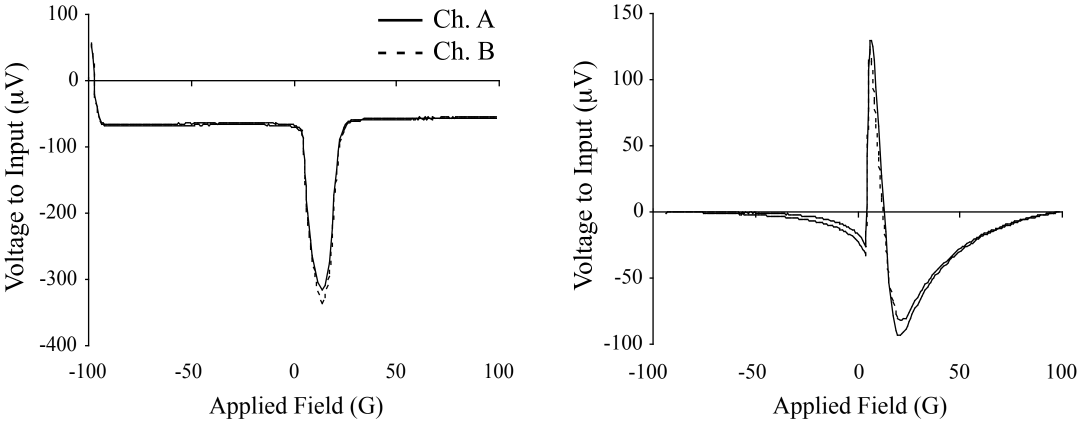

(a) (b)

Figure 3.5: (a) Antisymmetric and (b) symmetric contributions to the detector signal at 127 K. DC offsets have been subtracted.

To understand the M-Even effect has been the purpose of our current work. Its symmetry is puzzling, though recent data and much thought on the parts of Professors Hunter and Gordon have revealed that many things could potentially cause symmetric potentials to appear at our input. Indeed, narrowing the search has been the difficult part. The remainder of this chapter will characterize the M-Even effect further, which should help to place the succeeding chapters in better context. Few of the results are intuitive, but they have all contributed to our current methods, for better or worse.

3.3 Characteristics

3.3.1 Structure

The structure of the M-even signal is not well understood, but it is experimentally reproducible. The signal consistently includes the following features when plotted against the applied field.

- Slight decrease as **H** increases from the negative maximum and approaches zero.
- Sharp rise and drop as the magnetization flips.

- Negative peak after **M** flips, followed by $1/H$ decay in the high-field limit.

The last of these was discussed in the section dealing with data analyses, and is the reason that we use a pulsed waveform during data collection. This wave form allows us to magnetize strongly without overheating the sample. In theory a high field is helpful but not necessary to obtain an accurate EDM reading. With the M-even effect present, high fields are essential. The first two characteristics are presently not understood, but we can make some reasonable assumptions.

When the sample is magnetized, the two halves of the toroid strongly attract each other, just as do two bar magnets placed with opposite poles adjacent. As the applied field increases oppositely and approaches the coercive field, the magnetization decreases along with the force of attraction. Then the field reaches full strength and the attraction is restored. If we associate the signal with some changing behavior in the magnetization, then the M-even effect's structure might be explained.

Varying the maximum value of the applied field changes the shape of the signal and reveals a deeper connection between the effect and the sample magnetization. Figure 3.6 shows several curves of the M-even effect taken at different amplitudes of the applied field. They are vertically offset from each other to emphasize similarity in the shape of the high-field falloff regions. The value of zero is essentially arbitrary, but a particular trace always has the same value at its endpoints. Were **H** to increase further, the M-even signal would decrease and more of the $1/H$ falloff would be visible; displaying the curves this way emphasizes that they would be identical if **H** continued to increase. This is evidence of hysteresis in the M-even effect, a plot of which would look something like Figure 3.7.

The M-even effect produces signals on the order of 100 μV, which are enormous in our experiment. Recall from §2.2.3 that our current sensitivity is on the order of 1 μV, and to reach the world limit of the electron EDM we must distinguish 0.1 nV. This systematic effect therefore produces potential differences two orders of

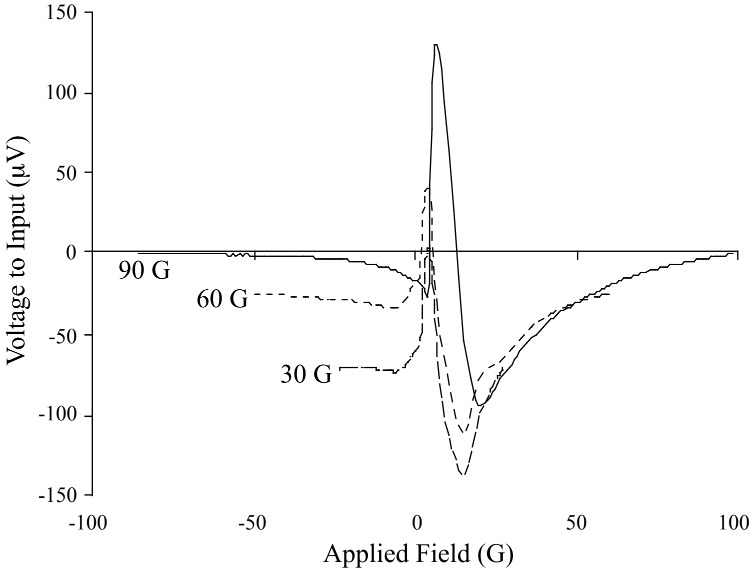

Figure 3.6: M-even effect plots at varied maximum values of the applied field ($T = 127$ K). Frequency has been adjusted for constant $\partial\mathbf{H}/\partial t$.

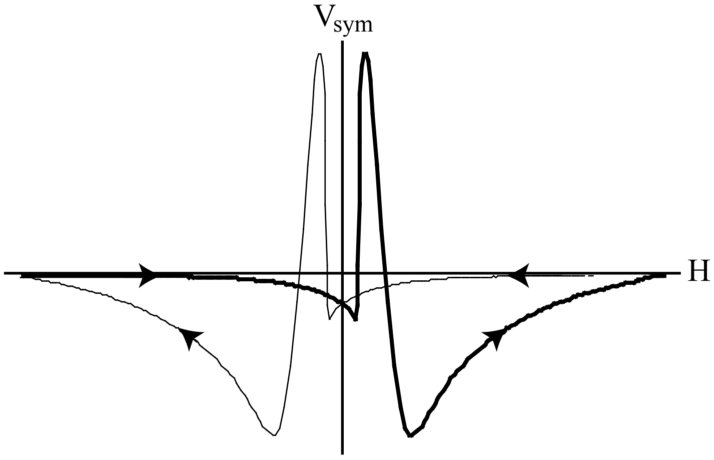

Figure 3.7: Hysteresis loop of the M-Even signal at 127 K.

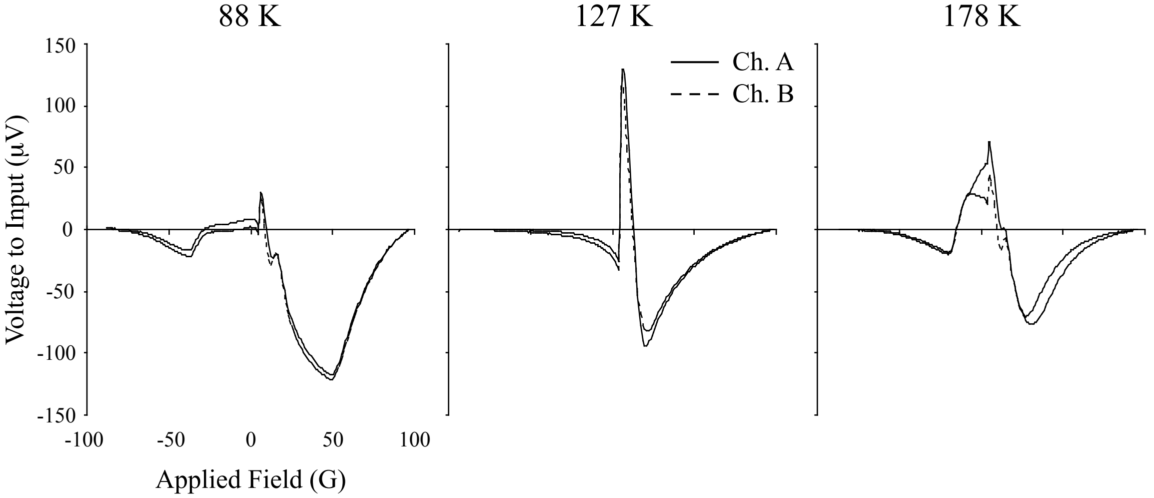

Figure 3.8: M-even effect at the operating temperatures, from summer 2006 ($H_{max} = 100$ G, $f = 1.02$ Hz).

magnitude larger than our current resolution, and *six* orders of magnitude larger than the sensitivity that we hope to achieve. All current research has focused on the M-even effect for this reason.

3.3.2 Temperature Dependence

The structure of the M-even signal changes slightly with temperature, as shown in Figure 3.8. The most interesting change occurs at 178 K, when the signals from the two channels differ just before $\mathbf{H} = 0$. This is disturbing because the channels are well matched in all other measurements. We currently have no explanation for this discrepancy, although it has been observed consistently at 178 K, and never at the other temperatures. The perturbation is due to the GdIG toroid, not the detector, because it tracks with the sample orientation.

3.3.3 Frequency Independence

The M-even effect is largely frequency-independent, which means that regardless of the driving frequency of the applied field, Figure 3.5 looks the same. Such behav-

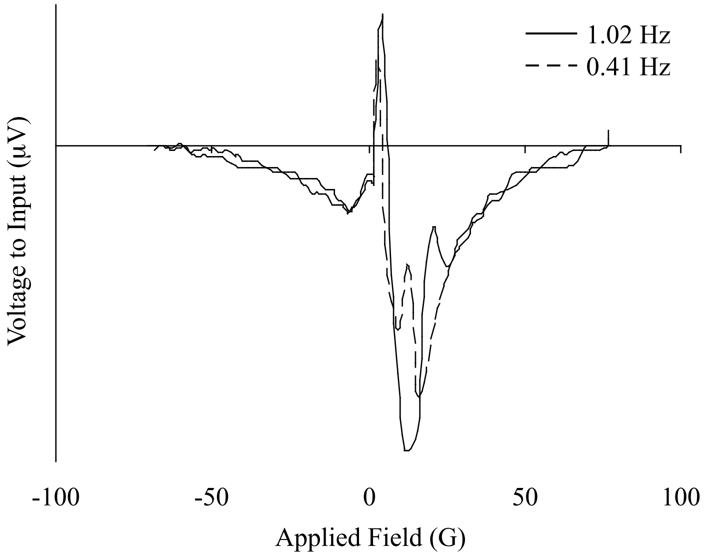

Figure 3.9: M-even signals at varied frequencies, from summer 2006. $H_{max} = 75$ G for both traces.

ior argues against some type of inductive, $\partial\mathbf{H}/\partial t$ effect (which couldn't explain the symmetry anyway). We understand this to be consistent with the interpretation that the M-even signal is magnetization-dependent. Figure 3.9 shows the M-even signal for two different driving frequencies, but with the same maximum field. The plots are essentially identical, apart from some substructure around $H = 25$ G. We observe this occasionally but not predictably, and so it remains unexplained; it is certainly atypical. Figure 3.6 also includes plots of different frequencies, none of which show this substructure.

3.3.4 Compensating Techniques

The most important technique adopted to combat the M-even signal is the pulsed waveform. High field increases the magnetization of the sample and therefore decreases the effect, but strong fields also require large currents. Large currents dissipate power in the form of heat, which becomes unacceptable as temperature regulation is important to our data collection. The problem is worst at 88 K, where the system temperature is just 11 K above that of the cold reservoir, liquid nitrogen ($T_{BP} \approx 77$ K).

We compromise by applying the strongest field possible with current[3] equipment, but we turn it off as soon as the sample is magnetized. The prices we pay are large inductive pulses, demagnetization due to flux matching, and the 23% overall loss, all of which are discussed in §2.5.2. Lowering the frequency of field pulses also helps, by decreasing the duty cycle of the heating. For this reason, much of the data from the summer of 2006 was collected at a frequency of 1.02 Hz instead of the usual 2.3 Hz.

3.4 Remounting the Sample

For many years, the two channels of the sample had produced inexplicably asymmetric signals. Channel A responded much more to microphonic excitations, and the magnitudes of its inductive pulses were consistently only 68% of those of channel B [2, §7.3]. For publication [1], the data from channel A were corrected by a factor of 1.47 to correct for this difference, but the asymmetry was still puzzling. Additionally, the 1.8 Gd half of the toroid was chipped before arriving at Amherst, breaking the symmetry of the toroid. The consequences of this were unknown.

To correct for both of these defects, the mounted, epoxied toroid was deconstructed in the spring of 2006. We found that the electrode wire of channel A had become significantly detached from the electrode plate, and the exposed surfaces quite oxidized; physical stability was certainly compromised. The sample was returned to the manufacturer, Pacific Ceramics, to be ground down below the level of the chip, reducing the height by 3/16". It was then heated to burn off the epoxy that was keeping the two halves together, giving us a fresh start. The thickness of the electrode plates was doubled from 0.001" to 0.002", and the wires were directly soldered to

---

[3] No pun intended.

the plates. The two halves of the toroid were then reattached with Epo-Tek EE149-2 silver-doped epoxy, which is different from the previously used brand. (This changed simply because the previous type was no longer available.)

After remounting the sample and collecting new data, we have found two primary changes. First, the signals from the two channels are well enough matched that no correction is required. Secondly, the M-even signal has decreased on both channels by a factor of approximately six. While the former correction is pleasing, it is the latter is the most relevant to the current work.

3.5 Summary, Interlude

The theoretical background for this thesis is now complete. The mathematics of discrete symmetries have been introduced, the nature of solid state EDM experiments explained, and the mathematics of our experiment derived in full. With the aid of appendix C, we hope that the reader has a good sense of how and why our apparatus is constructed. Now that the M-Even effect has been characterized to the most accurate level yet reported, we turn to a description of recent experiments to examine it further.

The next chapter outlines our early experimental methods and results, in an effort to motive the work presented in chapter 5. It begins with a description of the model system designed to facilitate these tests and then presents the data in roughly chronological order.

Chapter 4

Early Results

This chapter describes the first sets of experiments conducted to examine the M-even effect outside the EDM apparatus. The essential methods and results are discussed, but the details are located in appendix D. As mentioned in the previous chapter, we observed a factor of six decrease in the size of the effect after the sample was ground down and reassembled with new epoxy, electrodes, and electrode wires. The volume of the sample was changed by only 10% but the M-even signal decreased six fold, indicating that the effect is not due to the bulk, magnetic properties of GdIG. The epoxy was changed to a different brand, and the electrodes were differently constructed, so we next considered possible surface interactions at the electrode.

We first describe the model system constructed to examine the M-Even effect, and then some preliminary results. Few of these experiments yielded intuitive results, but some questions regarding the nature of the M-even effect begin to be addressed. Conclusions are drawn at the end of the chapter, where the results have been summarized.

4.1 Model System

The electrodes of the GdIG toroid are practically inaccessible because the Faraday cage surrounding the sample is encased by a field coil. Accessing the toroid requires cutting off and eventually rewinding this coil, which takes two people the better part of a week to complete. A more accessible model system therefore had to be built, and we chose a solenoidal coil and cylindrical samples. This cylindrical geometry introduces demagnetizing fields; however, it is easy to assemble and to alter.

4.1.1 Structure

Certain features of the new system are similar to those of the larger apparatus: a sample is mounted within a strong magnetic field and has an electrode somehow attached to its surface. This electrode connects to the gate of a high input impedance amplifier that isolates the electrode and prevents loading by the oscilloscope. Both the sample and the detector are kept within a Faraday cage to minimize noise.

The model system comprises a set of two solenoidal coils in parallel, one inserted into the other. Figure 4.1 shows the entire system in cross-section. The outer coil was constructed by Jared Hertzberg '98E for a different experiment. It is 10" tall and has extra windings for 1.5" at the bottom and top to diminish end effects; the three regions may be connected in any combination.

The inner coil was made by Dan Krause, Jr. and Benjamin Heidenreich in the winter of 2006. It is 8.75" tall and has the detector circuit mounted above it, surrounded by a 2" tall, accessible Faraday cage. The top of the cage is a brass plate with BNC inputs for positive and negative voltage supplies, ground, and output. This entire unit is inserted vertically into the outer coil and rests on a brass plate that is screwed into the bottom of the latter (completing the Faraday cage). The inner region of the inner coil therefore provides space to mount a sample. Electrode wires

Coil	Resistance (Ω)	Field Strength (G/A)
Top end	0.3	
Bottom end	3.5	90
Outer main	8.2	
Inner coil	9.0	140
Combination	8.1	130

Table 4.1: Resistance and field strength of each coil in the model system. Field strength is measured at the center of each coil, and is given for the outer coil with all three sections in series. The combination is the circuit shown in Figure 4.2.

extend vertically through the detector circuit board, where they are soldered to the input of the amplifier.

Mounting samples is challenging, but our system generally includes braces that are constructed to hold samples and center them vertically within the inner coil. The designs of various braces will be discussed in §4.2.

4.1.2 Magnetic Field

The inner coil is connected in parallel with the main body of the outer coil, and this combination is in series with the end coils. A circuit diagram for this combination is given in Figure 4.2. We connect them in this way to reduce the overall resistance while maintaining adequate current through the two main coils. (For example, virtually no current would flow through the inner coil were it connected in parallel with an end coil.) The resistance and field strength of each coil is given in Table 4.1, as measured directly with a Gaussmeter and an Ohmmeter.[1]

A linear amplifier, originally constructed by Phil Grant for the EDM apparatus, drives the solenoidal coils. It outputs up to ±6 A of current, which is adequate for the model system, although we now require ±10 A in the toroidal coil. The amplifier has two output terminals, positive and negative relative to ground, each in series with a

---

[1] The resistance of the top end coil is disturbingly low; this may be due to internal shorting. The field at the top of the outer coil is observed to be lower than at the bottom, supporting this conclusion.

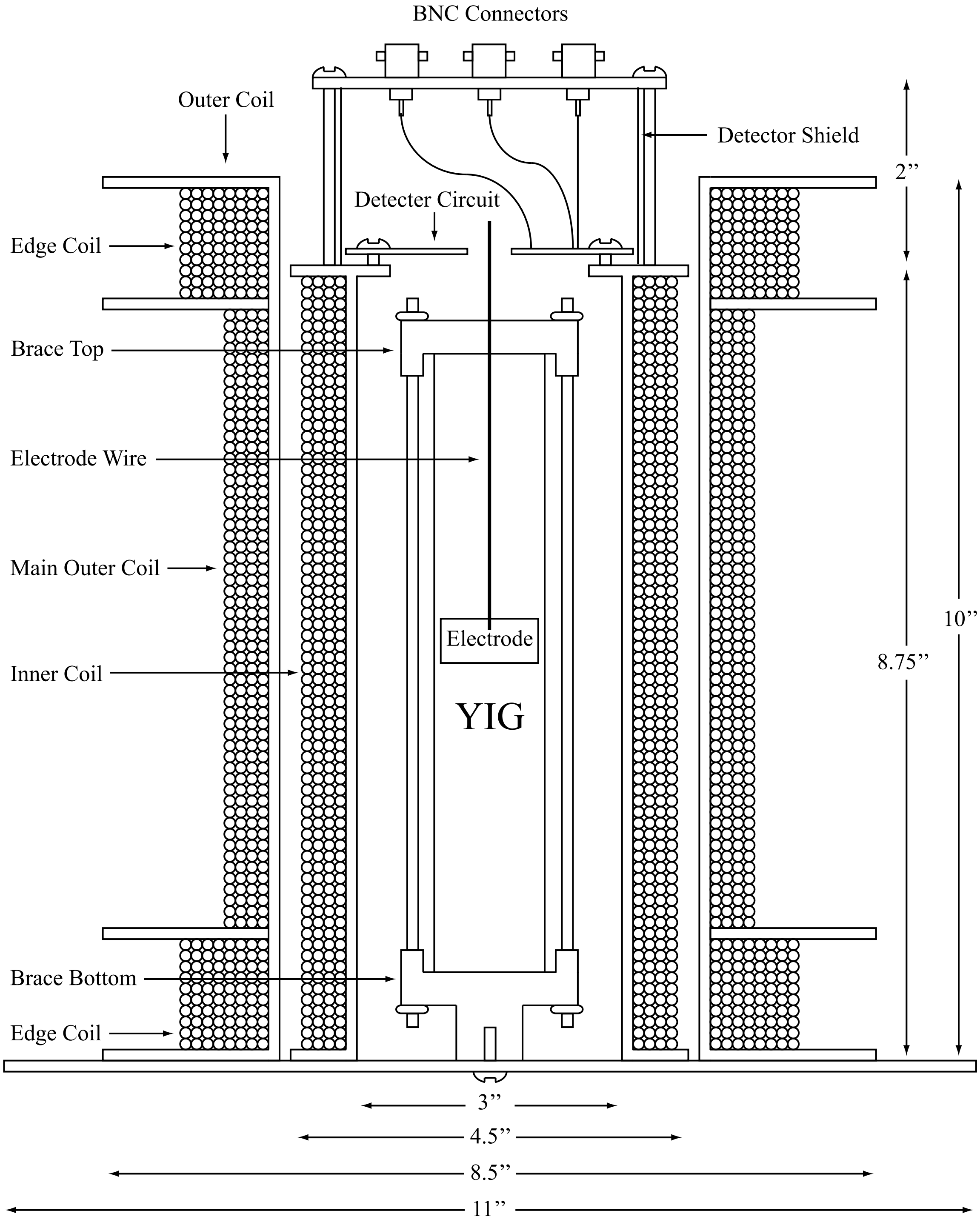

Figure 4.1: Cross-section of the model system; dimensions are largely to scale.

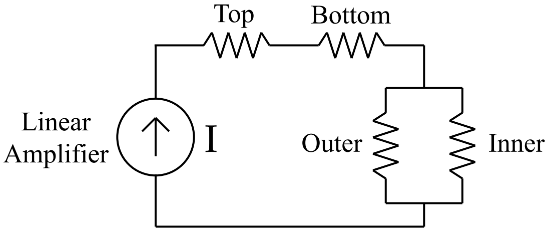

Figure 4.2: Circuit diagram for the field coils.

0.1 Ω resistor. We measure the voltage across this resistor with an *isolation amplifier* so that neither side is placed at ground potential, which would draw significant current and potentially damage circuitry. This amplifier has unity gain.

The linear amplifier is controlled by an Agilent function generator that can be arbitrarily programmed, though we typically use a triangular waveform. The driving amplitude is 11 V peak-to-peak in nearly all experiments, which results in ±4 A of current. By the conversions in Table 4.1, this gives an applied field of ±520 G at the center of the solenoids, and an average of roughly ±500 G over the entire volume.

4.1.3 Detector

The detector circuit used in the model system, shown in Figure 4.3a, is much simpler than that found in the main apparatus, Figure B.4. In fact, the entire amplifier is contained within a single IC, known as an INA116, manufactured by Burr-Brown Inc. It comprises three interconnected op-amps that function as an instrumentation amplifier with a single external resistor to adjust the gain [36]. We set the gain at 10 with a 5.6 kΩ resistor. The amplifier has extremely high input impedance, which we approximate to be on the order of 10^{16} Ω, and we decrease this by connecting a 10^{11} Ω resistor from the gate to ground. This is necessary so that the RC time of the circuit is much longer than the data collection time, but short enough that detector offset voltages practically decay.

The circuit is printed on a single G10 board, as shown in Figure 4.3b, with resistors

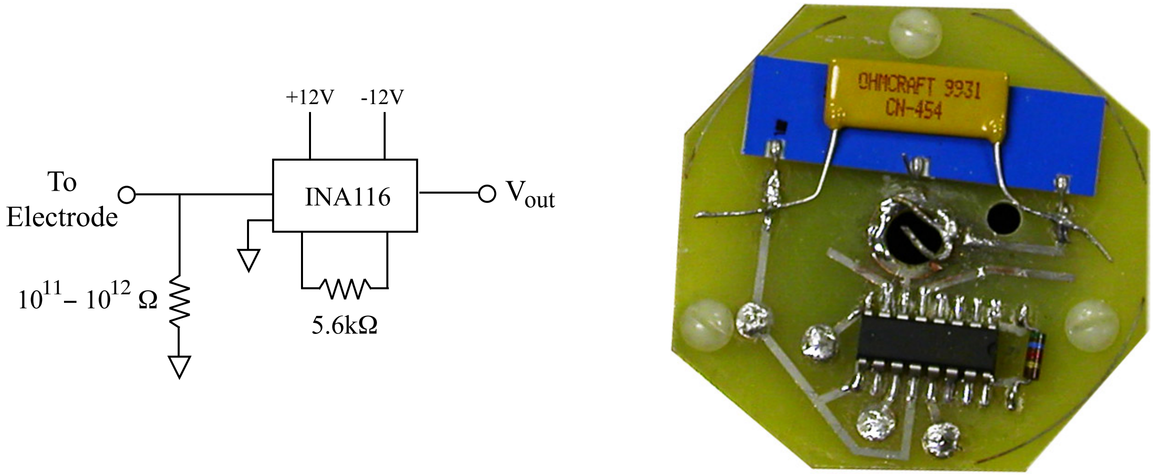

(a) (b)

Figure 4.3: The detector circuit of the model system: (a) circuit diagram, and (b) printed board with 10^{11} Ω and 10^{12} Ω resistors in parallel to ground.

mounted flat to lessen microphonic noise. The circuit usually takes several minutes to "settle" after being switched on, which is to say that DC offsets appear on the output and decay slowly to zero. This is reassuring because it indicates extremely high resistance to ground at the input, but it also inhibits our resolution. Typical offsets are several hundred millivolts in size.

4.1.4 Mounting Samples

Samples can be positioned within the inner coil in any number of ways, but they all must somehow be stabilized and vertically centered. The bottom plate of the inner coil provides an anchor point for any type of mechanical brace; a hole in the center allows a screw to extend into the space and hold whatever mounting system has been constructed.

Most braces discussed in this thesis follow the same principles of design. Our samples are generally long and thin, so we brace them at the top and bottom with "caps" connected by thin rods. The rods are 1/8", threaded brass with nuts on the top and bottom that are tightened to provide overall pressure on the sample. The bottom caps can be elevated to any height by placing spacers beneath them. There are many examples of this throughout the next chapters; later generations are noticeably prettier. With a description of the model system behind us, we now consider the first samples used and the mounts constructed to hold them.

4.2 Samples and Mounts

Ben Heidenreich began tests with the model system using a long, hollow cylinder of yttrium iron garnet (YIG). He observed a symmetric signal from an electrode attached to the surface of this sample [2, §7.9]. We believe that this is entirely analogous to the M-Even effect. If this is true, then the effect is not coupled to the EDM signal because YIG has essentially no sensitivity to the electron EDM (yttrium has no net spin, and iron and oxygen contribute only negligibly to the enhancement). We therefore hope to eliminate the effect without compromising our sensitivity. These experiments continued with various YIG samples for the next several months, but the data were largely irreproducible.

We continued from these preliminary results by experimenting with several new samples. Three are discussed in this chapter, along with preliminary results. We hope that this will outline the many difficulties encountered and the efforts made to improve the reproducibility of our data.

4.2.1 YIG Cylinder

The first sample that we purchased is a 7" long cylinder of YIG manufactured by Pacific Ceramics, the same company that fabricated our GdIG toroid. It has a 1.2" diameter and is therefore somewhat thin relative to its length, which diminishes demagnetizing effects. The mount that we constructed has plastic end caps to ensure high resistance to ground, and the aforementioned brass rods to apply tension. These

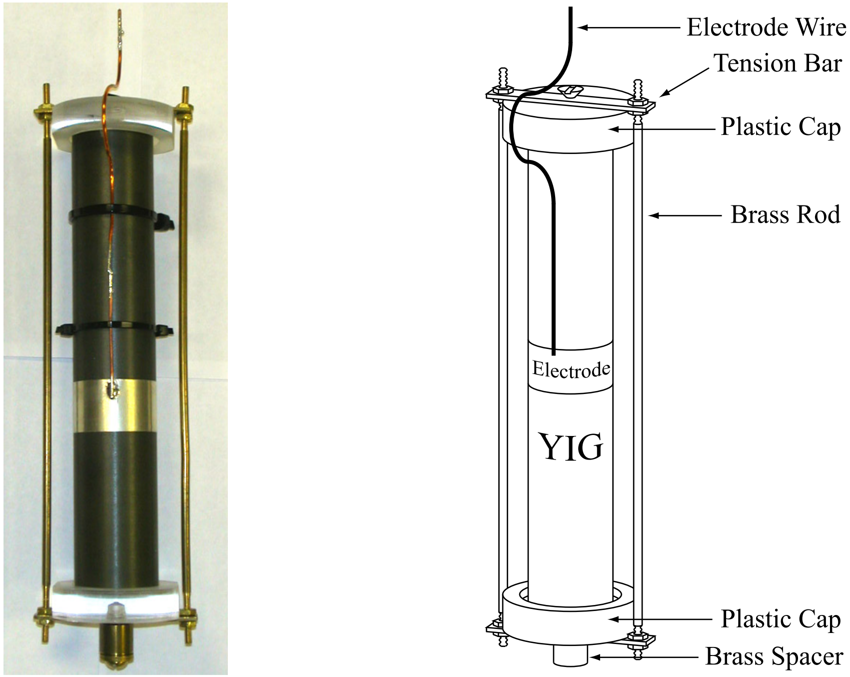

Figure 4.4: The brace built to hold the long, YIG cylinder. Dimensions are to scale.

rods attach to brass plates that grip the plastic end caps. The brass plates in turn connect to a metal spacer, which is in contact with the bottom plate; this ensures not only that all metal on the brace is grounded, but also that the YIG touches only plastic. Figure 4.4 shows both a photograph and a schematic diagram of the brace.

Electrodes are attached to the side of the sample, usually in the middle because this is the region of strongest field. A wire attaches to the electrode and extends vertically (bending around the top) to reach the detector above.

4.2.2 YIG Toroids

To mimic better the interface of the electrodes and the sample in the GdIG toroid, we next chose to "sandwich" electrodes between two samples of YIG. The lab possesses two suitable samples, which are small, irregular cylinders with holes drilled down their centers. They each have at least one face polished flat and perpendicular to its axis. We refer to these as *toroids*, though their geometry is essentially cylindrical.

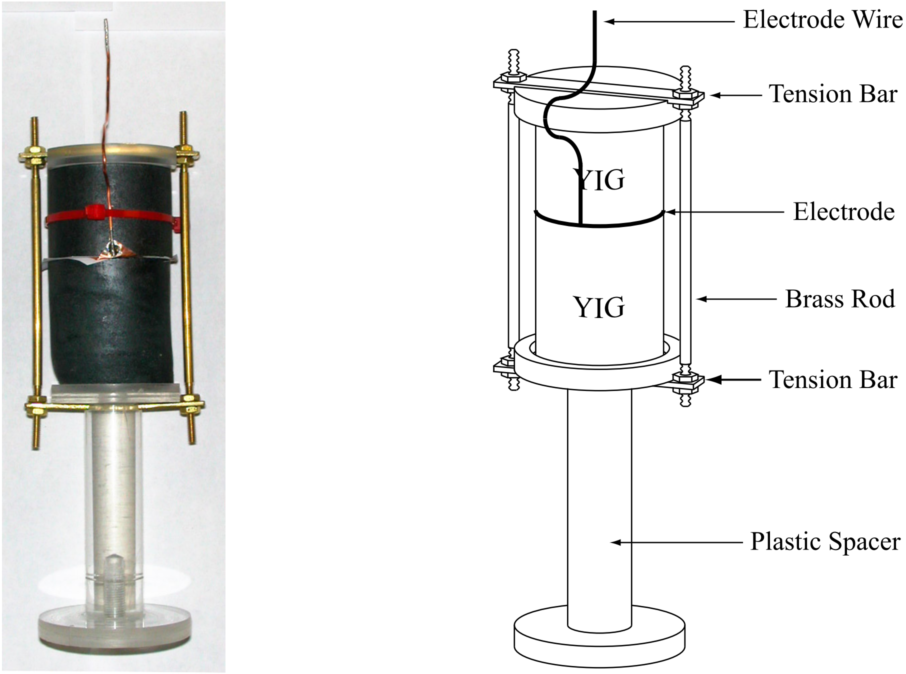

Figure 4.5: The brace built to hold the small, YIG toroids. Dimensions are to scale.

One toroid is 1.75” tall, and the other 1.25”, for a total length of 3”; both have 1.5” diameters. The effective length of the sample is therefore only half that of the longer cylinder, and so demagnetizing effects are worse. Nevertheless, symmetric signals are observed and the samples adequately magnetize in our applied field.[2]

The brace constructed to hold these samples follows the principles of the previous generation. It is almost entirely plastic, and has brass tensioning bars on both the top and bottom. Brass rods provide tension, and because the bars at each end are thin, they flex to provide variable force up to approximately 400 lbs. A photograph and a schematic diagram of this brace are shown in Figure 4.5. Circular electrodes are constructed to match the cross-sectional dimensions of the toroids.

This brace suffers from being constructed almost entirely of plastic. It provides extremely high resistance from the electrode to ground, but we believe that static charge also builds up on the plastic and creates undesirable fields near the electrode.

---

[2] This conclusion is based on data regarding the force of attraction between the samples. These results may be found in §D.5.

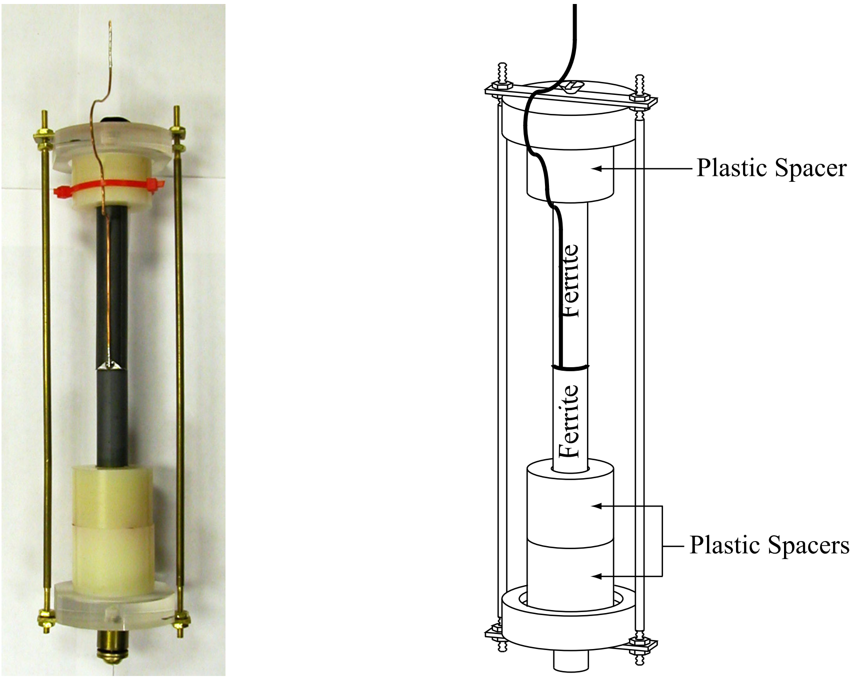

Figure 4.6: The initial brace to hold the ferrites. It is simply the long, YIG cylinder brace with plastic spacers. Dimensions are to scale.

4.2.3 Ni-Zn Ferrites

In order to obtain a comparison with YIG and to gain practice in making permanent bonds, we also carried out experiments with Nickel-Zinc ferrite samples. These ferrites are inexpensive and highly magnetic, but, unfortunately, have much lower resistivities than YIG (approximately $10^8\ \Omega$ versus $10^{15}\ \Omega$ for our dimensions). This reduces the RC time of the circuit.

The symmetric signals that we observe with the YIG samples do indeed appear with the ferrites, although they are smaller and often distorted. Only a few results from these samples are presented in this chapter; the majority of the tests conducted with them used a different brace and are discussed in chapter 5.

4.3 Preliminary Results

All data presented in this chapter were taken using a 1.1 Hz, triangular waveform giving a maximum applied field of ±500 G within the solenoids. The signals are decomposed via the methods of §3.2.2, and it is the symmetric contributions that are shown here. (The antisymmetric contributions tend to be extremely small, at least relative to the symmetric ones.) The symmetric signals are largely symmetric about the point of zero applied field because demagnetizing fields limit hysteresis. As a control, we measured the output signal when the samples were present but the electrode wires removed. No symmetric signals were observed.

All traces are additively adjusted so that they are zero-valued at the point of maximum applied field strength. We do so because our detector experiences time-varying DC offsets and so only potential differences are interesting. The measured potential asymmetry in the GdIG sample has its minimum in the high-field limit, and so we adopt this convention.

4.3.1 Adhesives

We first tested the model system by mounting the long, YIG cylinder and wrapping conductive tape on its surface as an electrode. This tape is approximately 0.001" thick and has acrylic adhesive on at least one side; the contact resistance of the adhesive is on the order of 0.01 Ω, according to manufacturer specifications. The electrodes were vertically centered and approximately half the height of the sample. Each comprised five strips of conductive tape partially overlapping to be electrically continuous.

Three different types of tape were used separately: copper, aluminum, and tin-plated copper. Each produced a symmetric potential on the electrode as the sample was magnetized; these results are shown in Figure 4.7a. We note particularly that the signal from the tin-plated copper electrode has an opposite sign to those from

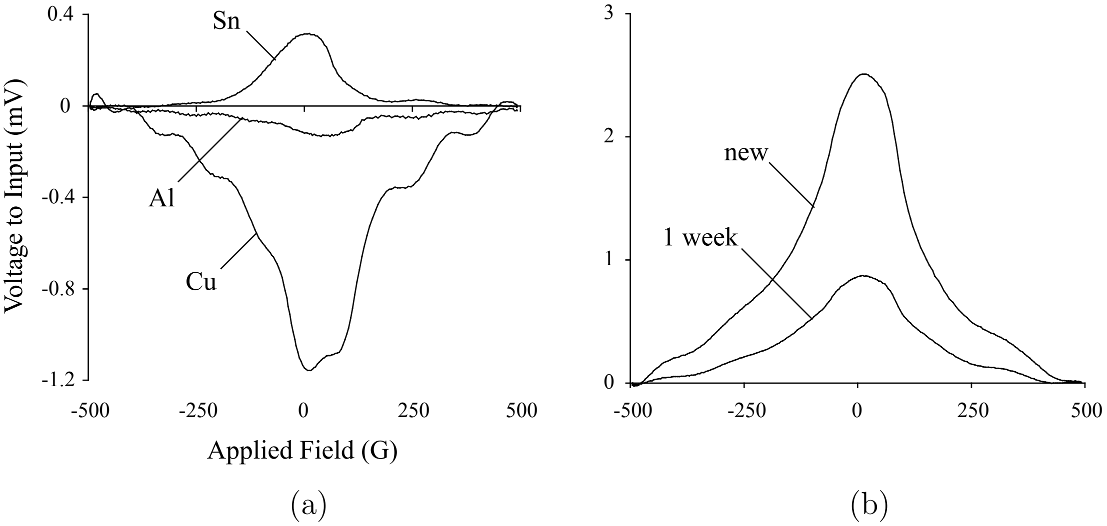

Figure 4.7: Symmetric signals from conductive tape electrodes on the long, YIG cylinder. (a) Different metals, (b) Aging of the copper electrode.

both copper and aluminum, although we observe inconsistent sign changes when experimenting with conductive tape. Copper reproducibly exhibits the largest signal, and aluminum the smallest. All signals, however, are approximately an order of magnitude larger than the M-even effect in the EDM apparatus (Figure 3.5b), which is approximately 100 μV at its peak.

Once we observed symmetric signals, we began to vary the properties of the electrodes. We note that the symmetric signals are largely independent of the size and position of the electrode, as well as the frequency of the applied field. The signal size does depend on the amplitude of the applied field.

Unfortunately, the signals from conductive tape electrodes decrease over time, as shown in Figure 4.7b. The adhesive bonded more tightly to the YIG over time, and we speculate that this may have limited the motion of the electrode. Regardless, this caused significant irreproducibility in our results, and prompted us to consider different adhesives. We tested one such material, silver paint, before deciding to abandon adhesives temporarily.

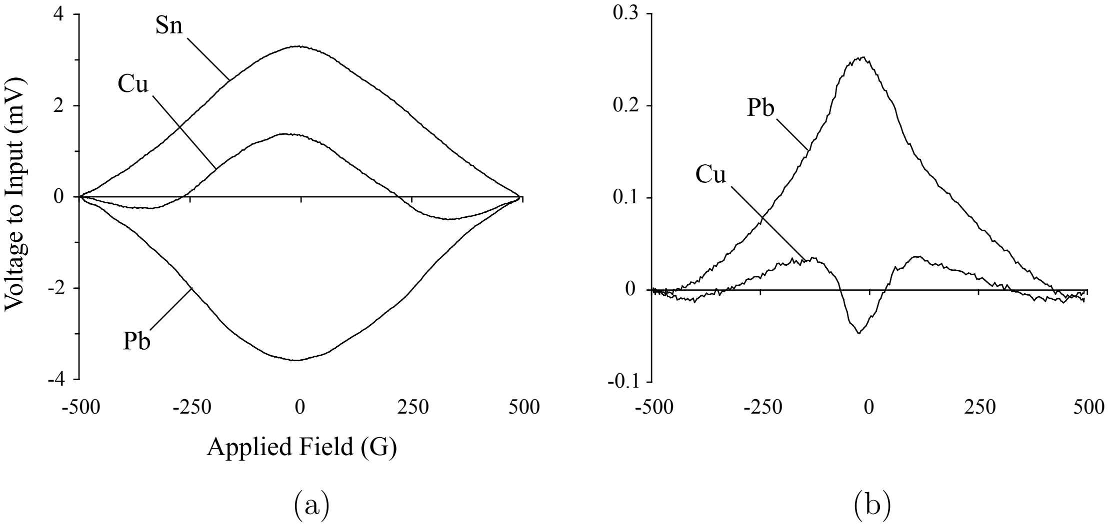

(a) (b)

Figure 4.8: Symmetric signals from metal electrodes without adhesive. (a) YIG toroids, (b) Ferrites.

4.3.2 Interfaces

With the YIG toroids, we are able to compress and stabilize electrodes between the samples without any adhesive. Based on the observation that tin-plated copper exhibits a signal of opposite sign to the others, we decided to test a variety of different metal electrodes. The results, a selection of which are shown in Figure 4.8a, indicate that the sign difference between tin and copper is not consistent.

We note that the sizes of the signals are largely independent of the size and thickness of the electrode, if we disregard apparent differences in sign. The signals do not noticeably change over time, which is an improvement over the previous methods. At this point we also obtained the Nickel-Zinc ferrites and tested both copper and lead electrodes between them. These results are shown in Figure 4.8b; the sign of the lead signal is inconsistent between the YIG and ferrite tests, and copper shows interesting structure.

In these early experiments with the YIG and ferrite samples, we occasionally anchored the electrode wire to the side of the samples with plastic zip-ties, to reduce vibrational noise. Unfortunately, this tended to alter the signal sign, shape, and size

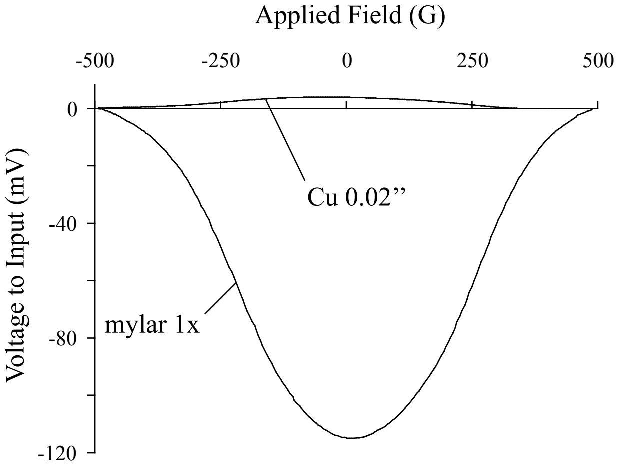

Figure 4.9: Symmetric signals from 0.02” copper electrodes, with and without one sheet of 0.001” mylar above and below the electrode. The signal size increases by two orders of magnitude.

upredictably. The data presented in Figure 4.8 were taken later, without zip ties, for consistency.

4.3.3 Dielectrics

The magnitudes of the symmetric signals significantly increase when we insert thin, dielectric material between the electrode and the YIG samples. We first tried paper, simply to see if a signal would be observed at all, and then 0.001” thick mylar sheets. When mylar is inserted with a copper electrode, the symmetric signal changes sign and increases by two orders of magnitude, as shown in Figure 4.9.

Preliminary models of the M-even effect involved unknown surface interactions between the YIG and the electrode, but none of these could explain the observed signal increase from mylar. However, it is not clear from these tests whether or not the large signals are directly related to those from the metal electrodes. Perhaps, for example, the large signal is the sum of two terms, one arising from a surface interaction with the YIG, and another due to the dielectric. Further experiments address this issue in greater detail, and these are discussed in chapter 5. At this

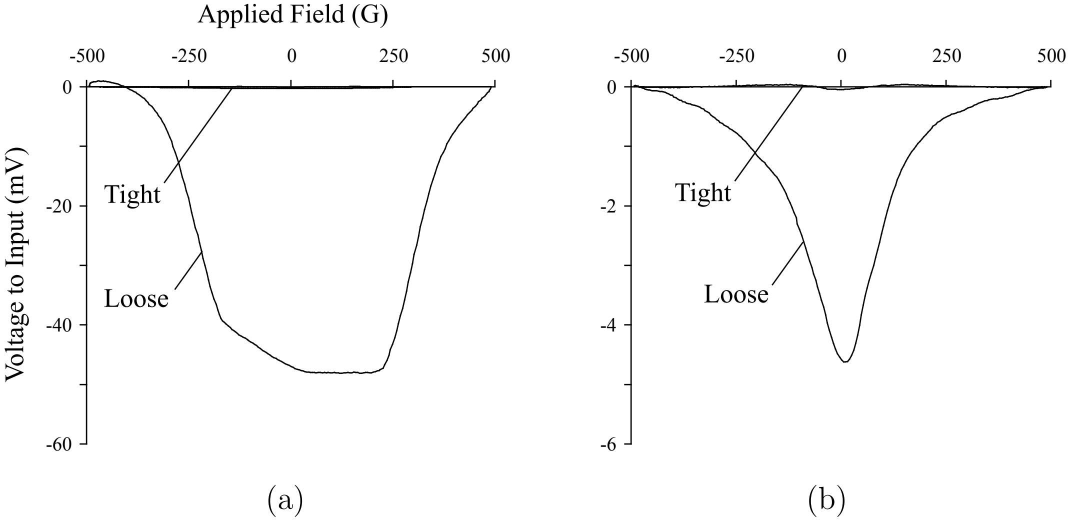

Figure 4.10: Symmetric signals from 0.02” copper electrodes under variable brace pressure. (a) YIG toroids, (b) Ferrites.

point, the signals from the dielectric tests were reproducibly large (within factors of two or so) but did exhibit some inexplicable sign differences.

4.3.4 Pressure Variation

We observe significant changes to the symmetric signals when we variy the pressure applied to the samples. The braces are designed simply to provide physical stability without concern for quantitatively measurable pressure, but we note that the sizes of the signals increase dramatically when the braces are loosened. Data from these tests with both the YIG toroids and the ferrites are shown in Figure 4.10.

In both cases the signals become large and negative, increasing by three orders of magnitude in YIG and two orders of magnitude in the ferrites. This variation is entirely reproducible and we observe it with every assembly in which an electrode is compressed between two surfaces; no comparable tests were performed with the long, YIG cylinder. To examine the effect further, we altered the assembly to apply time-varying pressure to the top of the toroid brace, as described fully in §D.2.6. We note that pressure variations yield extremely large signals, and that this requires neither

YIG nor an applied, magnetic field to be observed.

4.4 Conclusions

Several significant trends emerge from these results. First and foremost, large symmetric signals are observed when electrodes are coupled to the surfaces of YIG samples that are periodically magnetized. If these signals correspond to the M-even effect, then our model system successfully reproduces the systematic effect of interest, and in a highly accessible environment. Second, the structure of the effect depends on how the electrodes are coupled to the surface. Both dielectric materials and adhesives dramatically affect the signals.

Perhaps most importantly, the methods of mounting the samples affect the observed signals. Varying the brace pressure can change the amplitude of the signal by over three orders of magnitude. When we tighten the toroid brace as much as possible without breaking it, the signals generally decrease to the order of 0.1 mV peak-to-peak, which is an order of magnitude less than those shown in Figure 4.8. This signal size is comparable to that of the M-Even effect.

Additionally, these symmetric signals are observed not only with YIG samples, but also with Nickel-Zinc ferrites. This is reassuring because it implies that the effect is not specific to iron garnets, and therefore we need not seek another material for the EDM experiment. Instead, our method of assembly may require refinement.

Unfortunately, these experiments yield unacceptably irreproducible results for the smaller signals. We desire a system by which we may examine precise changes in the size and structure of the M-even effect, and the data from variable pressure tests evidence that these methods of mounting samples are insufficient. Additionally, the system is extremely sensitive to microphonic noise when these plastic braces are used. To limit the accumulation of static charge, we now mount samples in purely metal braces. The results of these tests are described in the next chapter.

Chapter 5

Experimental Results

This chapter describes the final experimental results from the current work. The data are significantly more reproducible than those described in the previous chapter. The observed signals are largely free of sign fluctuations, and their sizes and structures are essentially consistent. We describe two sets of samples, short YIG cylinders and Ni-Zn ferrites, and the experiments performed with them. Many experiments from chapter 4 have been repeated, and some interesting trends have emerged. Additional experiments with these samples are described in appendix D.

5.1 Samples and Mounts

The primary samples of interest in this chapter are short cylinders of YIG, 2" tall with 1.2" diameters. They are held by a brass brace to prevent static charge from accumulating near the electrode.[1] The brace has four brass rods to apply tension, and the tension bars are thickened to 1/4" to reduce bending. This limits the variability of the force, but allows it to reach up to 1,000 lbs.[2] A photograph and schematic diagram of the brace are shown in Figure 5.1.

---

[1] Unfortunately, YIG is an excellent insulator, but we couldn't really do away with that.

[2] The methods for determining this are described in §D.5.

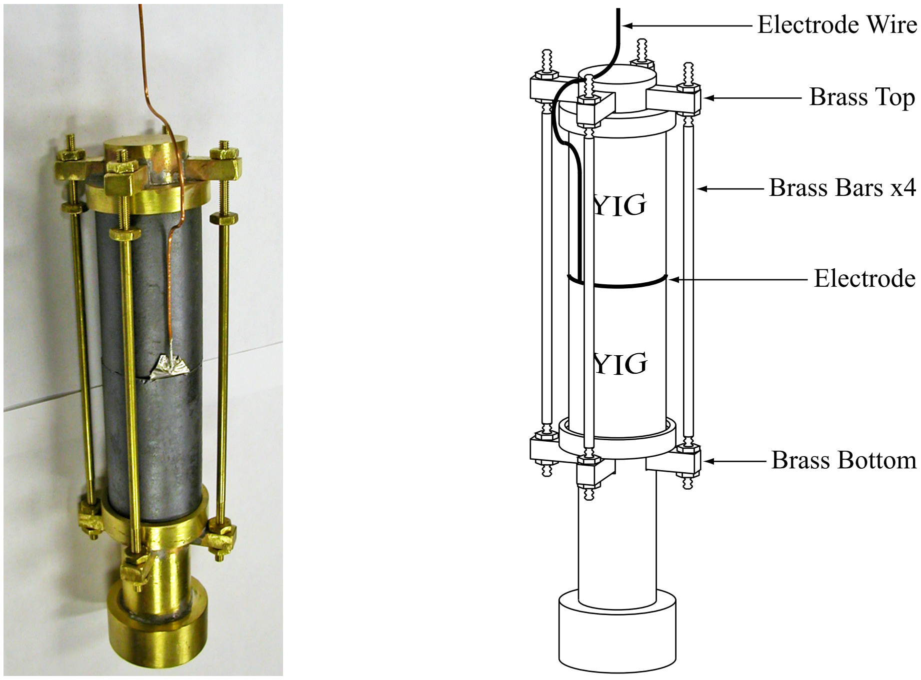

Figure 5.1: The metal brace built to hold the YIG cylinders. Dimensions are to scale.

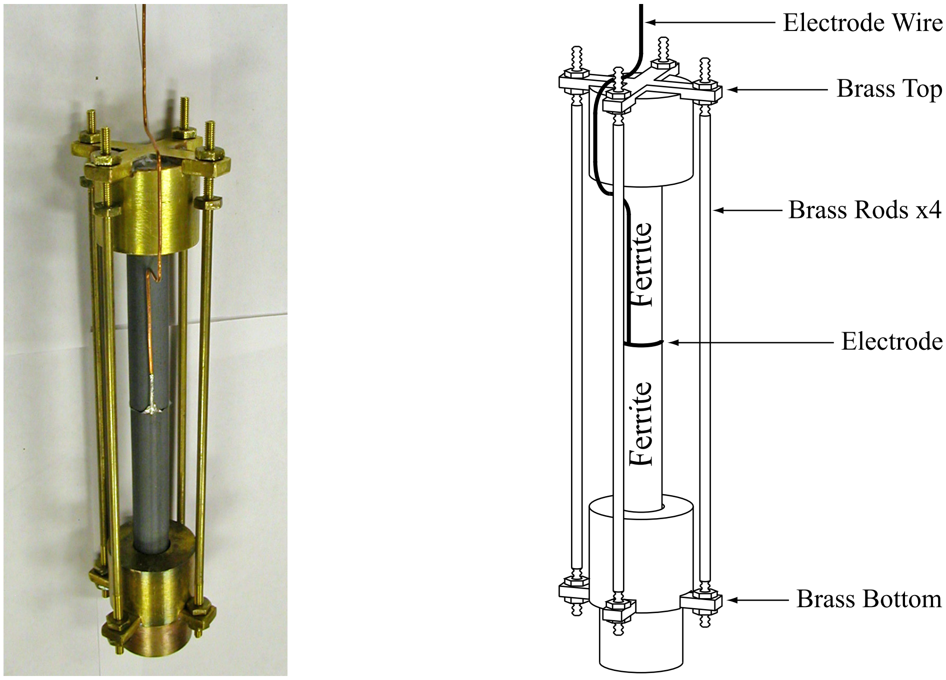

Figure 5.2: The metal brace built to hold the Ni-Zn ferrites. Dimensions are to scale.

Material	Thickness (0.001”)
Aluminum	1
Brass	2
Copper	2, 20
Gold	1
Indium	5
Lead	8
Tin	2
Zinc	4

Table 5.1: Metals used as electrodes.

The YIG brace also serves to compress samples during epoxy and indium bonding. It is 2.5” at its maximum diameter, and therefore fits into the 2.75” diameter, cylindrical oven available in our lab. These experiments are described in §5.3.

For comparison, we pursued experiments with the Nickel-Zinc ferrites in parallel with those of the YIG cylinders. The samples are 3” long with 1/2” diameters, and are similarly held by a purely conductive brace. The end caps have 3/4” deep holes in them to hold the samples and limit their relative motion. A photograph and schematic diagram of the brace are shown in Figure 5.2.

5.2 Metal Electrodes

As a first test with each brace, we compressed eight different metal electrodes between the samples, without any adhesive. The metals and their thicknesses are listed in Table 5.1, and the symmetric contributions to their signals are shown in Figure 5.3. These results should be compared to those from the YIG toroids, described in the previous chapter and shown in Figures 4.8 and D.7.

In both cases, the signals from indium, tin, and zinc electrodes are similar to each other, though the results are different for each sample. These electrodes yield positive signals from the YIG toroids, and here they yield largely negative signals with positive peaks to either side of zero applied field. Additionally, lead electrodes

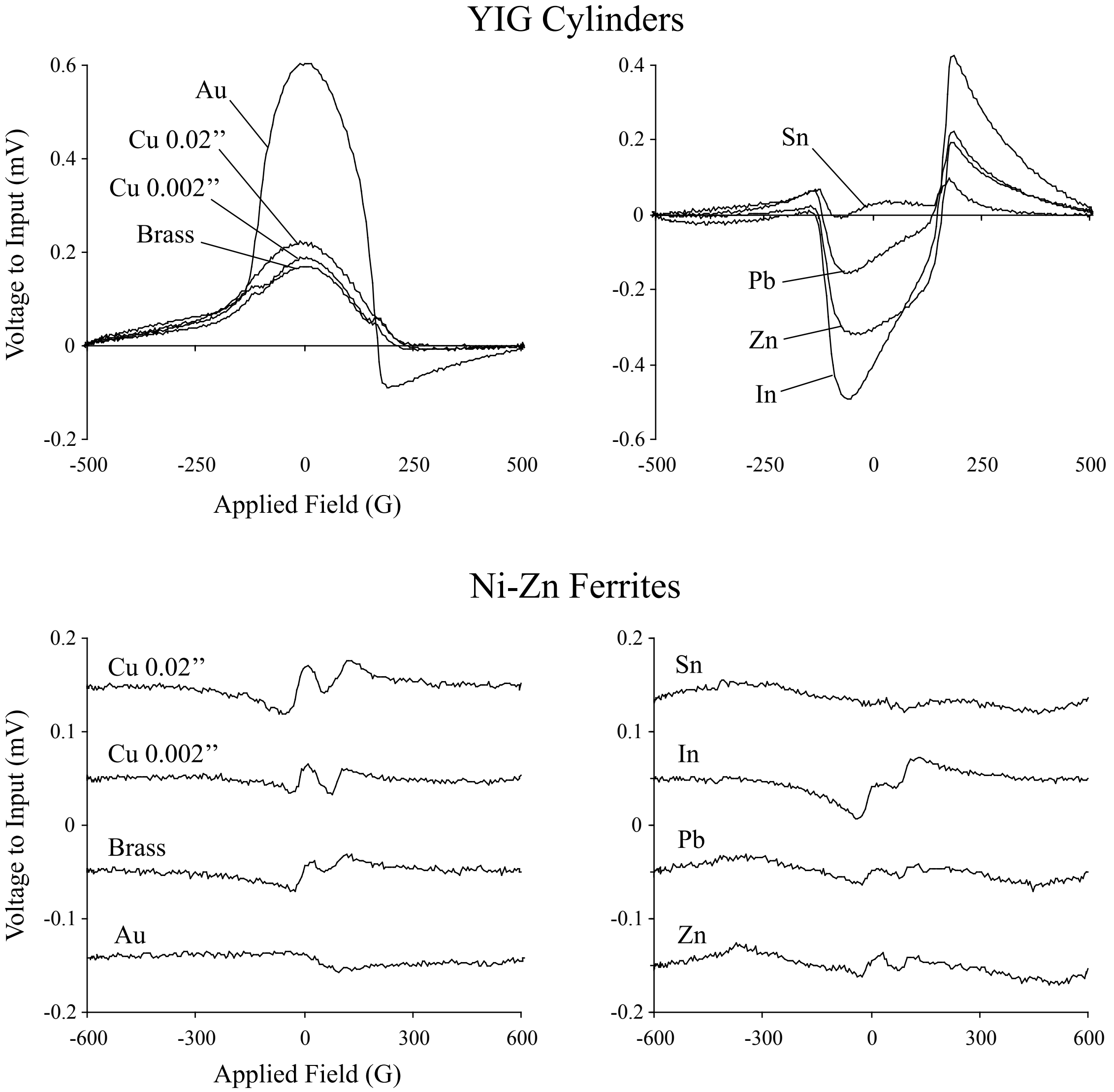

Figure 5.3: Symmetric signals from different metals electrodes between the YIG cylinders and ferrites; both braces were fully tightened. The ferrite signals are vertically displaced for clarity.

now give responses similar to those of the aforementioned metals.

Copper and brass electrodes, which are generally harder, produce fairly smooth, positive signals. Thinner electrodes show slight dips to either side of the point of zero applied field, reminiscent of those in the signals from the softer electrodes. Gold is an interesting exception, and yields the largest signal by far. Preliminary analyses of the YIG results are given in §6.2. The signals from the ferrites all show interesting structure, but we are currently unable to interpret their similarities and differences.

5.3 Epoxy and Indium Bonding

In addition to the various metal electrode tests, we also bonded the samples together using silver epoxy and indium, both with 0.002" copper electrodes. The epoxy is Epo-Tek EE149-2, which is same as in the GdIG toroid. At the time of writing, the YIG samples are still epoxied together after a month, but the ferrites have fallen apart.

To indium bond the samples, Dan Krause Jr. first vacuum deposited a thin layer of indium on the bonding surfaces of the samples, as well as on the copper electrodes to be used. We then assembled the braces as usual, with the electrode between the two samples, but inserted a sheet of polished, 0.005" indium metal above and below the electrode. The entire assembly was then compressed in the brace and heated to 250°C. Both the ferrite and YIG samples remain bonded, though we have performed no stress tests on them. A photograph of the bonded samples is shown in Figure 5.4.

The symmetric signals from the bonded YIG and ferrite samples are shown in Figure 5.5. The indium bonded samples produce the smallest signal in both cases, and it is essentially zero in the ferrites. The epoxied, YIG samples produce smaller signals than the 0.002" copper electrode without adhesive, but the ferrites produce larger signals. The structure of the ferrite signal is also different.

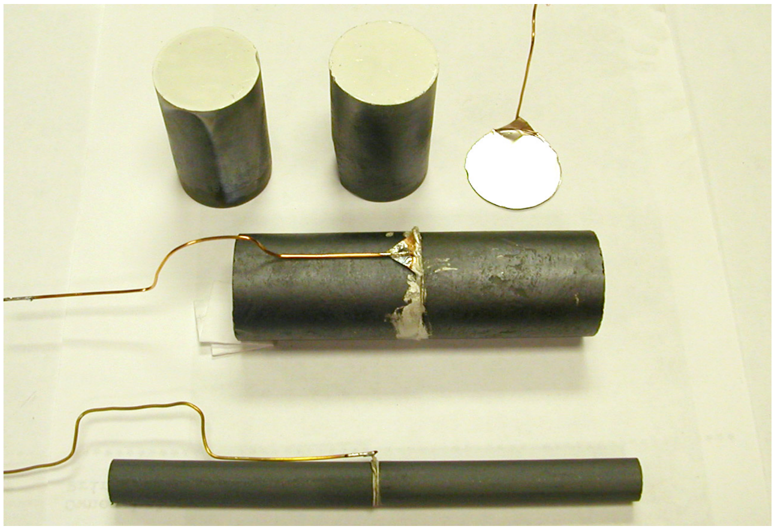

Figure 5.4: The bonded samples. From top to bottom: YIG cylinders and electrode before bonding, all with vacuum-deposited indium; epoxied YIG cylinders; indium-bonded ferrites.

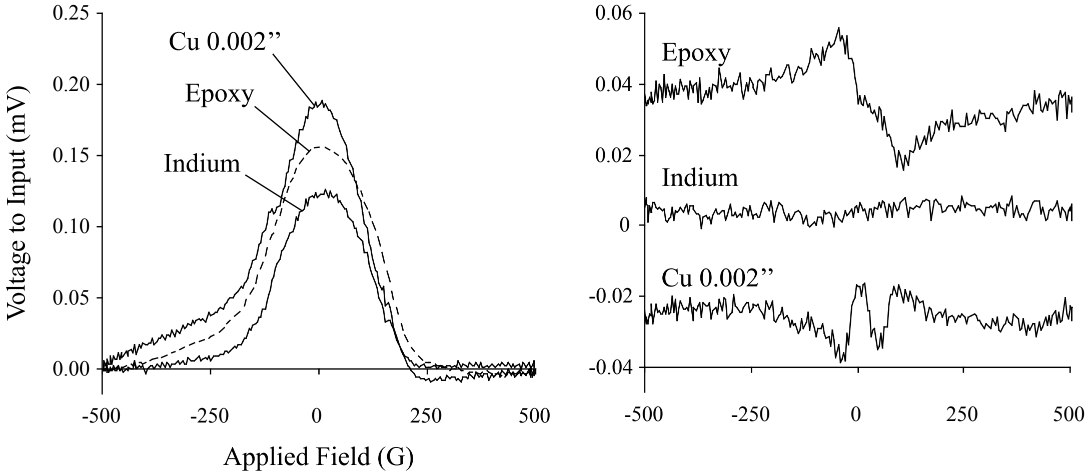

(a) (b)

Figure 5.5: Signals from samples bonded with silver epoxy and indium; the electrodes are 0.002" copper. 0.002" Cu is included for comparison. (a) YIG cylinders, (b) Ferrites, again displaced for clarity.

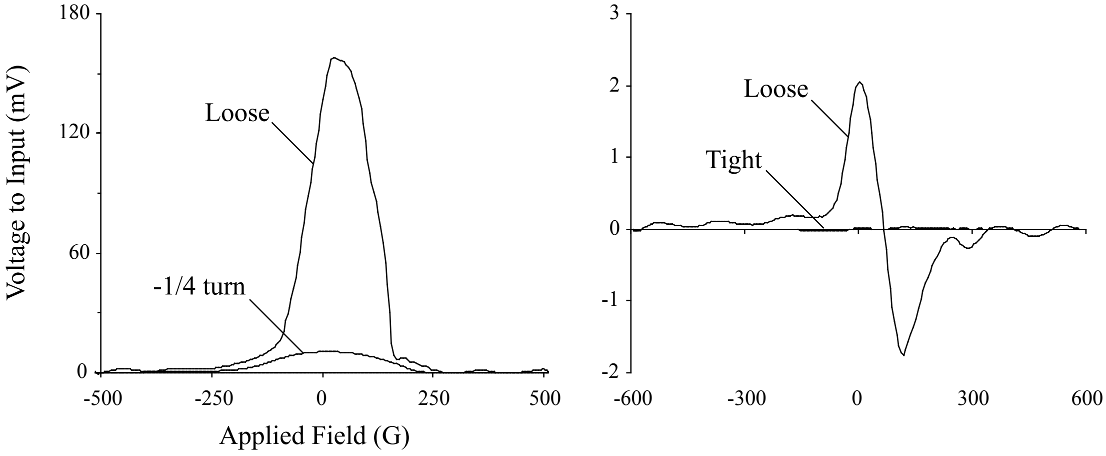

(a) (b)

Figure 5.6: Varied brace pressure on the YIG and ferrites with 0.02" Cu electrodes. (a) YIG cylinders: the signal increases by 3 orders of magnitude when the brace is fully loosened; the fully tight curve is thinner than the x-axis, but has qualitatively the same shape. (b) Ferrites: the signal increases by two orders of magnitude.

5.4 Pressure Variation

Preliminary results from the YIG toroids demonstrate that varying the brace pressure significantly affects the size of the symmetric signals that we observe. We explored this further in these experiments, using both various metal electrodes and the bonded samples.

5.4.1 Metal Electrodes

Loosening the pressure on the YIG samples with a 0.02" copper electrode increases the size of the symmetric signal by three orders of magnitude. The signals from the ferrites increase by two orders of magnitude, and exhibit both positive and negative bumps. These results are shown in Figure 5.6. Pressure variation in the YIG toroids, by comparison, yields large, negative signals from both the YIG toroids and the ferrites (Figure 4.10).

Softer, metal electrodes between YIG all yield similarly large and positive signals when the braces are loosened. Results from indium, lead, and tin are shown in Figures 5.7a, b, and c, respectively. None is quite as large as the copper signal, but all are two orders of magnitude larger than the signals from tightened braces. Indium electrodes between the ferrites yield signals identical to those from copper, as shown in Figure 5.7d. Because the signals from all electrodes change in qualitatively the same way when the braces are loosened, we conclude that these large, positive signals are independent of the electrode type.

5.4.2 Bonded Samples

The bonded samples, by contrast, do not exhibit significant increases in their signal sizes as the braces are loosened. Indeed, the signals remain on the same order of magnitude as the those from the metal electrodes without any adhesive. These results are shown in Figure 5.8. The signals from epoxied YIG increase by only a factor of two, and those from the indium-bonded YIG barely at all.

The symmetric signals from the indium-bonded ferrites increase dramatically, though they are negligibly different from the signals from 0.002” copper electrodes, shown in Figure 5.3. The increases only seems large because the symmetric signals from the indium-bonded ferrites are so unusually small.

5.4.3 Dielectrics

Large signals are also observed when dielectric material is inserted between the electrodes and the samples, as shown in Figure 5.9. The signals from YIG with both copper and lead electrodes are positive when a single sheet of 0.001” mylar is inserted; they increase positively as the braces are loosened. The signal from the ferrites with a lead electrode starts as negative, when the brace is tight, and grows to a larger, positive signal as the brace is loosened.

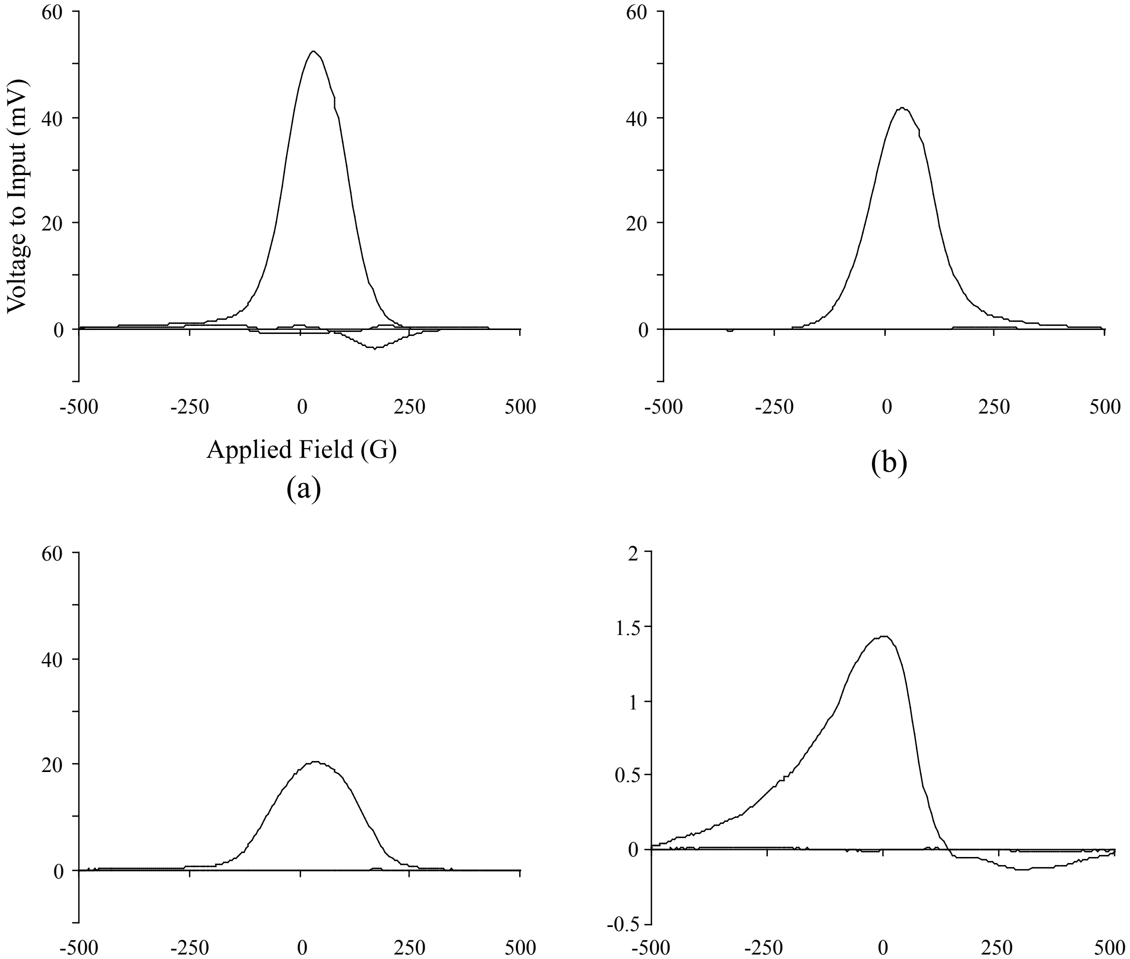

(a)

(b)

(c)

(d)

Figure 5.7: Softer, metal electrodes give large, positive, symmetric signals when the braces are loosened. In all cases, the large, positive curves are from fully loosened braces. The small curves barely visible above the x-axes are from tightened braces. (a) YIG with In; the negative curve is from the loosened brace before the electrode was peeled off of the sample. (b) YIG with Pb, (c) YIG with Sn, (d) Ferrite with Pb.

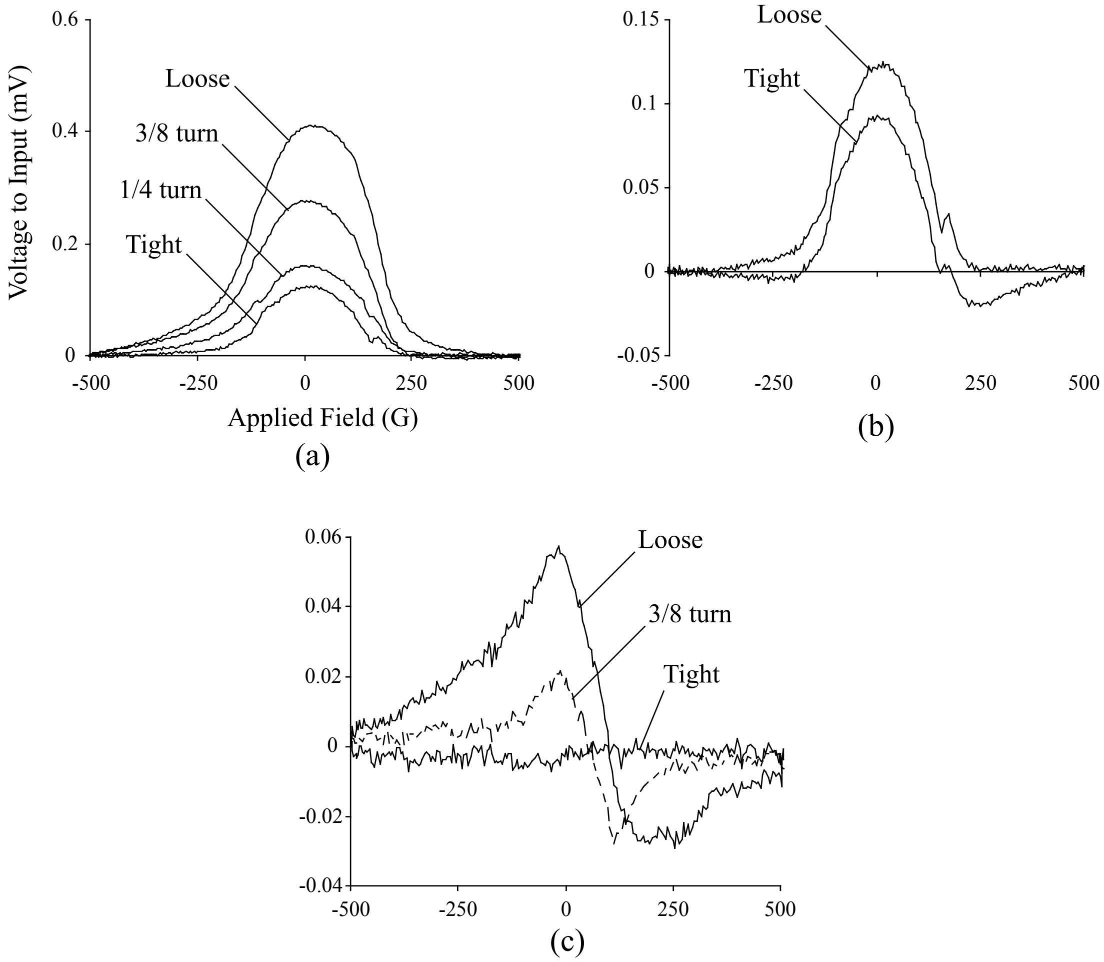

Figure 5.8: Varied brace pressure on the bonded samples. (a) YIG with silver epoxy, (b) YIG indium bonded, (c) Ferrite indium bonded.

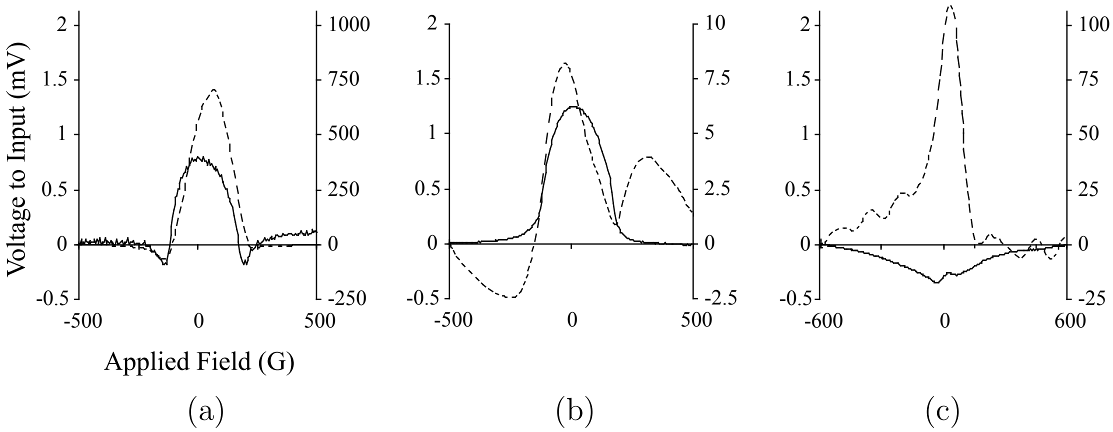

Figure 5.9: Symmetric signals with one sheet of 0.001" mylar inserted above and below the electrode. Solid curves indicate high brace pressure, and are measured against the primary axis. Dashed curves indicate low pressure and are measured against the secondary axis. (a) YIG cylinders with 0.02" Cu, (b) YIG cylinders with Pb, (c) Ferrites with Pb.

We therefore conclude that dielectric material positively increases the signals from loosened braces. The YIG signal from copper increases by three orders of magnitude when the brace is loosened, and that from lead by one order of magnitude. The ferrite signal increases by over two orders of magnitude. The signals from the tightened braces also have unexpected shapes, particularly from the lead electrode in YIG. Comparing the signals from copper electrodes between YIG with and without dielectric material, we see that mylar increases the size of both the tight and loose signals by a factor of 4. However, this relationship cannot be extended to the lead electrodes because the shapes of the signals are so significantly changed.

These results should be compared with those in Figures 4.9 and D.9. By contrast, mylar between the YIG toroids usually yields large, negative signals, and sometimes equally large positive ones. The results presented in this section are much more reproducible.

			Response (mV)	
Sample and Brace	Electrode	Dielectric	Tight	Loose
YIG Toroids, Plastic	Cu 0.02”	none	20	200
		mylar 1x	60	2,000
Ferrites, Plastic	Cu 0.02”	none	40	60
YIG Cylinders, Brass	Cu 0.02”	none	1	50
		mylar 1x	100	2,000
	Epoxy	n/a	5	40
	Indium	n/a	< 1	70
Ferrites, Brass	Cu 0.02”	none	1	200
		mylar 1x	30	600
	Indium	n/a	2	6

Table 5.2: Amplitudes of microphonic responses of the model system.

5.5 Microphonics

We observe that the microphonic sensitivity of the model system decreases dramatically when we switch to the conductive braces. When collecting data from the old, plastic braces, we are unable to touch the table on which the model system rests or vibrational noise will overwhelm the signals of interest. The brass braces diminish the microphonic responses enough that intentional excitations are typically imperceptible.

To be quantitative, we tested the response of the system by dropping a small block of wood onto the bottom plate from a height of 1.5”. The amplitudes of the initial responses are given in Table 5.2, and two example traces are shown in Figure 5.10. Looser braces uniformly give larger responses, with signals typically an order of magnitude larger than those from the tight braces. Mylar increases the microphonic response of every metal electrode, and plastic braces give larger signals than brass braces.

These trends are the same as those observed in the symmetric signals due to the applied, magnetic field. The exceptions are the bonded samples, where the microphonic responses increase but the electrode signals remain unchanged as the braces are loosened. We interpret this as further evidence that the large, positive signals are

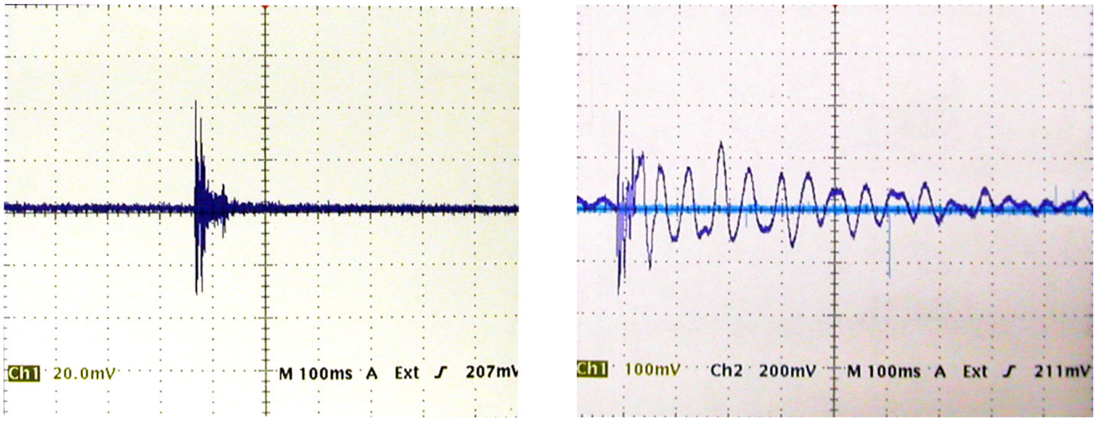

(a) (b)

Figure 5.10: Examples of microphonic responses of the model system. (a) Tightened brace, (b) Loosened brace.

due to motional effects.

5.6 Force Sensors

Results from the pressure tests reveal that decreasing the pressure on the electrode induces larger signals. One source of such pressures is the force of magnetic attraction between the samples as they magnetize; this is simply the force of attraction between two dipoles placed with opposite ends adjacent. To understand better these interactions, we purchased force sensors that can be placed between the samples within the model system, and measured the force as a function of applied field.

The details of the sensors themselves, including the circuity and calibration equations, are discussed in §D.5; in this section we simply cite the results. Figure 5.11 shows the measured force of attraction between the samples as a function of applied field, for tight and loose braces. We note that the force between the YIG cylinders increases rapidly as the applied field nears ±300 G, and then appears to saturate. We consider this strong evidence that the samples adequately magnetize in our applied fields. If considered upside down, this curve bears a striking resemblance to many

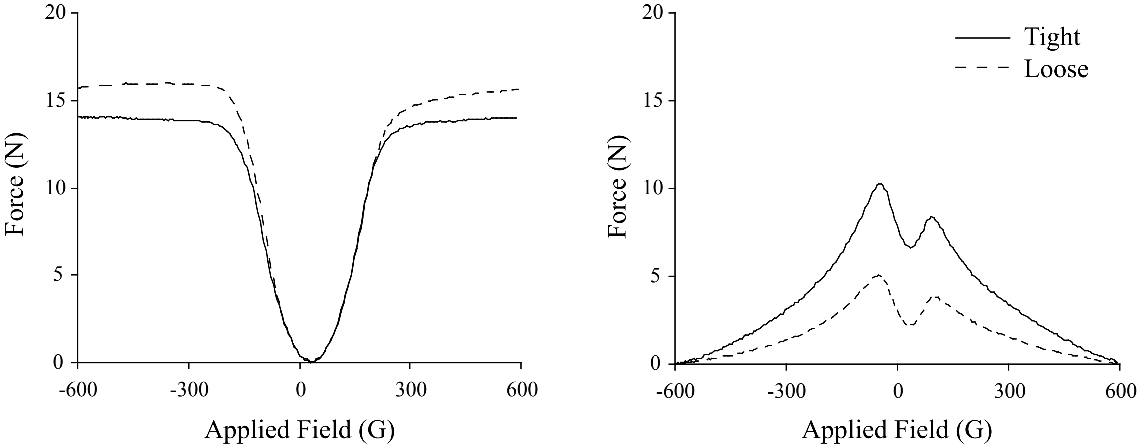

(a)

(b)

Figure 5.11: Forces of magnetic attraction between the samples as a function of applied field; the static force due to the tightened brace has been subtracted. Tight braces provide approximately 4,400 N of force, and loose braces 900 N. (a) YIG cylinders, (b) Ferrites.

symmetric signals that we observe.

The ferrite signal is currently not understood because it shows that the force of attraction increases as the applied field decreases. However, we make some preliminary remarks regarding its structure in §6.2. Loosening the braces has an opposite effect in each sample. The force of attraction between the YIG cylinders increases somewhat as the braces are loosened, but the force between the ferrites decreases.

Chapter 6

Conclusion

In this chapter we consider the essential results of our experiments and several trends that emerge. Some analyses of data are shown, but these are merely the prelude of future work. Relationships between the symmetric signals observed in the model system and the M-Even effect are then discussed, along with potential explanations. Future prospects for these experiments and for the larger apparatus are given to close.

6.1 Summary of Results

In our experiments with magnetic materials in the model system, we observed various signals that were symmetric upon reversal of the magnetic field. These signals were largely irreproducible at first, but, by altering our methods of mounting samples, we have begun to observe consistent signals. Specifically, we now apply pressure to the samples and mount them in fully conductive braces.

We reproducibly observe symmetric signals of different sizes, shapes, and signs from different metal electrodes. The largest signals are from gold and indium, and the smallest from tin. Variation is also observed in the ferrite signals.

The signals from samples mounted in conductive braces are roughly an order of magnitude smaller than those from samples in plastic braces. The signals increase positively when brace pressure is decreased, and these increases can reach three orders of magnitude. Bonded samples do not exhibit the same sensitivity to pressure variations as do the samples without adhesive. The signals from these samples increase only two-fold at most. Dielectric material between the sample and the electrode also increases the signal size by up to two orders of magnitude.

Microphonic responses scale approximately with the sizes of the symmetric signals. They are worst in loosened, plastic braces with dielectric materials, and best in tightened, conductive braces without dielectric materials. Microphonic noise from the bonded samples increases as the braces are loosened, unlike the sizes of the symmetric signals.

These are the most obvious trends apparent from our data and comprise the bulk of our results. However, other interesting trends emerge if we examine the signals from the metal electrodes in greater detail.

6.2 Electrode Analyses

The signals from the metal electrodes and force sensors display some structural features that merit further examination. We combine and scale these data in various ways, and find that the resulting curves often mimic those from other tests. There is no *a priori* reason to suspect that the data can be combined in such fashions. These analyses are included as motivation for future research.

6.2.1 Signals Versus Magnetization

The earliest signals that we observed with the model system bear little resemblance to the M-Even effect in the EDM apparatus. These signals generally resemble Gaussian curves, whereas the M-Even signals display a dip, rise, drop, and $1/H$ decay, as shown in Figure 3.5b. However, the conductive braces significantly improve our data and we now observe that the softer, metal electrodes yield signals with some structural similarities to the M-Even effect.

Consider the negative of the signal from the zinc electrode between YIG, shown in Figure 5.3. This demonstrates the same dip, rise, and $1/H$ decay that are characteristic of the M-Even effect, although the region of the dip is significantly longer. We may partially explain these differences by considering the signals as functions of magnetization rather than of applied field, as they have typically been displayed.

To plot these data versus magnetization, we must consider sample hysteresis. The cylindrical samples have relatively strong demagnetizing fields, so for small fields their magnetizations track the applied field closely. Data from the force sensors, shown in Figure 5.11, show that this approximation fails beyond approximately 300 G, when the samples magnetically saturate. The GdIG toroid, by contrast, has relatively small demagnetizing fields. It therefore requires a stronger coercive field to flip its magnetization, and approaches saturation much more rapidly. Ben Heidenreich and Kyle Virgien measured a hysteresis loop for the GdIG sample at 127 K; it is shown in Figure 6.1. From these data we see that the coercive field for the sample is approximately 8 G, and by 15 G the sample is almost entirely re-magnetized.

The hysteresis loop demonstrates the nonlinear relationship between the applied field and the sample magnetization. As H passes through the coercive field, the magnetization suddenly changes by 80% of its range, yet the applied field has changed little. This accounts for the difference between the dipped regions of the zinc signal and the M-even effect, both of which occur around zero applied field. With a little footwork, we may show the signals to be qualitatively very similar.

Figure 6.2a shows both the zinc and M-even signals versus applied field, as they are usually displayed (the M-Even signal has been inverted). We now take the hysteresis loop in Figure 6.1 to be the relationship between applied field and magnetization for

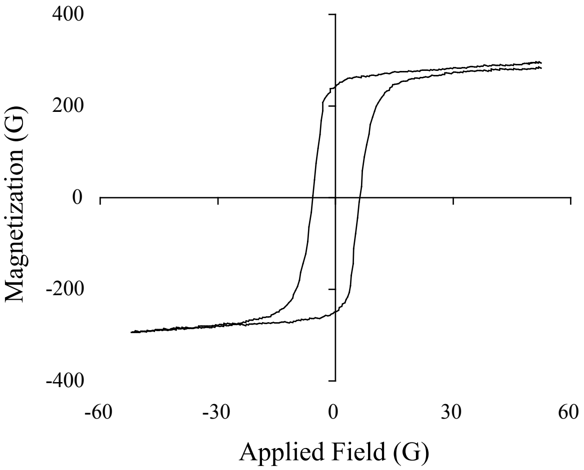

Figure 6.1: Hysteresis loop for the GdIG toroid at 127 K, from summer 2005.

the GdIG toroid, and modify it to form an approximation of the same relationship for the YIG cylinders.[1] Less hysteresis implies that the coercive field for the cylinders is approximately zero, so we shift the curve horizontally; the slower rise to saturation implies that the curve should be horizontally stretched. The final curves that we choose are shown in Figure 6.2b.

We now plot the symmetric signals in Figure 6.2a against these modified magnetization curves, and results are shown in Figure 6.2c. (The domain of the M-Even signal is linearly stretched to match that of the zinc signal, for the purposes of these comparisons). Here we have attempted to compare the signals from soft, metal electrodes between the YIG cylinders in the model system to the M-Even effect observed in the GdIG toroid. The qualitative features of the curves now appear similar, which suggests that the signal from the zinc electrode may be analogous to the M-Even effect. The signals from the tin, lead, zinc, and indium electrodes all share this characteristic shape.

---

[1] This doesn't quite work because the YIG cylinders are at room temperature, not 127 K, and GdIG has contributions to its magnetization from gadolinium ions in addition to iron ions.

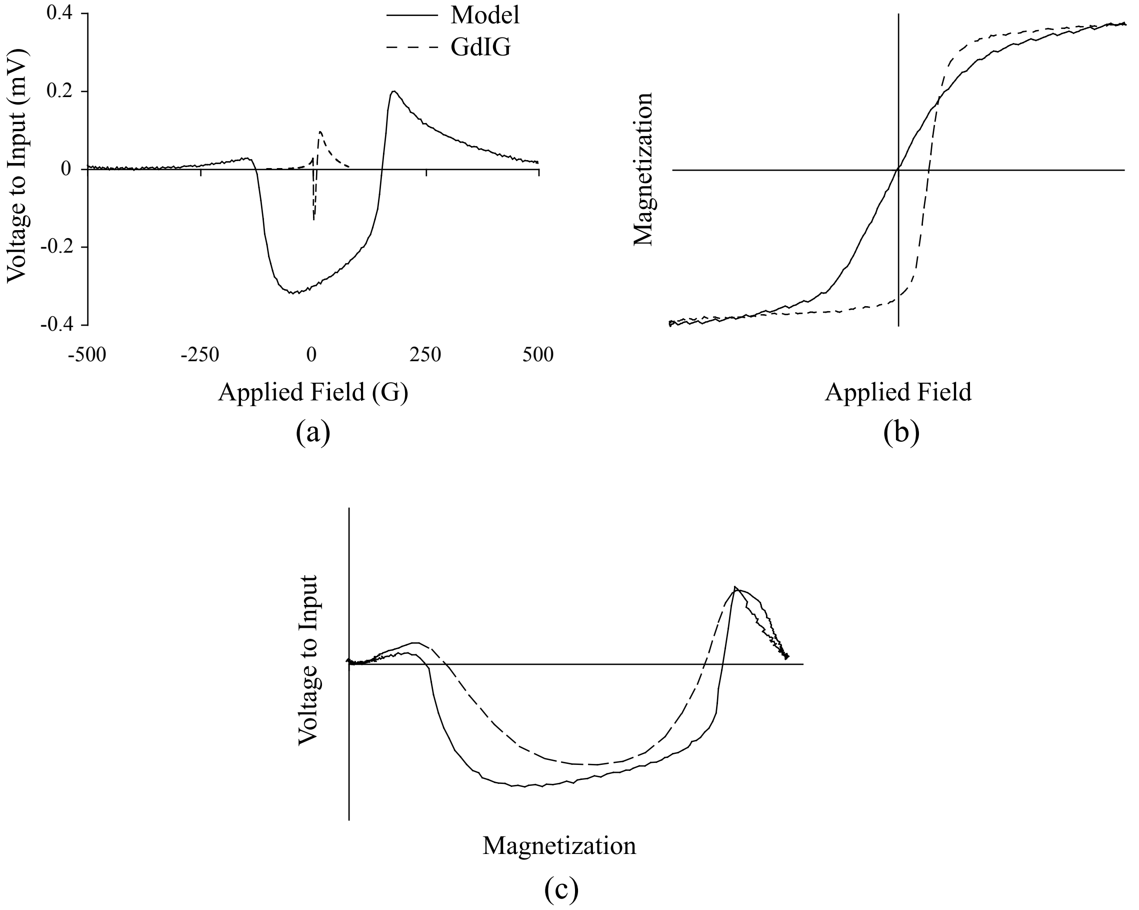

(a) (b) (c)

Figure 6.2: Comparing the signal from a zinc electrode in the model system to the M-Even effect at 127 K. Solid curves are the Zn electrode, and dashed curves are the M-Even effect. (a) Signals versus applied field. (b) Magnetization curves used for comparison. (c) Scaled signals versus magnetization.

6.2.2 Metal Combinations

Another interesting trend emerges if we consider the signals from brass electrodes between YIG, shown in Figure 5.3. This curve is approximately Gaussian, but has small dips to either side of zero applied field. Visual inspection indicates that this shape might be the sum of two signals, one fairly smooth and positive, and another with negative bumps.

We choose the thick copper and zinc curves as test functions to examine further this possibility. Superimposing nine-tenths of the copper signal with one-tenth of the zinc signal gives a curve which is almost indistinguishable from the brass signal. Interestingly, these are the two components of brass, although the compositional ratio is typically 70% Cu and 30% Zn. These results are shown in Figure 6.3a.

We note two other interesting combinations of this form, shown in Figures 6.3a and b. First, the anomalously large gold signal emerges if we instead take the difference between the copper and zinc signals, scaled somewhat differently.[2] Second, the tin signal is approximated by adding adding those from copper and lead.

We currently have no explanation for these observations, though it seems unlikely that these relationships indicate a chemical interaction between the YIG and the electrode. Rather, we imagine that the signals depend on some physical properties of the electrodes, such as their hardnesses and elasticities. These electrodes may represent particular values of relevant, physical variables. Accordingly, the signals that we observe may be superpositions of two or more fundamental shapes.

---

[2] We might instead say that gold and zinc add to copper, for consistency. However, our observations indicate that the copper signal is characteristic of an entire class of electrodes, whereas gold is unusual.

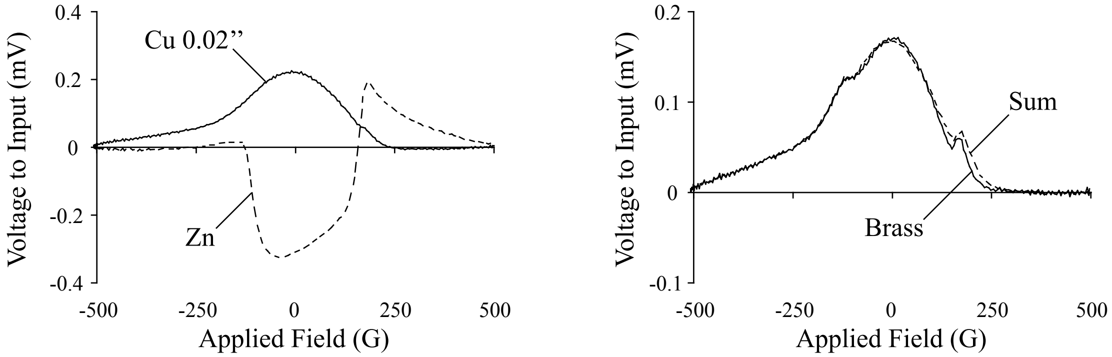

(a) Brass ≈ 0.9(Cu 0.02") + 0.1(Zn)

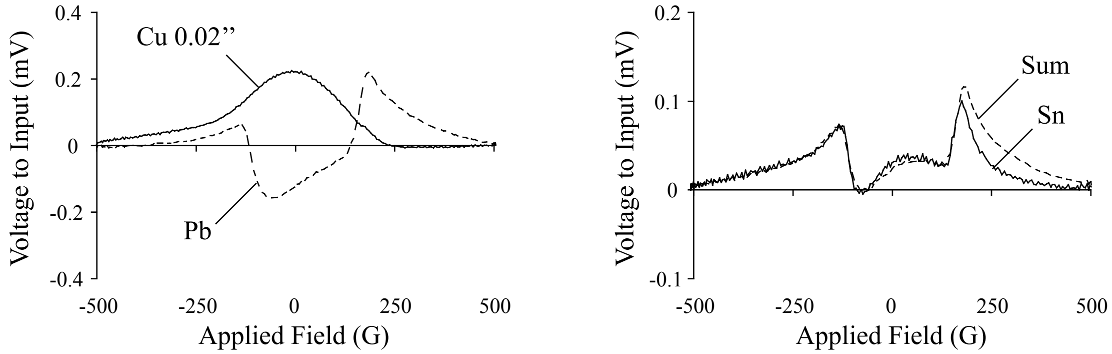

(b) Sn ≈ 0.33(Cu 0.02") + 0.44(Pb)

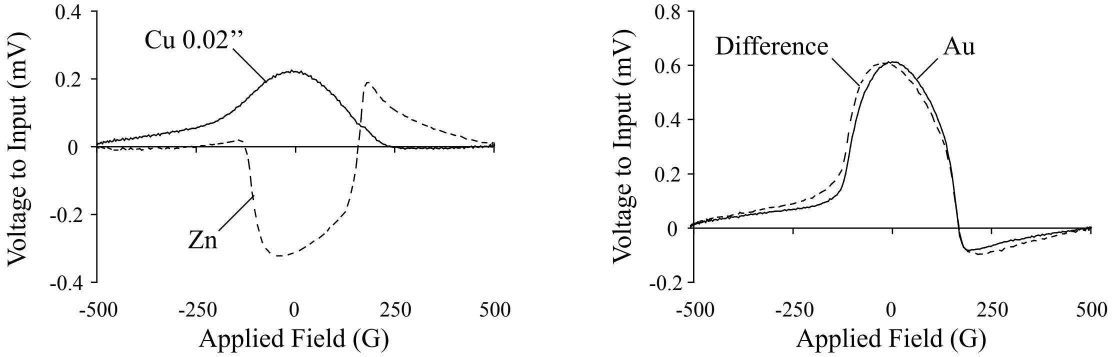

(c) Gold ≈ 1.6(Cu 0.02") − 0.8(Zn)

Figure 6.3: Combinations of the symmetric signals from metal electrodes. The curves on the left are scaled and added as indicated to form those shown on the right.

6.3 Force of Attraction

Data from the force sensors regarding the force of attraction between the magnetized YIG cylinders give us considerable insight into the physical behavior of the samples during magnetization. Figure 5.11a shows that the cylinders attract each other with approximately 14 N of force at 500 G of applied field, which we find to be reasonable based on a simple, physical model. These results are discussed in the following section, after which we extend them to a basic interpretation of forces in the GdIG toroid.

6.3.1 YIG Cylinders

Consider two identical, magnetized samples placed with opposite ends adjacent. If they are close enough together that edge effects can be neglected, then the field between them will be approximately constant. If the samples are identically magnetized then all field lines leaving the north pole of one will eventually close into the south pole of the other. Figure 6.4 shows a diagram of this model.

We calculate the force of attraction between the samples as the gradient of the field energy in the gap between them. The energy density of a magnetic field is given by [13, §7.2]

$$u = \frac{1}{2\mu_0} B^2, \tag{6.1}$$

and the energy in the gap is therefore

$$U = \frac{1}{2\mu_o} B^2 A l, \tag{6.2}$$

where $A = 7.3 \times 10^{-4}$ m is the cross-sectional area of the YIG, and l is the length of the gap. The force of attraction between the samples is the derivative of this

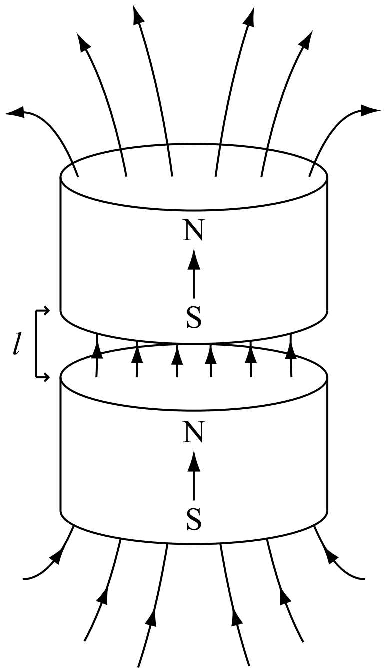

Figure 6.4: Model of the field from the cylindrical samples. The field is approximately constant in the gap.

expression with respect to l, which is

$$F = \frac{dU}{dl} = \frac{1}{2\mu_0} B^2 A. \tag{6.3}$$

This force is quadratic in the applied field and independent of the gap size, in the limit of small separations. This is a good approximation given that the YIG cylinders are each 2" long, but the force sensors are only 0.007" thick. The gap is therefore approximately one-thousandth the total length of the samples, and the ratio $l/\sqrt{A}$ is 7×10^{-3}. The gap should therefore negligibly perturb the field.

To find the field in the gap, we consider the magnetic properties of YIG. Yttrium ions contribute nothing to the total magnetic moment of the sample, so the total field is due to the iron ions. These contributions are shown in Figure 2.3. At 0 K, fully magnetized YIG will have a net magnetic moment of 5 μ_B per formula unit. At room temperature this drops by roughly 20%, and so the net moment is taken to be 4 μ_B

per formula unit. The magnetization of YIG at room temperature is therefore

$$M \approx \left(\frac{4\mu_B}{\text{formula unit}}\right)\frac{1}{3}n_{\text{Gd}}, \tag{6.4}$$

where we recall that 1 $\mu_B = 9.274 \times 10^{-24}$ J/T is one Bohr magneton, and $n_{\text{Gd}} = 1.235 \times 10^{22}$ cm^{-3} is the number density of rare-earth ions per unit volume in iron-garnets.

The magnetization is most conveniently expressed in Gaussian units, in which the magnetic flux density is defined as

$$\mathbf{B} = \mathbf{H} + 4\pi\mathbf{M}. \tag{6.5}$$

We calculate the magnetization via the same logic as in §2.3.3, and find it to be approximately 1900 G. Our applied field reaches a maximum strength of 500 G. Substituting these results into Eq. 6.5, we find the flux density in the gap between the samples to be approximately 2400 G.

This value is converted back into SI units by the conversion 1 T = 10^4 G, such that the total flux density is 0.24 T. Substituting this result into Eq. 6.3, we find the force of attraction between the samples at magnetic saturation to be 17 N. This value agrees closely with the measured forces shown in Figure 5.11b, which shows the attractive force to be 14 N at 500 G. These values differ at least partially because the samples do not *fully* magnetize in our applied field; however, the difference is only 20%.

Data from the force sensors reveal interesting behavior in both the YIG and the ferrite samples. We compare these curves to select signals presented in chapter 5, and note their similarities. The YIG force curve, if considered upside down, is roughly Gaussian and bears striking resemblance to many signals that we observe. Figure 6.5a shows this signal compared to those from the indium-bonded YIG and a loose,

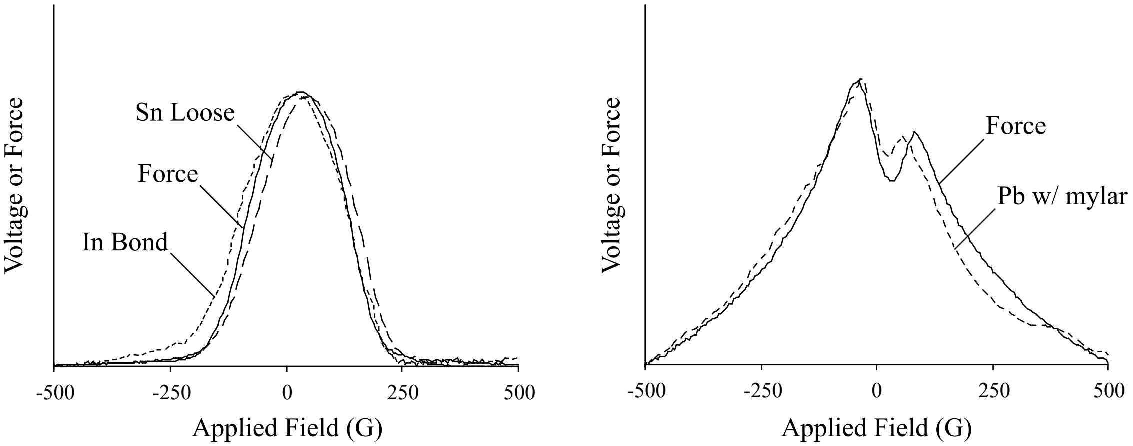

(a) (b)

Figure 6.5: Force curves compared to selected, symmetric signals. Force curves are solid lines, and electrode signals are dashed. (a) YIG, force curve inverted. (b) Ferrites, electrode curve inverted

tin electrode; all curves have been scaled arbitrarily. These are two of many such possible superpositions.

These results indicate that the roughly Gaussian signals that we observe may share the same dependence on the sample magnetization as does the force of attraction. We note additionally that the force is approximately quadratic in the applied field for small values of H. This is the region in which the magnetization varies approximately linearly in the applied field, such that $B \propto H$. By Eq. 6.3 the force is therefore quadratic in H, in agreement with our observations.

The ferrite force curve is not currently understood because it implies that the force of attraction increases as the field decreases. However, its shape is remarkably similar to the signal from lead electrodes, between ferrites and mylar with the brace tightened. This signal is shown in Figure 5.9c, and a comparison with the force curve is shown in Figure 6.5b. The lead curve has been inverted and scaled aribtrarily. No other signals with this shape were observed, but the similarity here is unmistakable.

One theory to explain the ferrite force curve is that the samples may undergo significant magnetostriction. This is the process by which a material's dimensions change when it is exposed to a magnetic field [32, ch. 8]. The magnetic domains align parallel to the applied field, attracting along the magnetization axis and repelling perpendicular to it. This translates into a net contraction along the magnetization axis, and expansion in the perpendicular plane. Deformations are measured as $\delta l/l$, and typically range from 10^{-6} to 10^{-5}.

It is currently unclear whether such effects could account for the apparent decrease in pressure on the force sensor when the ferrites are magnetized. Further research into the magnetostrictive properties of the Ni-Zn ferrites may be required to understand this behavior.

6.3.2 GdIG Toroid

The GdIG toroid behaves analogously to the YIG cylinders because its internal field, although toroidal overall, is perpendicular to the gap created by the electrode plates. We may therefore approximate its force of attraction by the same methods described above, with Figure 6.6 as our picture. However, the two halves of the toroid are differently doped with gadolinium ions and so their magnetizations are not generally the same. These differences substantially change the behavior of the toroid during a field pulse.

When the applied field is on, the two halves magnetize to their respective saturation values and are therefore not flux-matched. The field then turns off and the more magnetized half quickly demagnetizes to the level of the lesser. The entire toroid is then observed to lose another 23% of its magnetization. The total magnetization of the toroid during data collection is therefore only 77% of that of the less magnetized half.

The total magnetization of each half of the toroid is given as a function of temperature in Figure 2.14b. From these data we calculate the total magnetization after

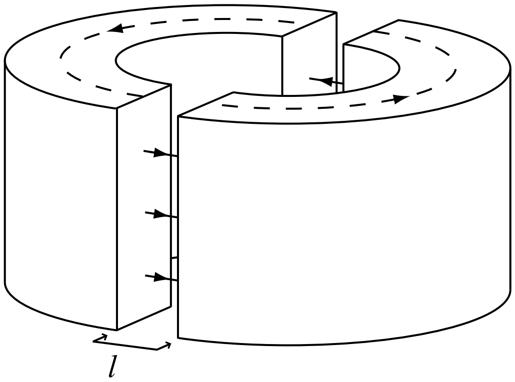

Figure 6.6: Model of the field from the GdIG toroid. The field is approximately constant in the gap.

Temperature	$M_{1.8}$ (μ_B)	$M_{1.35}$ (μ_B)	Total M (μ_B)
88 K	2.2	0.5	0.4
127 K	0.6	0.6	0.5
178 K	0.4	1.3	0.3

Table 6.1: Total magnetizations of the halves of the GdIG toroid at the operating temperatures. Data for $M_{1.8}$ and $M_{1.35}$ are from Figure 2.14b.

a field pulse at each of the operating points, 88 K, 127 K, and 178 K. These results are given in Table 6.1.

We may now solve for the total flux density by Eq. 6.5, and the force by Eq. 6.3. (The cross-sectional area of the toroid is 11.7 cm^2, and we double the force to reflect the total attractive force due to both electrodes.) These results are shown in Table 6.2. According to this model, the forces of attraction between the halves of the GdIG toroid are approximately two orders of magnitude smaller than those between the YIG cylinders. The M-Even effect, by comparison, has approximately the same size in both the model system and the EDM apparatus.

If the symmetric signals that we observe in the model system represent the M-Even effect, then these results imply that the effect is largely independent of the magnitude of the attractive force between the samples. However, some interesting trends emerge if we consider in greater detail the changes that occur in the sample's

Temperature	Flux Density (G)	Force (N)
88 K	190	0.34
127 K	240	0.54
178 K	140	0.18

Table 6.2: Flux densities and forces of attraction in the GdIG toroid at the operating temperatures.

magnetization during a field reversal.

The field within the toroidal Faraday cage is nonuniform, and varies as $1/r$. When the applied field is on, the inner edge of the sample will be twice as magnetized as the outer edge, and the forces of attraction should differ by a factor of four. To confuse matters further, the coercive fields are different for each half, so one will flip before the other; this could lead to momentary *repulsion*.

If we suppose that the M-Even effect is related to changes in the attractive force between the samples, then we may hypothesize some connections. We identify four regions of interest in the M-Even signal, as shown in Figure 6.7. Based on the magnetic behavior of the toroid during a field flip, we propose the following associations.

1. **Slight decrease as $\mathbf{H} \to 0$**: Decrease in force as the magnetization decreases.
2. **Sharp rise**: One half of the toroid flips, momentary repulsion;
3. **Sharp dip**: The other half flips, attraction restored;
4. **$1/H$ decay**: Magnetization increases and approaches saturation as $1/H$ [34].

Further experiments are required to examine these possibilities in greater detail. They would be aided by a more precise model of the time-varying force between the toroid halves as the field flips.

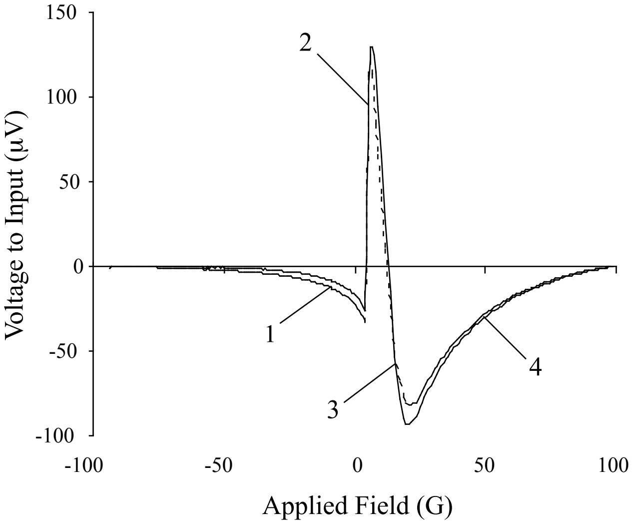

Figure 6.7: The M-Even signal at 127 K, reproduced from Figure 3.5b.

6.4 Relations to M-Even Effect

The analyses in §6.2.1 imply that the signals we observe from the softer, metal electrodes may indeed correspond to the M-Even effect observed in the GdIG toroid. This is the most convincing evidence of any connection between the signals that we observe in the model system and the systematic effect of interest in our larger apparatus.

We also observe other signals of significantly different character, typically resembling positive, Gaussian curves. These signals increase dramatically when we alter the method of assembly, either by loosening braces or inserting dielectric material, but it is not clear that such alterations are directly relevant to the M-Even effect. These Gaussian signals are certainly not observed in the EDM apparatus, although we have not tried making these sorts of adjustments. However, these signals are highly reproducible, magnetically symmetric, and of the same order of magnitude as the M-Even effect. We therefore have no reason to discount them as irrelevant at present.

Both the epoxied and indium-bonded samples exhibit exclusively Gaussian signals in the model system, although these do not increase when the braces are loosened.

It is possible that these signals overwhelm whatever M-Even effect may be present in this geometry. The combinations of data from the metal electrodes seem to support this. The tin electrode provides an excellent example: it has the same general features of the M-Even signal, yet we may approximate its shape by adding the zinc signal to the nearly Gaussian, copper signal. If this is true, then refining the model system to remove these positive signals must be the next priority in our research.

Perhaps, instead, the M-Even effect truly varies in the manners that we have observed. If this is the case, then we have learned a considerable amount about its nature and variability. Its causes, however, are presently unclear. Some connections have been proposed as motivation for future research, but these are tentative.

6.5 Possible Systematic Effects

Our data imply that motional effects can create extremely large signals with the same symmetry as the M-Even effect. For example, the differences between the responses of the bonded and non-bonded samples to pressure variation indicate the presence of effects that depend on the relative motion of the samples and electrodes. The symmetry of the effects is expected because the forces involved with flipping sample magnetization from up to down and down to up are identical.

Our results are therefore largely consistent with the presence of motional effects, and these should be considered if the GdIG toroid is modified in the future. Even if the M-Even effect is independent of sample motion, other symmetric signals evidently do depend on it and could eventually limit our resolution.

The decreases in microphonic sensitivity and symmetric signal size that we observe when using the conductive braces indicate that insulating materials should be kept far from the electrodes. It is hypothesized that static charge may build up on insulating surfaces, creating in-homogeneous fields through which our electrodes move. We have the same concerns for the EDM apparatus. For example, the microphonic sensitivity of the system dropped significantly when we removed styrofoam spacers from around the electrode wires [2, §6.8].

If these theories are correct, then any insulating material around the electrode is a potential source of large, symmetric signals. The GdIG toroid is currently mounted on a ceramic base that is an extremely good insulator. We do so to maintain high resistance from the electrode to ground, but perhaps this risks the unfavorable accumulation of static charge.

6.6 Future Prospects

Through the experiments described in this thesis, we have significantly improved the sensitivity of the model system. The data that we collect are now largely reproducible, and we have begun to make insightful comparisons.

In a larger sense, we have reached an exciting moment. Strong evidence exists that the model system reproduces the M-Even effect, and interesting patterns emerge from the data. Based on the combinations of metal electrode signals presented in this chapter, one might imagine specifically selecting an alloy to minimize the amplitude of the resulting signal. We have considered coating copper electrodes with tin and indium as preliminary tests of these possibilities.

A focused, theoretical model of the force of attraction between the two halves of the GdIG toroid during magnetic reversal would benefit our experiments enormously. Additionally, we have begun researching the magnetostrictive properties of GdIG and YIG. Combined work in these areas will help us to understand both the parallel and perpendicular forces acting on the electrodes as the magnetizations of the samples change.

We hope that future efforts will reveal a clearer understanding of the M-Even effect. Improvements to our apparatus may include reassembling the toroid with a different adhesive, different electrodes, or mounting it in an entirely new fashion. The current support structure provides no pressure on the electrodes, though it is quite rigid and minimizes stresses on the sample during temperature cycling. Modifications to this would be difficult, but we do not discount their possibility at this stage.

If the M-Even effect can be reduced, then the sensitivity of our apparatus should be greatly increased. Currently its signal is so large that it defines our data fit, and we must extrapolate its behavior to the high-field limit in order to calculate the potential asymmetry due to the electron EDM. Significant improvement beyond the M-Even effect will likely be necessary if our sensitivity is to reach the world limit, and we remain hopeful that such improvements are possible.

Appendix A

Schiff's Theorem

This appendix considers the non-relativistic shielding of electric dipole moments in atomic systems. In pariticular, Schiff found in 1963 that the first-order energy shift in an atomic system due to EDMs is zero, which would appear to exclude atomic systems from EDM searches. However, Sandars later extended this proof relativisitically and found results quite to the opposite [37]. Schiff's work is illuminating nevertheless, and the full mathematics have been included here. His proof assumes two conditions:

1. The system consists of charged, point particles with electric dipole moments whose distributions are equivalent to their charge distributions.

2. Particles move non-relativistically and interact electrostatically.

Schiff's theorem is a formidable proof and general within its postulates, but we may approach it with the benefit of hindsight.[1] Consider a system consisting of i charged particles with positions $\mathbf{r}_i$ situated in an electrostatic potential $V(\mathbf{r})$. Schiff describes the total Hamiltonian $\hat{H}$ of his model system as the sum of five terms, each of which describes a particular interaction. The first three terms, $\hat{H}_1$, $\hat{H}_2$, and $\hat{H}_3$,

---

[1] This proof follows from the brief outlines given in [5, 21, 37, 38]. Ben's thesis also includes the full mathematics, which differ only slightly from those presented here [2, §2.3].

account for particulate motion, inter-particle Coulomb forces, and interactions with the applied potential. They are defined by

$$\hat{H}_1 = -\sum_i \frac{\hbar^2}{2m_i} {\nabla_i}^2, \qquad \hat{H}_2 = \sum_i \sum_{j \neq i} \frac{q_i q_j}{2r_{ij}}, \qquad \text{and} \qquad \hat{H}_3 = \sum_i q_i V_j, \tag{A.1}$$

where ∇_i denotes differentiation with respect to the i^{th} particle's coordinates. These make no reference to electric dipole moments, and may be grouped as a single Hamiltonian $\hat{H}_0 = \hat{H}_1 + \hat{H}_2 + \hat{H}_3$.

The last two terms of $\hat{H}$ account for EDM interactions with the applied potential and with the fields created by other particles, respectively. They are defined by

$$\hat{H}_4 = -\sum_i \frac{d_i}{q_i} \sigma_i \cdot \nabla_i V_i, \qquad \hat{H}_5 = \sum_i \sum_{j \neq i} \frac{q_j d_i}{{r_{ij}}^2} \sigma_i \cdot \hat{\mathbf{r}}_{ij}, \tag{A.2}$$

where d_i is the constant of proportionality between each particle's dipole moment and spin, σ_i. These are grouped as an "EDM Hamiltonian," $\hat{H}_{edm} = \hat{H}_4 + \hat{H}_5$. If the presence of EDMs is a sufficiently small effect, then this Hamiltonian may be treated as a first order perturbation on $\hat{H}_0$. Furthermore, if $\hat{H}_{edm}$ can be expressed as (a scalar multiple of) the commutator of some operator and $\hat{H}_0$, then it will cause no energy shift in the eigenstates of $\hat{H}_0$, as we will demonstrate later. There will therefore be no energy shift to first-order in the dipole moments and their effects will be "shielded."

Rather than constructing an operator to satisfy the above conditions, we will posit the "infinitessimal displacement operator" $\hat{Q}$ and verify that it works.[2] It has the form

$$\hat{Q} = \sum_i \frac{d_i}{q_i} \sigma_i \cdot \nabla_i, \tag{A.3}$$

---

[2] Schiff chooses this name in his original paper [21], but some other sources refer to it as the "translation operator" [5, 38].

which is the same as given in [21, 38], and varies only slightly from other sources. The commutator $[\hat{Q}, \hat{H}_0]$ can be expanded into the sum of three commutators, each of $\hat{Q}$ with one of the terms of $\hat{H}_0$, such that

$$[\hat{Q}, \hat{H}_0] = [\hat{Q}, \hat{H}_1] + [\hat{Q}, \hat{H}_2] + [\hat{Q}, \hat{H}_3]. \tag{A.4}$$

To verify Schiff's theorem we will demonstrate that the sum of these commutator terms is equal to $-\hat{H}_{edm}$. Specifically, we will show that

$$[\hat{Q}, \hat{H}_1] = 0, \qquad [\hat{Q}, \hat{H}_2] = -\hat{H}_5, \quad \text{and} \quad [\hat{Q}, \hat{H}_3] = -\hat{H}_4, \tag{A.5}$$

which satisfy the requisite condition.[3]

Let us examine each of the terms in Eq. A.4 individually. The first can be manipulated directly to yield

$$\begin{aligned}[\hat{Q}, \hat{H}_1] &= \sum_i \frac{d_i}{q_i}\sigma_i \cdot \nabla_i \left(-\sum_j \frac{\hbar^2}{2m_j}{\nabla_j}^2\right) + \sum_j \frac{\hbar^2}{2m_j}{\nabla_j}^2 \left(\sum_i \frac{d_i}{q_i}\sigma_i \cdot \nabla_i\right) \\ &= -\sum_i\sum_j \frac{\hbar^2}{2m_j}\frac{d_i}{q_i}\sigma_i \cdot \nabla_i{\nabla_j}^2 + \sum_i\sum_j \frac{\hbar^2}{2m_j}\frac{d_i}{q_i}{\nabla_j}^2(\sigma_i \cdot \nabla_i).\end{aligned} \tag{A.6}$$

The spin vectors σ_i are position-independent and so we may rearrange the dot product in the last term to find

$$[\hat{Q}, \hat{H}_1] = \sum_i\sum_j \frac{\hbar^2}{2m_i}\frac{d_i}{q_i}\sigma_i \cdot [{\nabla_i}^2, \nabla_j], \tag{A.7}$$

---

[3] The various other descriptions of Schiff's theorem differ significantly in the terms they assign to each Hamiltonian. Sandars [37] includes the first four terms, but neglects to mention $\hat{H}_5$ (The inclusion of $\hat{H}_2$ but not $\hat{H}_5$ leaves the second commutator in Eq. A.5 incomplete.) Bigi and Sanda [5] include neither the second nor the fifth terms, easing the mathematics but making their argument less general. Bernreuther and Suzuki [38] provide no definition of $\hat{H}_0$. I have elected to follow Schiff and include all terms, but to treat them by methods similar to those implied by Sandars.

which is expressed in terms of the commutator $[\nabla_i{}^2, \nabla_j]$. Mixed partial derivatives commute and so the expression vanishes.

The second term in Eq. A.4 is treated similarly, although the mathematics are lengthier. We may accordingly manipulate it into a simpler commutator relationship by

$$\begin{aligned}
[\hat{Q}, \hat{H}_2] &= \sum_i \frac{d_i}{q_i}\sigma_i \cdot \nabla_i \left(\sum_{j \neq k} \frac{q_j q_k}{2 r_{jk}} \right) - \sum_{j \neq k} \frac{q_j q_k}{2 r_{jk}} \left(\sum_i \frac{d_i}{q_i}\sigma_i \cdot \nabla_i \right) \\
&= \frac{1}{2}\sum_i \sum_{j \neq k} \frac{q_j q_k}{q_i} d_i \sigma_i \cdot \nabla_i \frac{1}{r_{jk}} - \frac{1}{2}\sum_i \sum_{j \neq k} \frac{q_j q_k}{q_i} d_i \frac{1}{r_{jk}} (\sigma_i \cdot \nabla_i) \\
&= \frac{1}{2}\sum_i \sum_{j \neq k} \frac{q_j q_k}{q_i} d_i \sigma_i \cdot \left[\nabla_i, \frac{1}{r_{jk}} \right], \qquad \text{(A.8)}
\end{aligned}$$

where the last equality again invokes the commutativity of $\sigma_i \cdot \nabla_i$. The commutator in this expression is best understood by allowing it to act on a test function, because operators involving derivatives are not generally associative. To clarify, consider this brief example in which x and y are independent variables:

$$\frac{\partial}{\partial x}\big(y \cdot f(x)\big) \neq \left(\frac{\partial}{\partial x} y \right) f(x). \qquad \text{(A.9)}$$

The proper method is to operate consecutively from right to left. Allowing the commutator in Eq. A.8 to act on a test function, f, we find

$$\begin{aligned}
\left[\nabla_i, \frac{1}{r_{jk}} \right] f &= \nabla_i \left(\frac{1}{r_{jk}} f \right) - \frac{1}{r_{jk}} \nabla_i f \\
&= f \nabla_i \frac{1}{r_{jk}} + \frac{1}{r_{jk}} \nabla_i f - \frac{1}{r_{jk}} \nabla_i f \\
&= \left(\nabla_i \frac{1}{r_{jk}} \right) f, \qquad \text{(A.10)}
\end{aligned}$$

The effect of the commutator is therefore to multiply by $\nabla_i \frac{1}{r_{jk}}$. Explicit differentiation further simplifies this result to yield

$$\begin{aligned}
\nabla_i \frac{1}{r_{jk}} &= -\frac{1}{{r_{jk}}^2} \nabla_i r_{jk} \\
&= -\frac{1}{{r_{jk}}^2} \cdot \frac{1}{r_{jk}} \Big((r_{jk})_x \hat{\mathbf{x}} + (r_{jk})_y \hat{\mathbf{y}} + (r_{jk})_z \hat{\mathbf{z}} \Big) (\delta_{ij} - \delta_{ik}) \\
&= \frac{1}{{r_{jk}}^2} (\delta_{ik} - \delta_{ij}) \hat{\mathbf{r}}_{jk}. \qquad \text{(A.11)}
\end{aligned}$$

Using the result of Eq. A.11 in Eq. A.8, the commutator $[\hat{Q}, \hat{H}_2]$ becomes

$$\begin{aligned}
[\hat{Q}, \hat{H}_2] &= \frac{1}{2} \sum_i \sum_{j \neq i} \frac{q_j d_i}{{r_{ji}}^2} \sigma_i \cdot \hat{\mathbf{r}}_{ji} - \frac{1}{2} \sum_i \sum_{i \neq k} \frac{q_k d_i}{{r_{ik}}^2} \sigma_i \cdot \hat{\mathbf{r}}_{ik} \\
&= \frac{1}{2} \sum_i \sum_{i \neq j} \frac{q_j d_i}{{r_{ij}}^2} \sigma_i \cdot (\hat{\mathbf{r}}_{ji} - \hat{\mathbf{r}}_{ij}) \\
&= -\sum_i \sum_{i \neq j} \frac{q_j d_i}{{r_{ij}}^2} \sigma_i \cdot \hat{\mathbf{r}}_{ij}. \qquad \text{(A.12)}
\end{aligned}$$

The second to last equality follows because $\hat{\mathbf{r}}_{ji} = -\hat{\mathbf{r}}_{ij}$. This expression is equal to $-\hat{H}_5$, which is the interaction energy between the dipole moments and the fields created by each particle.

The third term of Eq. A.4 simplifies directly to

$$\begin{aligned}
[\hat{Q}, \hat{H}_3] &= \sum_i \frac{d_i}{q_i} \sigma_i \cdot \nabla_i \left(\sum_j q_j V_j \right) - \sum_j q_j V_j \left(\sum_i \frac{d_i}{q_i} \sigma_i \cdot \nabla_i \right) \\
&= \sum_i \sum_j \frac{d_i q_j}{q_i} \sigma_i \cdot [\nabla_i, V_j]. \qquad \text{(A.13)}
\end{aligned}$$

The commutator $[\nabla_i, V_j]$ is evaluated by similar methods to Eq. A.10, and so by allowing it to act on a test function f we find

$$\begin{aligned}
[\nabla_i, V_j]f &= \nabla_i(V_j f) - V_j(\nabla_i f) \\
&= (\nabla_i V_j)f + V_j(\nabla_i f) - V_j(\nabla_i f) \\
&= (\nabla_i V_j)f. \qquad \text{(A.14)}
\end{aligned}$$

The effect of this commutator is therefore to multiply by $(\nabla_i V_j)$. However, ∇_i differentiates only with respect to the i^{th} particle's coordinates, so this expression will vanish for all $i \neq j$. Inserting this result into Eq. A.13 we find

$$[\hat{Q}, \hat{H}_3] = \sum_i d_i \sigma_i \cdot \nabla_i V_i, \qquad \text{(A.15)}$$

which is equal to $-\hat{H}_4$, describing the interaction of EDMs with the applied potential.

Combining the results of Eqs. A.12 and A.15, the commutator $[\hat{Q}, \hat{H}_0]$ in Eq. A.4 becomes

$$[\hat{Q}, \hat{H}_0] = \sum_i d_i \sigma_i \cdot \nabla_i V_i - \sum_i \sum_{i \neq j} \frac{q_j d_i}{{r_{ij}}^2} \sigma_i \cdot \hat{\mathbf{r}}_{ij} \qquad \text{(A.16)}$$

This shows that $\hat{H}_{edm}$ may be expressed as the commutator of $\hat{Q}$ and $\hat{H}_0$,

$$\hat{H}_{edm} = -[\hat{Q}, \hat{H}_0], \qquad \text{(A.17)}$$

and the total Hamiltonian $\hat{H}$ of the system may therefore be written as

$$\hat{H} = \hat{H}_0 - [\hat{Q}, \hat{H}_0]. \qquad \text{(A.18)}$$

We have now only to show that the perturbation caused by $\hat{H}_{edm}$ is zero, which is in fact true of any first-order perturbation that can be expressed as a commutator with the unperturbed Hamiltonian. To be explicit, the first order energy shift ${E_p}^{(1)}$ associated with a perturbation $\hat{H}_p$ is given by

$$ {E_p}^{(1)} = \langle\psi|\hat{H}_p|\psi\rangle, \tag{A.19} $$

where $|\psi\rangle$ is an eigenstate of the unperturbed system.[4] If this perturbation is equal to the commutator of an operator $\hat{O}$ with the unperturbed Hamiltonian, $\hat{H}_p = [\hat{O}, \hat{H}_0]$, then the energy shift is identically zero:

$$ \begin{aligned} {E_p}^{(1)} &= \langle\psi|\hat{H}_p|\psi\rangle = \langle\psi|[\hat{O}, \hat{H}_0]|\psi\rangle = \langle\psi|(\hat{O}\hat{H}_0 - \hat{H}_0\hat{O})|\psi\rangle \\ &= E_0\langle\psi|\hat{O}|\psi\rangle - E_0\langle\psi|\hat{O}|\psi\rangle = 0 \end{aligned} \tag{A.20} $$

The second to last step follows because $\hat{H}_0$ is Hermitean and acts on either the bra or the ket to yield the eigenenergy E_0.

This result holds for $\hat{H}_{edm}$, and so the first-order energy shift due to electric dipole moments in any bound system satisfying Schiff's conditions is zero. This result seemed to doom future searches for the EDMs of charged particles, until 1965 when Sandars published his famous, relativistic examination of Schiff's theorem [22]. He showed that atomic systems in fact *enhance* the effects of the EDMs they comprise. The enhancement scales roughly as $\alpha^2 Z^3$, where $\alpha \approx 1/137$ is the fine structure constant, and Z is the atomic number [29]. Atomic enhancement is therefore better in heavier atoms, and can reach several orders of magnitude.

The mathematics of Sandars's proof are complex, and indeed far beyond my abilities. The reader is directed to [22, 37, 40, 41] for the original work.

---

[4] An overview of perturbation theory, focusing on first and second order calculations, can be found in [7, ch. 6]. For a more complete study see P. A. M. Dirac [39, ch. 7].

Appendix B

Detector Filter

A basic overview of the electronics involved in our EDM search is covered in the main body of this thesis; however, the specifics of our detector filter are located here. This chapter begins by motivating and explaining the use of complex variables in circuit analysis. We then apply these ideas to basic and more complex filters, and finish with a summarized analysis of the detector filter. Primarily, therefore, this appendix is concerned with *methods*; the actual analyses are quite basic with these in hand.

B.1 Ohm's Law Generalized

In order to examine circuits in a more powerful and ultimately illuminating way, we require the language of complex variables as they relate to circuits.[1] In order to motivate this shift, consider the following DC circuit (Figure B.1) in which a signal is connected to ground through a resistor and a capacitor in series.

If we assume negligible loading from the output, all current that flows through

---

[1] This discussion closely follows both the language and intent of Horrowitz and Hill's *The Art of Electronics*, [42, pgs. 23–37]. My words are ungainly and clumsy in comparison.

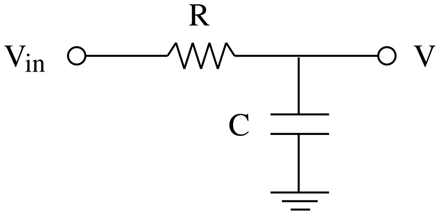

Figure B.1: A typical RC circuit.

the resistor then flows into the capacitor. Applying Kirchhoff's current law, we find

$$I = C\frac{dV}{dt} = \frac{V_{in} - V}{R}, \tag{B.1}$$

which is a differential equation describing how V changes in time. It has the solution

$$V(t) = V_{in}\left(1 - e^{-t/RC}\right), \tag{B.2}$$

where the product RC is known as the *time constant* of the circuit. Evidently, the voltage will increase from zero and approach V_{in} as the capacitor charges. This is a good description of the DC case, and invoking higher mathematics would be burdensome. But now consider applying a time-varying signal to the input, such as a sine-wave of form

$$V_{in} = V_0 \cos\omega t. \tag{B.3}$$

Eq. B.1 still applies, but to continue it is helpful to know more about the output signal.

The circuit above contains only *linear* devices (i.e. resistors, capacitors, and inductors), which allows us to conclude a useful property of its output signal: *an effectively linear circuit will output a signal of the same frequency as its input.* The only differences may be in amplitude and phase. Therefore, we may write Eq. B.1 for an AC circuit as

$$C\frac{dV}{dt} = \frac{1}{R}\big(V_0 \cos \omega t - V \cos(\omega t - \phi)\big), \tag{B.4}$$

where V is the amplitude of the output signal and ϕ is its phase shift.

One can imagine cascading such circuits and acquiring quite a headache from repeated trigonometric manipulations. The mathematics beg us to introduce complex variables via the Euler identity, $e^{i\phi} = \cos\phi + i \sin\phi$. While doing so will surely simplify the mathematics, it does add complexity to their interpretation. Let us be unambiguous from the start: voltage, current, resistance, capacitance, and inductance are all real quantities described by real numbers. As we switch to complex variables, we *represent* these quantities by boldface symbols and must somehow manipulate them at the end to recover their real values.

Sinusoidal potentials are our main signals of interest because any periodic, physical signal can be decomposed into such frequencies by Fourier analysis. The analysis of a sinusoidal input therefore encompasses all signals of interest, with the understanding that some contain many superimposed frequencies. Remembering that any linear circuit device will output a signal identical in frequency to its input, there is really no need to expressly consider that fundamental frequency, ω. We shall consider it understood and define our representative scheme accordingly. The only things left to define, then, are the amplitude and phase. We may express a sinusoidal voltage of form $V = V_0 \cos(\omega t + \phi)$ in the complex world as

$$\begin{array}{ccc} \text{Real Value} & & \text{Complex Representation} \\ V(t) = V_0 \cos(\omega t + \phi) & \rightarrow & \mathbf{V} = V_0 e^{j\phi}, \end{array}$$

where we have replaced i with $j = \sqrt{-1}$ to avoid confusion with electrical current, which is typically given the former symbol. The amplitude and phase are expressly included as V_0 and ϕ, respectively, and frequency is understood. To recover the real expression simply multiply $\mathbf{V}$ by $e^{j\omega t}$ (thereby recovering frequency) and take the real part.

Ohm's law may be generalized to include all linear circuit elements by following this example. To begin, we define the terms *reactance*, *resistance*, and *impedance.* Reactance is specifically the response of ideal capacitors and inductors because they have no resistance and therefore dissipate no power. Resistance is defined in the usual way. Impedance, given the symbol $\mathbf{Z}$, describes the total response of linear circuit elements to time-varying signals and is the sum of reactance and resistance. Ohm's law therefore states

$$\mathbf{V} = \mathbf{I}\mathbf{Z} \tag{B.5}$$

where $\mathbf{V}$, $\mathbf{I}$, and $\mathbf{Z}$ are complex representations.

Further simplifying matters, engineers often work in terms of the variable $s = j\omega$, which can be thought of as "complex frequency." In terms of s, the reactances of capacitors and inductors, given by X_C and X_L respectively, have values

$$X_C = \frac{1}{sC} \qquad \text{and} \qquad X_L = sL.$$

Because capacitors and inductors have no resistance, these are also their impedances. All future calculations will be done in terms of complex impedances as functions of s.

As a final aside, let us reconsider these representations as vectors, or *phasors*, in the complex plane. Without loss of generality we associate magnitude with amplitude and angle with phase. In terms of imaginary and real parts, they are given by

$$\text{Amplitude: } |\mathbf{V}| = \sqrt{\Re(\mathbf{V})^2 + \Im(\mathbf{V})^2}, \tag{B.6}$$

$$\text{Phase: } \phi = \arctan\left(\frac{\Im(\mathbf{V})}{\Re(\mathbf{V})}\right). \tag{B.7}$$

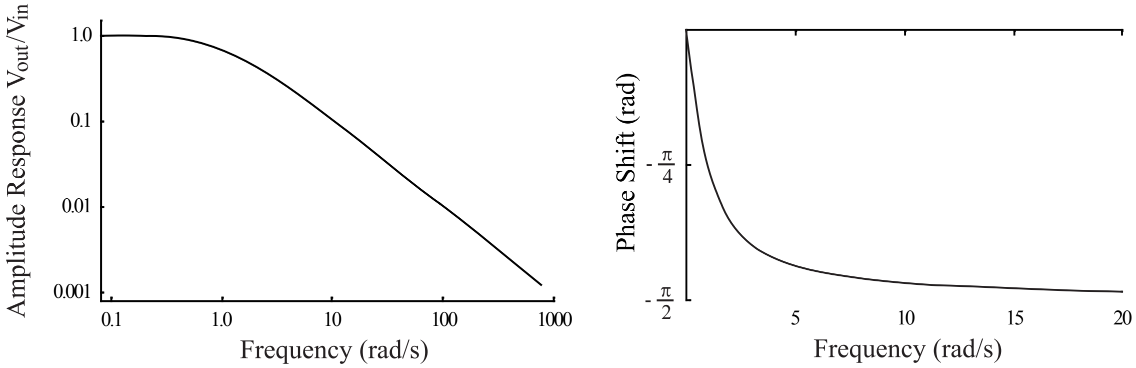

Figure B.2: Amplitude and phase responses of an RC filter.

These identities provide a direct method for finding the amplitude and phase of any signal for which the complex representation is known.

B.2 RC Filters

Let us return to the circuit in Figure B.1 and examine its behavior with the help of complex variables. Applying Ohm's law, Eq. B.5, we find that the ratio of $\mathbf{V}$ to $\mathbf{V}_{\text{in}}$ is

$$\frac{\mathbf{V}}{\mathbf{V}_{\text{in}}} = \frac{\mathbf{Z}_{\text{C}}}{\mathbf{R} + \mathbf{Z}_{\text{C}}} = \frac{1}{1 + RCs}. \tag{B.8}$$

By Equations B.6 and B.7, the amplitude and phase of the output are found to be

$$V = \frac{V_{\text{in}}}{\sqrt{1 + (\omega RC)^2}} \qquad \text{and} \qquad \phi = \arctan\left(-\omega RC\right), \tag{B.9}$$

revealing that this circuit is a "low-pass filter." This means that the output amplitude is *frequency-dependent* and attenuates high frequencies. Reversing the positions of the resistor and capacitor yields a "high-pass filter" whose behavior can be modeled in a similar fashion. Figure B.2 shows these results for a low-pass filter with $R = 1\ \Omega$ and $C = 1$ F.

As evidenced by the above figures, RC filters do not have an abrupt "cutoff frequency" beyond which signals are significantly attenuated. Rather, the amplitude response gradually declines and the filter is therefore not terribly useful for isolating similar frequencies. More advanced filters, however, can achieve magnificent attenuation through the use of op-amps. We now proceed to examine these *active* filters and begin by further developing a language to describe their performance.

B.3 Transfer Functions, Poles, and Decibels

Filters are described entirely by their amplitude and phase responses, and so may be characterized by a mathematical function containing this information. Such an expression is called the *transfer function* and is the primary quantity of interest in filter analysis.[2] It may be written formally as

$$H(s) = \frac{\mathbf{V}_{\text{out}}}{\mathbf{V}_{\text{in}}}. \tag{B.10}$$

We may alternately write H in polar form as

$$H(s) = Ge^{j\phi}, \tag{B.11}$$

where G is the gain of the filter. Solving for G and ϕ separately gives

$$G = \left|H(s)\right|, \tag{B.12}$$

$$\phi = \arctan\left|H\right|. \tag{B.13}$$

In cascaded, isolated filters, transfer functions commute. This means that filters can be connected one after the other, with appropriate isolating stages, and the overall transfer function is simply the product of each. Mathematically we find that each

---

[2] National Semiconductor provides an excellent online review of transfer functions and poles [43].

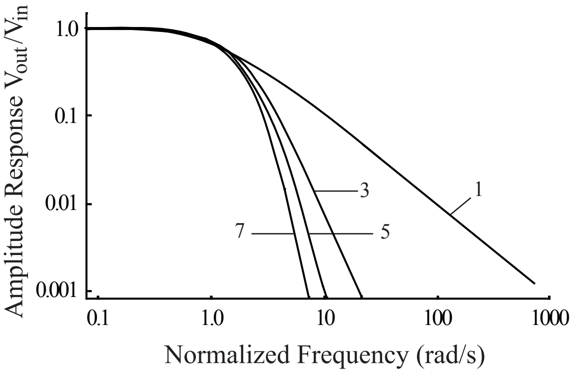

Figure B.3: Amplitude responses of cascaded RC filters.

capacitor in the circuit adds another power of s to the denominator of H, yielding an n^{th}-degree polynomial, where n is the total number of capacitors in the filter. This polynomial will have n zeros in the complex s-plane, corresponding to singularities in H that we refer to as *poles*. More poles generally result in better characteristics.

A convenient scale for comparing amplitude responses is the *decibel*, which is a logarithmic comparison that sets unity gain at zero. It is defined as

$$\mathrm{dB} = 20 \log_{10} \frac{A_2}{A_1} \tag{B.14}$$

(or more naturally for power as $10 \log_{10} P_2/P_1$). Amplitude responses are typically plotted either as decibels, or simply $\log A_2/A_1$, versus $\log \omega$, both of which tend to reveal filter characteristics more clearly. To normalize further the comparisons, frequencies are scaled such that each filter has its -3dB point (gain of $10^{-3/20} \approx 0.707$) at a frequency of 1 rad/s. An example of such a plot, comparing RC filters of increasing pole number, is shown in Figure B.3.

B.4 The Detector Filter

Active filters incorporate non-linear circuit elements such as op-amps to achieve remarkable filter characteristics. There are several different types of active, analog filters, but the most popular designs are the Chebyshev, Butterworth, and Bessel.[3] We shall focus our attention on the last because it is the design incorporated in our detector circuit. Figure B.4 shows the complete detector circuit as of April, 2007. It has been modified since the previous student thesis.

Bessel filters are renowned for their highly linear phase response, which causes minimal waveform distortion in the pass-band region. To demonstrate this, simply consider a sinusoidal voltage of form $V(t) = V_0 \cos(\omega t + \phi)$ and set $\phi = k\omega$, where k is some constant of proportionality. Minor rearrangement reveals that each frequency has been shifted in time by a constant amount $\Delta t = k$. Our experiment values this characteristic and we have therefore designed a 5-pole Bessel filter with its -3dB point at 80 Hz.

The filter consists of three isolated stages, the first of which is a low-pass RC filter isolated by a non-inverting op-amp with a gain of 56. The next two stages are two-pole active filters manufactured as ICs by Burr-Brown, Inc. They are two-stage active state filters consisting of three interconnected op-amps and a fourth to act either for gain or as a voltage follower. The transfer function for each IC is given by

$$H(s) = \frac{A_{LP}{\omega_n}^2}{s^2 + s(\omega_n/Q) + {\omega_n}^2}, \tag{B.15}$$

where A_{LP}, ω_n, and Q are interrelated quantities determined by component values [44]. With appropriate choice of components, the combined circuit can be modeled as a Bessel filter, and computer programs typically are used to solve these equations.

---

[3] These filters are so named because their transfer functions are mathematical expressions involving functions of the same names.

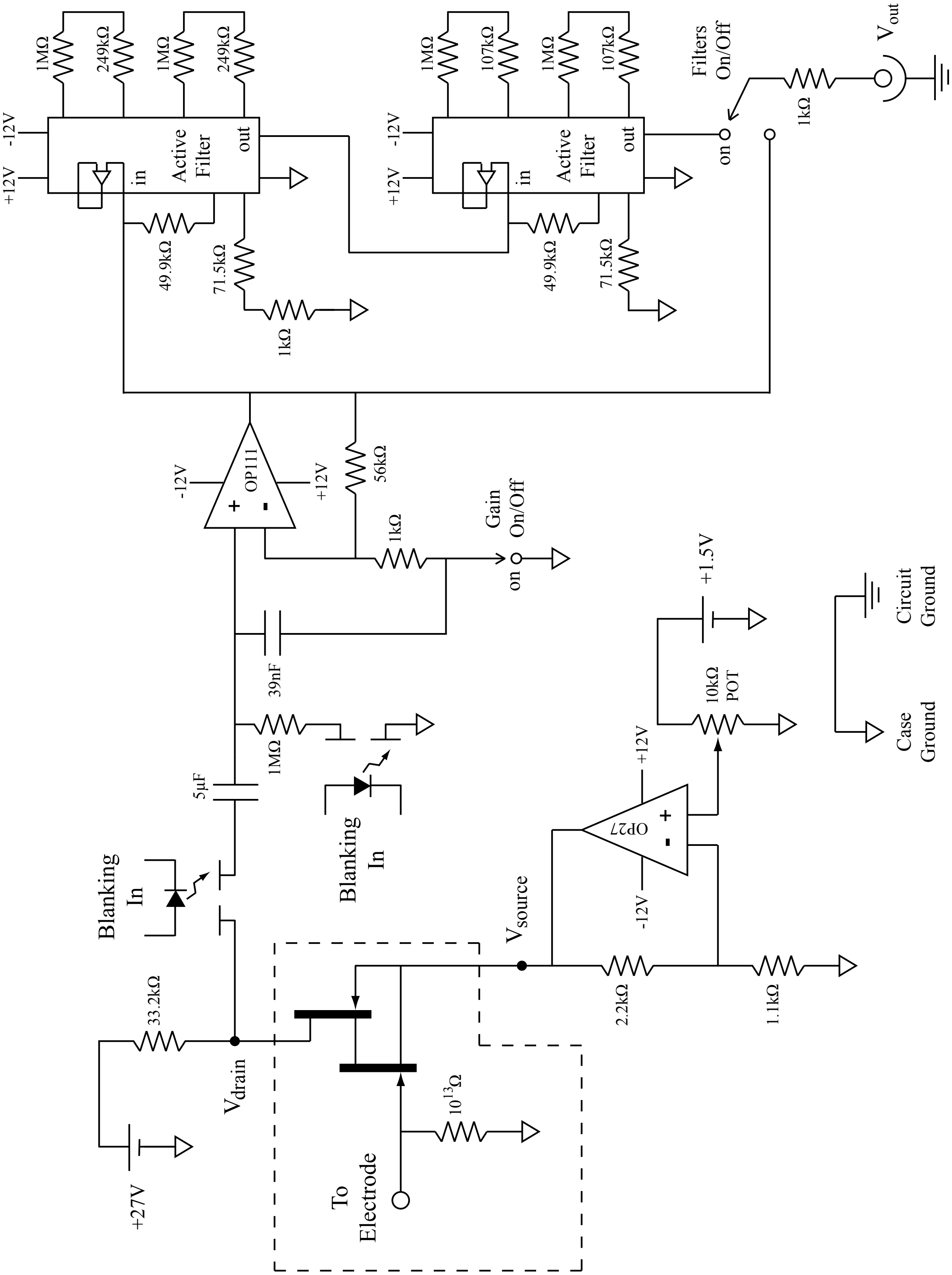

Figure B.4: The complete detector circuit. The boxed region is within the pre-amplifier.

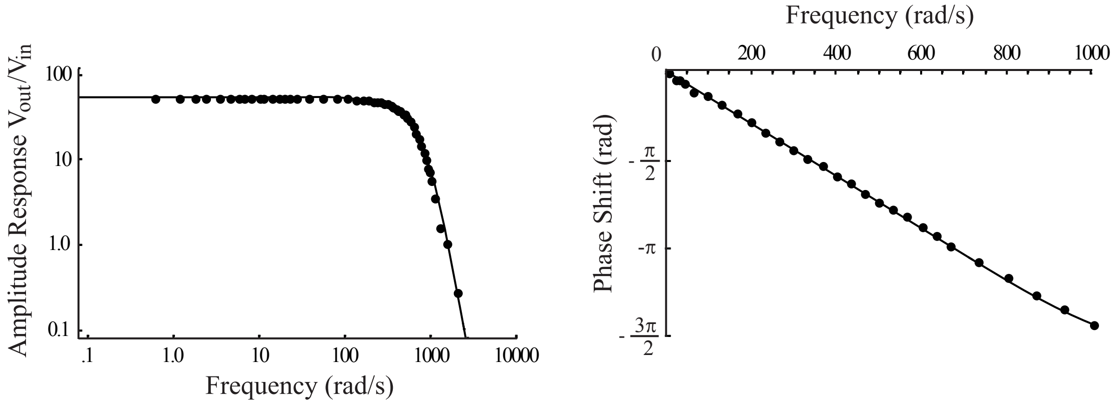

Figure B.5: Amplitude and phase responses of the detector filter. Measured data points are dots, and mathematical models are continuous lines.

The actual values chosen are shown in Figure B.4. To model the filter we multiply together the transfer function for each stage because they commute as stated previously. Equations B.12 and B.13 give the amplitude and phase response of the filter, as shown in Figure B.5.

The filter behaves as expected and matches the initial design specification that the -20dB point occur at 200 Hz. The phase shift is linear within and far beyond the experimental region of concern, and well beyond the passband. This results in imperceptible waveform distortion and adequate filtration of acoustic and vibrational noise.

Appendix C

The Apparatus

This appendix is intended as a brief, physical guide to the design of the apparatus. Along with chapter 2 this should provide the reader with a sense of how everything is physically constructed. Especially important are the methods that have been adopted to minimize noise and to regulate temperature. Chapter 5 of Ben's thesis treats much of the design in finer detail [2]; this is intended to condense the information into its essentials.

C.1 Sample Structure and Mount

As discussed in §2.3, our sample is a vertically-split toroid of GdIG, each half of which contains a different concentration of gadolinium ions. The sample is extremely resistive ($\sim 10^{15}$ Ω/m), so the two electrodes are essentially isolated from each other by the GdIG. To ensure that they remain isolated from ground, we mount the sample on a ceramic, macor base which is considered even more resistive than the GdIG. A photograph of the toroid on its base is shown in Figure C.1.

The sample is attached to the mount with a thin layer of Stix-All glue, which survives cycling through liquid nitrogen temperatures. The ceramic mount is attached

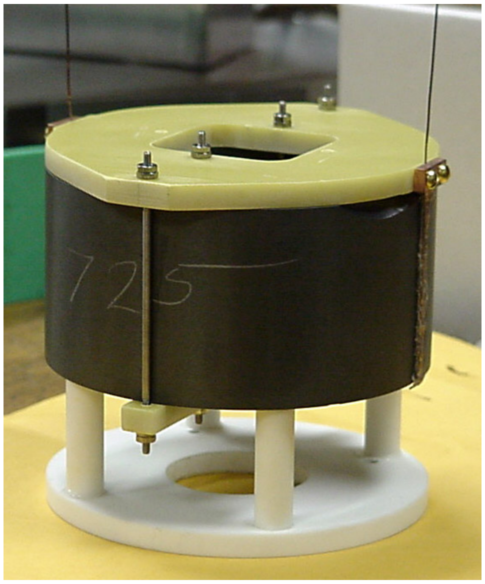

Figure C.1: The toroid situated on its ceramic mount. The G10 clamp for the electrode wires is visible, as is the chip on the 1.8 Gd side, to the right of the image.

to the surrounding Faraday cage with brass screws, anchoring it in place but allowing for easy removal. Electrode wires extend vertically from the sample and eventually attach directly to the gates of the JFETs in the pre-amplifier, which will be discussed in §C.3.

A clamp made from G10 board and titanium rods is attached to the sample. It clamps the electrode wires above the sample, after their connection to the electrode plate itself. Any tension applied to the wires is therefore transfered to the sample itself, and not to the joint between the wire and the electrode plate. This brace allows us significantly to tension the electrode wires, increasing the frequency of their microphonic responses. The detector filter, discussed in appendix B, effectively filters these frequencies. Titanium was chosen because its thermal expansion coefficient is similar to that of GdIG; they are 8.6×10^{-6} K^{-1} and 10.4×10^{-6} K^{-1}, respectively [45, 35]. This minimizes stresses during cooling.

C.2 Sample Faraday Cage

A toroidal Faraday cage surrounds the sample, and is encased by both a magnetic field coil and a heating coil. The heating coil is the inner of the two and is wound in the horizontal plane, but never in complete loops. This reduces any vertical field that its current might create.

The magnetic field coil is wound to create a circulating field. We calculate its flux density[1] by the equation

$$\mathbf{B}(s) = \frac{\mu_0}{2\pi} \frac{NI}{s} \hat{\phi}, \tag{C.1}$$

where $N = 336$ is the number of turns, I is the current, and s is the distance from the vertical axis of the toroid [13]. Approximating the radius as $s = 1.5''$, which is half way between the inner and outer radii of the sample, we find the flux density in terms of the current to be

$$\mathbf{B} = 17.6 \text{ G/A}. \tag{C.2}$$

The coil wrapping does not progress regularly about the axis of the toroid, but rather changes direction regularly. This decreases any vertical component of its field.

C.3 Pre-Amplifier

The first stage of signal amplification occurs in a circuit located within a small, brass case above the sample. This is referred to as the *pre-amplifier*. The electrode wires connect directly to the gates of JFET cascode pairs, which have extremely high input impedance. We decrease this impedance by connecting 10^{13} Ω resistors from the gate to ground. This circuit is shown in Figure C.2; its gain versus temperature curve is shown in Figure 2.12.

---

[1] I'm being a picky with terms here, by choosing *flux density* instead of *field*, but I do so for dimensional consistency.

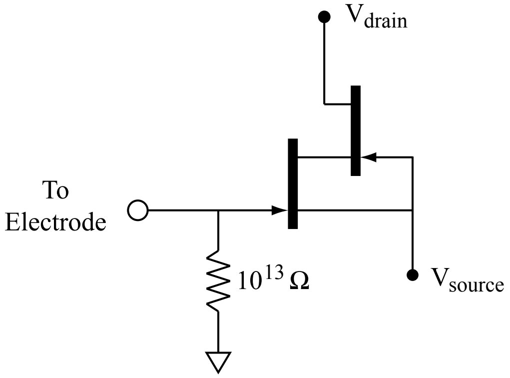

Figure C.2: The pre-amplifier circuit.

The temperature of the pre-amplier is controlled by two 50 W power resistors in series, the current through which is adjusted automatically to maintain a temperature of 127 K. A temperature diode between the resistors gives feedback to the temperature control box. Both the resistors and the diode are varnished onto the top of the pre-amplifier case, and a brass tensioning clamp holds them in place should the bond fail. At 127 K, the gain of the pre-amplifier is roughly 75.

C.4 Vacuum Can

The sample and pre-amplifier are contained within a larger vacuum can that is immersed in liquid nitrogen during cooling. The top and bottom flanges of the can are brass, and the sides are copper tubing. The can hangs down from wooden supports above, so that the apparatus does not touch the ground. A vacuum seal is maintained by compressing a thin bead of indium between the top flange and upper lip of the vacuum can. The top flange of the can is soldered to stainless steel tubes that carry the cables for all electronics within the can. These include voltage supplies for the pre-amplifier, field coil, pre-amplifier, sample heater coils, and temperature diodes. Stainless steel is an extremely poor thermal conductor, so the tubes remain at room temperature just a few inches above the level of the liquid nitrogen. A schematic diagram of the vacuum can, pre-amplifier, and sample cage is shown in Figure C.3.

The top of the pre-amplifier case is soldered directly to the stainless steel tubes that extend through the top flange of the vacuum can. The bottom of the pre-amplifier is held by brass side-panels that are screwed to the top. The sample Faraday cage is supported from beneath by an aluminum plate that is screwed to aluminum bars that extend vertically to the top flange of the vacuum can. To drop the sample cage, we unscrew the bottom plate from its support rods. The electrode wires extend to the pre-amplifier through guard tubes that are permanently attached to the sample Faraday cage, but not to the pre-amplifier. These slide out as the sample is lowered, though the electrode wires must be unsoldered from the pre-amplifier.

C.5 Temperature Regulation

The cold reservoir for the apparatus is the liquid nitrogen that surrounds the vacuum can. As previously mentioned, a heating coil on the sample Faraday cage and heating resistors on the pre-amplifier maintain the desired temperatures of these two units. Helium exchange gas is pumped into the system to accelerate heat transfer. At 88 K the system is particularly prone to heating from the field coil, and the helium helps to dissipate this heat.

Temperature control boxes are programmed to regulate the temperatures of both the pre-amplifier and the sample Faraday cage. The pre-amplifier temperature is held constant at 127 K because this falls in the ideal operating range of JFETs, and eases calculations of the gain. The sample cage is held at the appropriate operating point.

Temperature diodes are varnished to four points inside the vacuum can: the upper flange, the top of the pre-amplifier, the bottom support plate, and the sample Faraday cage. The temperature control boxes report the temperatures of these four diodes simultaneously. We are most concerned with the temperature of the sample Faraday

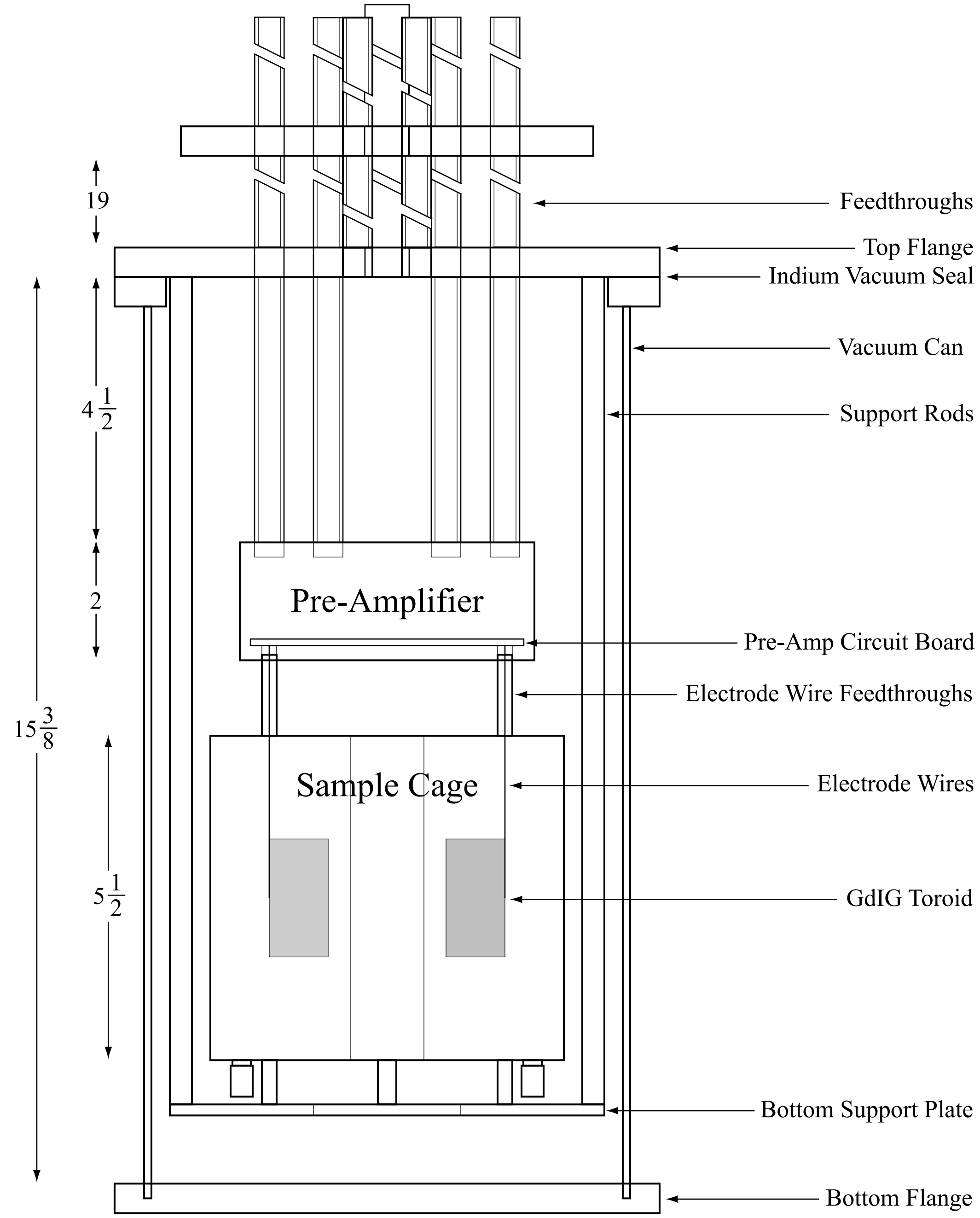

Figure C.3: Cross-section of the apparatus. Dimensions are in units of inches. (After [2, Figure 5.9].)

cage because this is the surface closest to the GdIG toroid.

GdIG is particularly sensitive to temperature gradients, and so we must be careful to vary its temperature slowly. The manufacturer recommends that we cycle the temperature at a rate of no greater than 20 K per hour, and to be safe we select the rate

$$\frac{dT}{dt} \leq 0.25 \text{ K/min}. \tag{C.3}$$

We use an iterative procedure to estimate the sample temperature. The rate of change of the sample temperature, T_S, is assumed to be directly proportional to its difference from the temperature of the Faraday cage surrounding it, T_{FC}:

$$\frac{dT_S}{dt} = k(T_{FC} - T_S), \tag{C.4}$$

where k is the constant of proportionality. As determined experimentally, k for our sample is roughly 3.7×10^{-3} min^{-1} in vacuum and 1.2×10^{-2} min^{-1} with exchange gas present [2, §5.5]. If T_{FC} changes linearly in time, then the time rate of change of the sample will never exceed that of the Faraday cage, as we now show.

Consider a general system with a sample of temperature T, initially at $T = T_0$, surrounded by a medium of temperature τ, initially at $\tau = \tau_0$. Suppose that the time rate of change of T is given by

$$\frac{dT}{dt} = k(\tau - T). \tag{C.5}$$

If we assume that τ changes linearly in time, such that $\tau(t) = ct + \tau_0$, then we find

$$\frac{dT}{dt} = ckt - kT + k\tau_0. \tag{C.6}$$

We now change variables to

$$u = ckt + k\tau_0, \qquad \text{and} \qquad \frac{du}{dt} = ck, \tag{C.7}$$

such that Eq. C.6 simplifies to

$$\frac{dT}{dt} = \frac{dT}{du}\frac{du}{dt} = ck\frac{dT}{du} = u - kT. \tag{C.8}$$

Rearranging slightly, and multiplying each side by $e^{u/c}$, this becomes

$$ce^{u/c}\frac{dT}{du} + Te^{u/c} = \frac{1}{k}ue^{u/c}. \tag{C.9}$$

The first two terms on the left may now be combined, to yield

$$c\frac{d}{du}(Te^{u/c}) = \frac{1}{k}ue^{u/c}. \tag{C.10}$$

Multiplying through by du and integrating both sides, we find

$$ck\int d(Te^{u/c}) = \int ue^{u/c}du. \tag{C.11}$$

The left hand side of Eq. C.11 is easily solved; it reduces to

$$ck\int d(Te^{u/c}) = ckTe^{u/c} + C_1. \tag{C.12}$$

The right hand side simplifies to

$$\int ue^{u/c}du = cue^{u/c} - c\int e^{u/c}du = (cu - c^2)e^{u/c} + C_2, \tag{C.13}$$

and we combine these results to yield a relationship in terms of T and u:

$$ckTe^{u/c} = c(u-c)e^{u/c} + C', \tag{C.14}$$

where $C' = C_1 + C_2$ is the total constant of integration. Because $u = ckt + k\tau_0$ is independent of T, we may isolate T directly. After some simplification, we find

$$T = ct - \frac{c}{k} + \tau_0 + Ce^{-k(ct+\tau_0)/c}. \tag{C.15}$$

The constant of integration is found by applying the initial condition that $T(t=0) = T_0$, which yields

$$C = \left(T_0 - \tau_0 + \frac{c}{k}\right) e^{k\tau_0/c}. \tag{C.16}$$

The final result for the temperature of the sample as a function of time is therefore

$$\boxed{T(t) = ct + \tau_0 - \frac{c}{k} + \left((T_0 - \tau_0) + \frac{c}{k}\right) e^{-kt}.} \tag{C.17}$$

The temperature of the sample will therefore change approximately linearly in time, with the same rate c as the external medium. Some transient, exponential terms decay relatively quickly, and at $t = 0$ the temperature is $T = T_0$ as expected. A graph of this function is shown in Figure C.4. This result is important in our cooling procedure because we may program the temperature control boxes to change their set-points at an arbitrary rate. According to these calculations, if we set the rate at -0.25 K/min then the sample cooling rate will never exceed that of the Faraday cage.[2]

Ideally, if the sample cooled from room temperature at the maximum rate, then

---

[2] A caveat to this bold statement is that the heaters have a limited range of operation. For example, when the vacuum can is immersed in liquid nitrogen, the heaters are unable to keep the sample Faraday cage above 165 K unless the helium exchange gas is pumped out. These calculations are general, but they are helpful to us only when the heating coil can actually control the sample cage temperature.

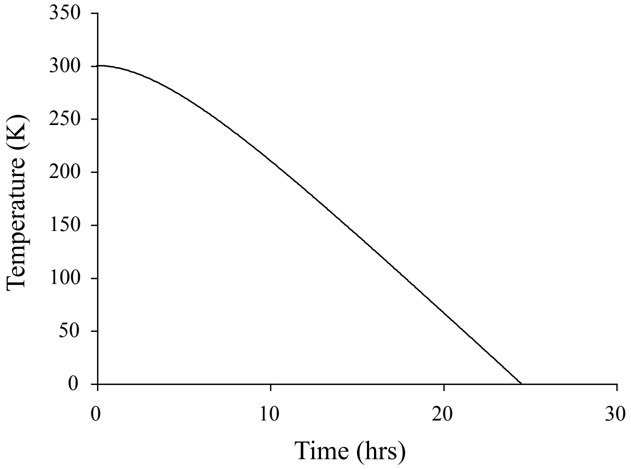

Figure C.4: A plot of the estimated sample temperature versus time when the Faraday cage cools at a linear rate. This curve is for $k_{vac} = 3.7 \times 10^{-3}$ min^{-1} and $c = -0.25$ K/min.

it could reach 88 K in just over 14 hours. According to these calculations, however, it would take approximately 18.5 hours if the Faraday cage started cooling immediately at the maximum rate. In reality, cooling takes considerably longer.

We experience delays in cooling for many reasons. The vacuum can must be cooled at a reasonably slow rate to prevent cracking that would compromise the vacuum seal. Improvements to its design have limited these failures, but they still occur with undesirable frequency. Heat transfer from the vacuum can to the sample Faraday cage is rather slow because the primary route is down to the support plate, up through the support bars, and into the top flange of the vacuum can. “Cooling fins” provide direct thermal contact between the field coil and the support rods, but the path to the cold reservoir is still indirect. This significantly delays the response of the Faraday cage to changes in the external temperature.

We are therefore unable to control carefully the sample temperature at higher temperatures, and so we proceed cautiously. Typically, liquid nitrogen is poured into the dewar surrounding the vacuum can until it is just below the bottom flange. The can then cools from the vapors until it has reached approximately 200 K. At this point we slowly immerse the bottom of the can by raising the dewar and topping up the liquid nitrogen as necessary. Soon thereafter, the entire vacuum can is immersed. The temperature regulators work constantly to ensure that the Faraday cage never cools faster than 0.25 K/min.

The vacuum can is kept immersed in liquid nitrogen during all data collection, which takes place between 88 K and 178 K. The heating coil does little work at 88 K, but at 178 K it must work at nearly full power constantly. To assist the heater, we pump out the exchange gas at 178 K.

Appendix D

Experimental Details

This appendix elaborates on the details of experiments performed with the model system. The essential results are outlined in chapters 4 and 5, but the methods and a more thorough interpretation of the data are located here. Each set of samples is considered independently and chronologically. A description of the force sensors and their involved circuitry is discussed to close. Illustrations of the braces constructed to hold the various samples may be found in §4.2 and §5.1.

Unless otherwise noted, all experiments presented in this appendix were conducted using a 1.1 Hz, 11 V peak-to-peak, triangular, driving waveform from the linear amplifier. This gives a maximum applied field of ±500 G within the solenoids. As in chapters 4 and 5, the signals have been decomposed via the methods of §3.2.2 such that only the symmetric contributions are displayed. (The antisymmetric contributions change little between experiments.) All traces have been additively adjusted so that they are zero-valued at the point of maximum applied field strength.

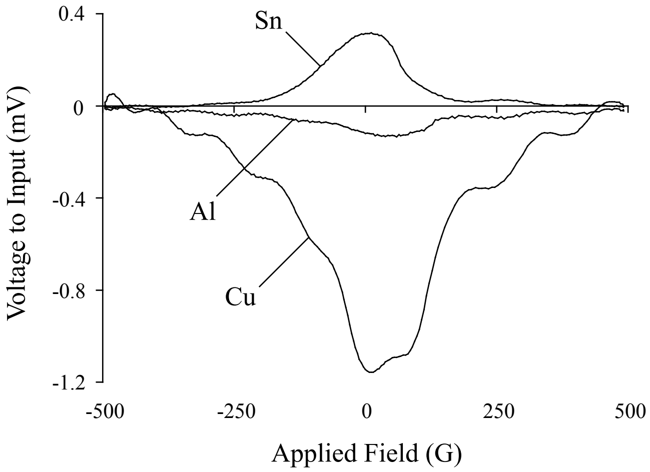

Figure D.1: Symmetric signals from different conductive, tape electrodes on the YIG cylinder. Electrode wires were soldered to copper and tin, but pressed to aluminum with a plastic zip-tie.

D.1 YIG Cylinder

D.1.1 Different Metals

The first set of electrodes that we used with the long, YIG cylinder were pieces of metal tape. These are thin strips of metal with conductive, acrylic adhesive. The tape is on the order of 0.001" thick and has a contact resistance of approximately 0.01 Ω.

As a first approach, we experimented with three different types of metals on the sample: copper, aluminum, and tin-plated copper. The first electrodes comprised five strips of copper tape, overlapped slightly to completely cover the middle half of the sample. Electrode wires were soldered to the top strips of copper and tin tapes, but pressed to the aluminum tape with a plastic zip-tie. The signals from these electrodes are shown in Figure D.1.

We note that copper and tin electrodes give signals of opposite signs, and that aluminum gives the smallest signal by far. Further experiments reveal that the observed sign differences are inconsistent. Some assemblies yield large, positive signals,

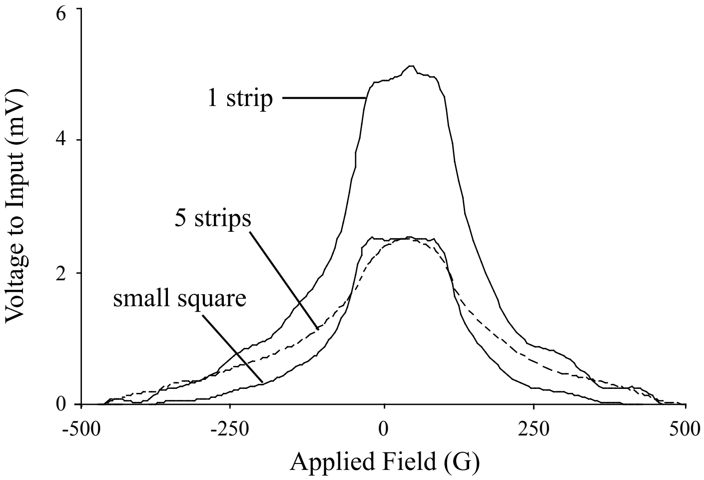

Figure D.2: Symmetric signals from copper electrodes of various sizes. The small square is approximately ten times smaller than one strip of tape.

and others equally large, negative ones.

D.1.2 Electrode Size

Direct observation reveals that electrode size has little effect on the size, shape, and reproducibility of the symmetric signals. We varied the size of the electrode from five strips of partially overlapping tape to a 0.25 in^2 square, and the signal sizes changed insignificantly. These results are shown for copper in Figure D.2. The only observable change in the signal is greater vibrational noise from the smaller electrodes, which is sensible because larger electrodes adhere to the sample better. To reduce vibrations, we anchored the electrode wire to the YIG with plastic zip-ties.

D.1.3 Electrode Position

Changing the positions of the electrodes on the sample similarly makes very little difference to the symmetric signals. Data from copper electrodes placed at the top, middle, and bottom of the YIG, all still attached to the side, yield essentially identical signals, as shown in Figure D.3. These variations are within the typical range for

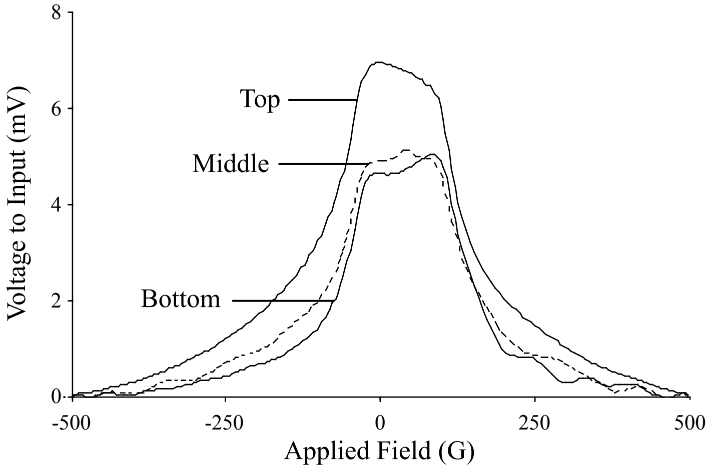

Figure D.3: Symmetric signals from copper electrodes placed at different positions on the YIG cylinder. The signals are essentially identical.

simply reconstructing a given electrode, so we consider these signals identical.

D.1.4 Reproducibility and Aging

One of the major difficulties that we encounter with this sample is the reproducibility of the data. For example, we often constructed electrodes and used them for several days before switching to a different type. We observed that the amplitudes of the symmetric signals decreased over time, though it is not obvious why such change should occur. For example, the M-even effect in the GdIG sample is exactly reproducible over time. Also, the contact that our conductive tape makes with the sample *improves* over time: the tape can be easily removed at first, but after several days we require methanol to clean off acrylic that adheres to the YIG. We hypothesize that the improved bond between the electrode and the YIG may limit the motion of the electrode. These observed decreases in signal size would therefore be analogous to tightening the later braces.

Figure D.4 shows the effects of aging with two different electrodes, over different time spans. The decrease is sudden at first but evidently slows. However, it makes

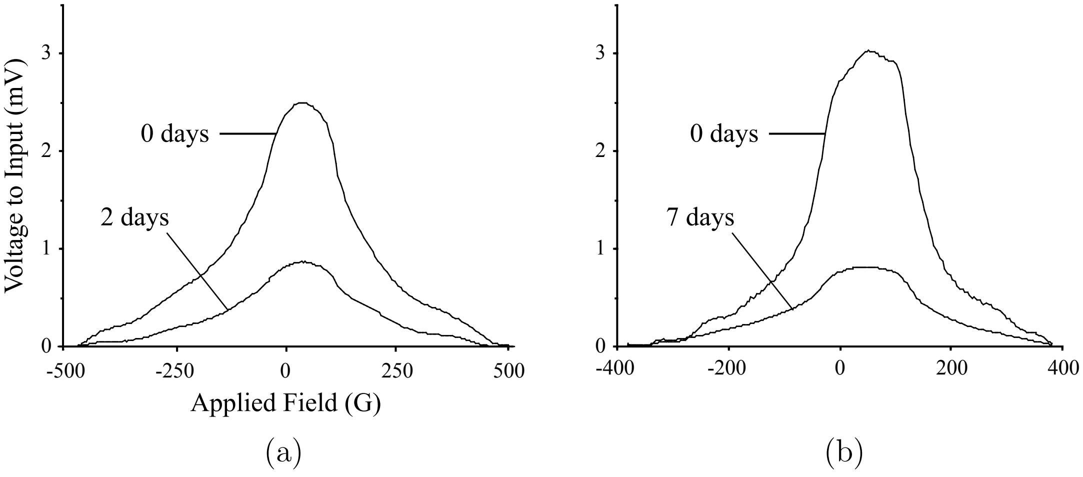

(a) (b)

Figure D.4: Aging of the conductive tape electrodes. (a) 5 strips of Cu tape, (b) 1 strip.

comparing data from different electrodes difficult unless the electrode is freshly constructed; at least then we know that the signal is as large as it ever will be. Because of these difficulties with aging, and the observed changes in how the acrylic sticks to the YIG, we decided to try bonding electrodes to the sample with different adhesives. The first attempt was with silver-doped paint.

D.1.5 Silver Paint

Beyond conductive tape, we also tried bonding a copper electrode to the YIG cylinder with silver paint. The symmetric signal from a 0.5” square, copper electrode silver painted to the sample has a smaller magnitude than the conductive tape signal by approximately a factor of two, but this is insignificant given the variations we routinely observed. Most interestingly, the signal maintained its amplitude over time, as shown in Figure D.5.

We did not try attaching the electrode to the YIG with silver-doped epoxy, as in the main apparatus, because we felt unable to heat safely such a large sample of YIG. Gadolinium and yttrium iron garnets are terrible thermal conductors, and both are extremely sensitive to internal temperature gradients (e.g. our GdIG toroid had to be

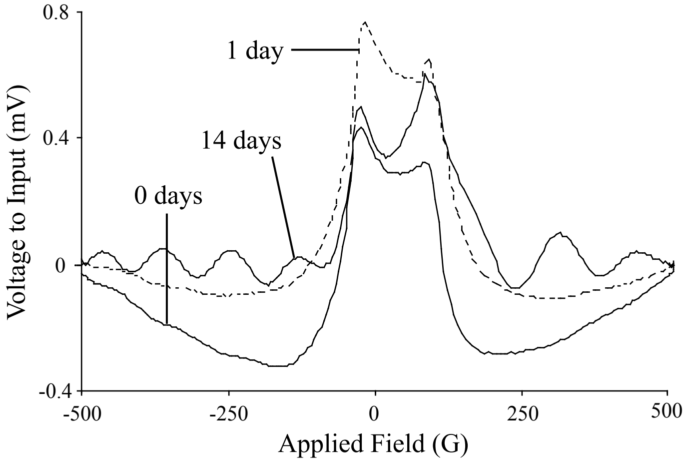

Figure D.5: Symmetric signals from a 0.5” by 0.5” copper electrode, attached mid-sample by silver paint. The signal changes insignificantly over time.

cooled from sintering for two weeks to prevent fracturing). Heating in an oven risks heating the outside of a sample much more rapidly than the inside, which could cause it to crack. We performed epoxy tests on smaller samples of YIG, and the results are discussed in chapter 5.

D.2 YIG Toroids

The second samples that we used were short, YIG cylinders with holes down their centers. We refer to these as toroidal samples, although they are highly irregular. They have 1.5” outer diameters, and are 1.25” and 1.75” tall. Each has one face polished smooth and perpendicular to its axis; we press the samples together at this interface with electrodes between.

D.2.1 Conductive Tape

The first electrodes used with these samples comprised two strips of copper tape with acrylic adhesive on both sides. We placed these parallel between the YIG toroids

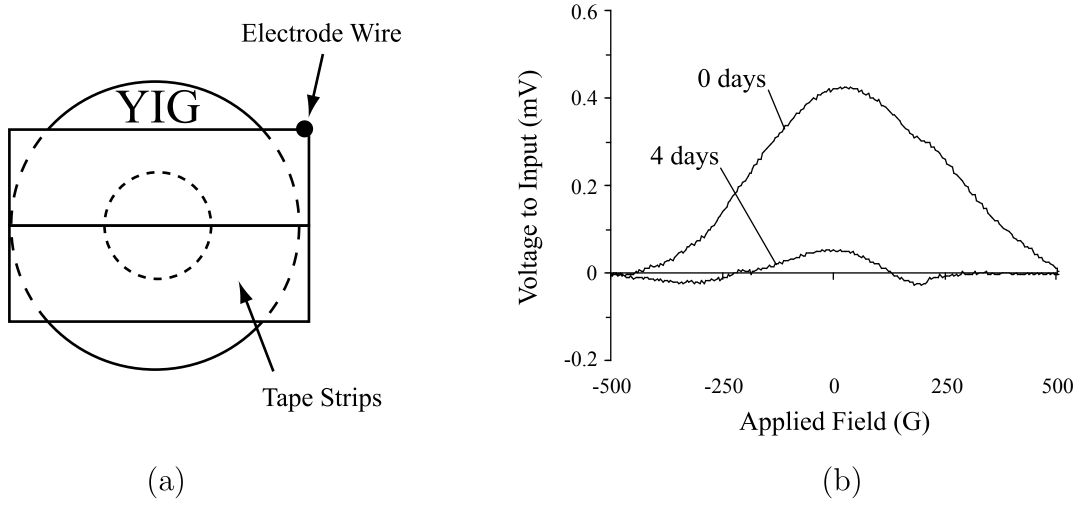

Figure D.6: Symmetric signals from conductive tape between the toroids. (a) The electrodes comprised two strips of copper tape. (b) Aging of the signal.

such that they touched but did not overlap, as in Figure D.6a. The electrode wire was soldered directly to one of the pieces and extended vertically as before. Upon turning on the applied, magnetic field, we observed a symmetric signal of comparable size to those from previous tape measurements.

After allowing the tape to age for four days, we measured the signal again and observed the expected decrease in amplitude. These data are shown in Figure D.6b. In this case, as the tape aged, it became increasingly difficult to separate the samples physically. This supports the hypothesis that the improved bond limits motion between the samples and the electrode, and that this decreases the sizes of the symmetric signals.

D.2.2 Metal Electrodes

Metal electrodes are made from various stocks available around the lab. Most are pure elements, although we also use brass. The materials and their thicknesses are listed in Table 5.1.

The 0.02" copper electrode serves as a control in nearly all experiments because

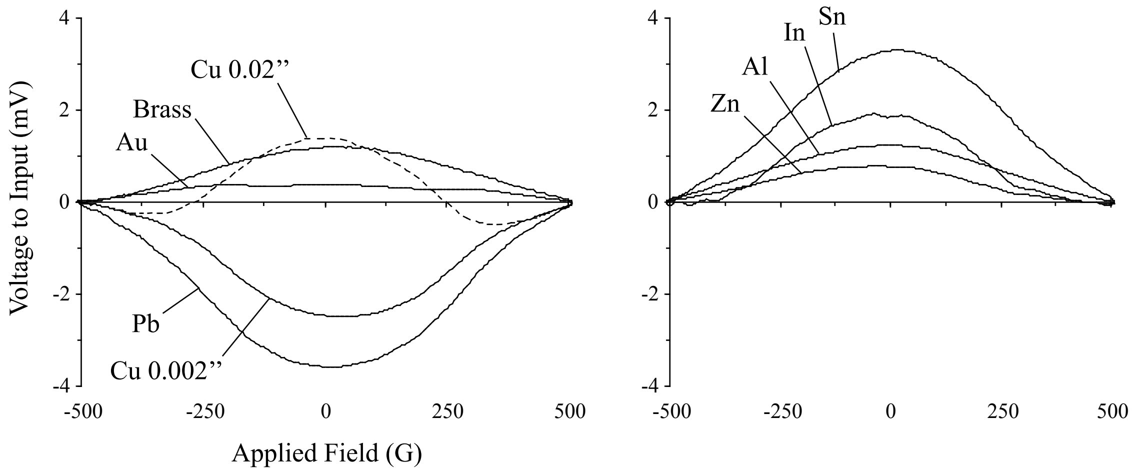

Figure D.7: Symmetric signals from electrodes made of a variety of different metals. Some sign differences are observed.

it is rigid and its signals are reproducibly large. Signals for all these electrodes are shown in Figure D.7. These are best interpreted as *instances* of the signals from these electrodes; often we observe seemingly random sign changes and variations in amplitude. These curves represent a best guess at the most frequent behavior.

Securing electrodes to the indium and tin electrodes is especially difficult because the materials are so soft that they flex under the weight of the electrode wire. Originally we addressed this problem by attaching the electrode wires to the side of the YIG with plastic zip ties, but experiments reveal that this can result in irreproducible changes to the signal shape and sign. The data in Figure D.7 use no zip ties or securing mechanism of any kind, and so differences are likely correlated to the changed electrode.

Two particular qualities of these data are worth noting. First, the signals all have roughly the same size (up to factors of three, or so), and these are quite large. The M-even effect in the GdIG sample has an amplitude of roughly 100 μV, but here the signals are well over 1 mV. Second, some sign changes *have* been observed. Neither of these observations was to be predicted; fundamentally, it is mysterious that we

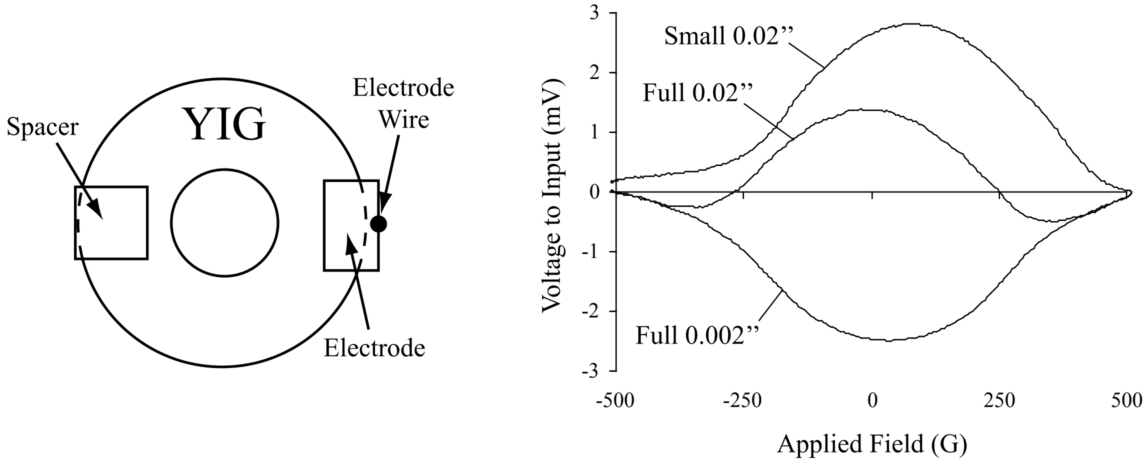

(a) (b)

Figure D.8: Decreasing the size of the electrode between the toroids. (a) A spacer is inserted opposite the electrode to maintain balance. (b) Signals from the electrodes.

observe a symmetric signal in the first place, and further that the signals should vary in this manner.

D.2.3 Size and Thickness

To test the dependence of the symmetric signals on electrode size, we reduced the 1.5” diameter, copper electrode to a 0.5 cm^2 rectangle. This decreases the contact area by a factor of 20. To maintain the vertical geometry and prevent tipping of the toroids relative to each other, we inserted an equally thick, metal spacer across from the electrode, as in Figure D.8a. The signal from this electrode is shown in Figure D.8b; it slightly larger than that from the full electrode.

These data reproduce the two copper electrode curves from Figure D.7 to emphasize the effects of varying the thickness of the electrode. Copper is convenient in this case for we possess a variety of thicknesses, but our stocks of the other materials are limited. In this case, a sign change is observed between the signals from the two copper electrodes, and the signal from the thinner electrode is slightly larger. These differences are frequently observed, yet we lack a sufficient explanation for them.

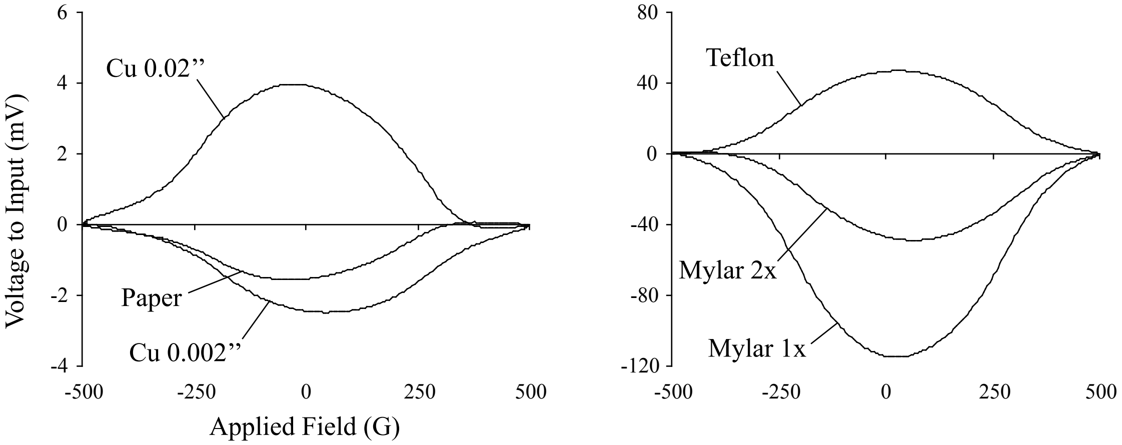

Figure D.9: Signals with various dielectric materials inserted between the electrodes and the YIG. Paper was inserted with a 0.002” copper electrode, and the mylar and teflon with 0.02” copper. The amplitudes of the signals vary by over an order of magnitude.

D.2.4 Dielectrics

To test whether the symmetric signals depend on electrical contact with the YIG, we inserted a small piece of paper on either side of the 0.002” copper electrode. Surprisingly, the signal is barely affected, as Figure D.9 shows. We next tried inserting two sheets of 0.001” mylar above and below the 0.02” copper electrode, for a total of four sheets. The resultant signal is an order of magnitude larger, and of opposite sign, than the signal from the electrode alone. We also tried single sheets of mylar and thick, 0.02” teflon, and observed the largest signals to that point; the single mylar sheet produced a symmetric signal of roughly 120 mV peak-to-peak. These signals are arrestingly large and required complete reconsideration of our models

D.2.5 Brace Pressure Variation

When the pressure applied to the YIG toroids by the brace is decreased, the sizes of the symmetric signals from metal electrodes dramatically increase. The results for a round of these experiments are shown in Figure D.10. We note increases in the

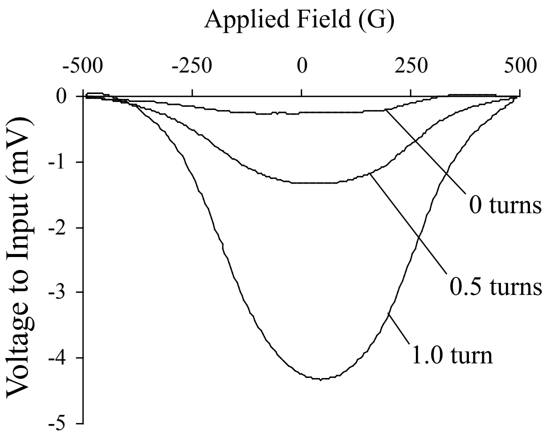

Figure D.10: Signals from a 0.02” copper electrode under varying amounts of brace pressure. Numbers of turns indicate the amount that the two nuts on the top of the brace are loosened; 2.5 turns is the point of no pressure. The amplitudes of the signals vary by over two orders of magnitude.

magnitude of the signal throughout the loosening; when the brace is fully loosened, it increases by over two orders of magnitude.

We find these results to be significant because there is no obvious connection between the pressure applied by the brace and a potential (of any symmetry) on the electrode. However, decreasing brace pressure obviously allows the samples to move more, which suggests a motional EMF source. We had suspected for some time that flipping the magnetization of the GdIG sample might lead to torques and small oscillations, but had not expected significant motion in the model system.

It is worth noting that microphonic noise in the model system is particularly notable with this brace. Simply tapping the outer coil with a finger induces oscillations with amplitudes of several millivolts, and harsher excitations have proportionally greater effects.

D.2.6 Time-Varying Pressure

The most reliable increases in the symmetric signals from the metal electrodes occurred when we progressively loosened the brace. However, each step required unsoldering the electrode wire from the input of the detector, pulling out the inner coil, loosening the brace, and reassembling the whole system. We did our best to limit any other changes that might occur during this reassembly, but one can never be sure. It therefore seemed prudent to develop a system of varying the brace pressure while the system was running.

Professor Hunter suggested hanging a weight on a spring from the top of the brace, and we modified the model system accordingly. A brass plate is placed on top of the toroid brace, with brass bars extending down through the bottom plate of the outer coil. We attach a rod between these bars from which is hung a 4.5 lb weight on a spring; this assembly is shown in Figure D.11. The weight oscillates with a frequency of approximately 2 Hz.

This system produces extremely large, sinusoidal signals on the electrode, as shown in Figure D.12a. Manually pulling the weight produces an immediate negative bump in the signal, which slowly decays to zero with the RC time of the circuit. We also find that large signals are produced if we remove the YIG entirely and replace it with another insulator, such as plastic. One such assembly involves two plastic spacers with pieces of glass, indium-bonded to a 0.002” copper electrode, between them. Dan Krause Jr. bonded the copper to the glass as preliminary work for the indium bonding described in chapter 5, and we borrowed the samples for this test. A photograph of the setup is shown in Figure D.12b. The signal is smaller than that from the YIG, for unknown reasons.

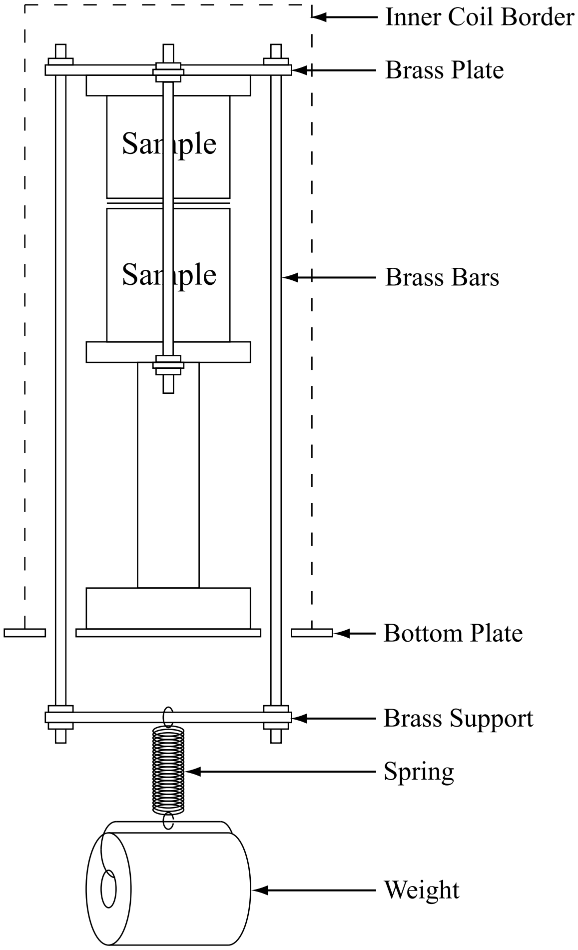

Figure D.11: A hanging weight beneath the model system applies pressure to the top of the brace via brass bars that extend through holes in the bottom plate. The entire system is electrically grounded.

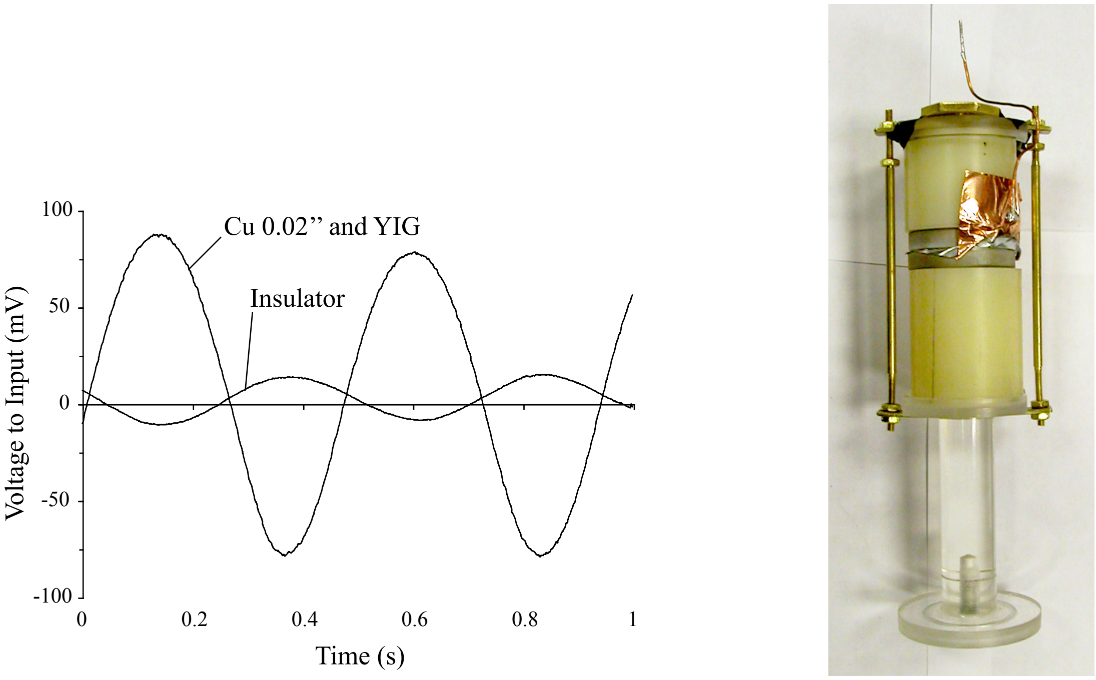

(a) (b)

Figure D.12: Time-varying pressure applied by a weight hanging on a spring. (a) Signals from the electrodes; there is no intended phase relationship between the curves. (b) Photograph of the brace with plastic spacers and a copper electrode indium-bonded to glass.

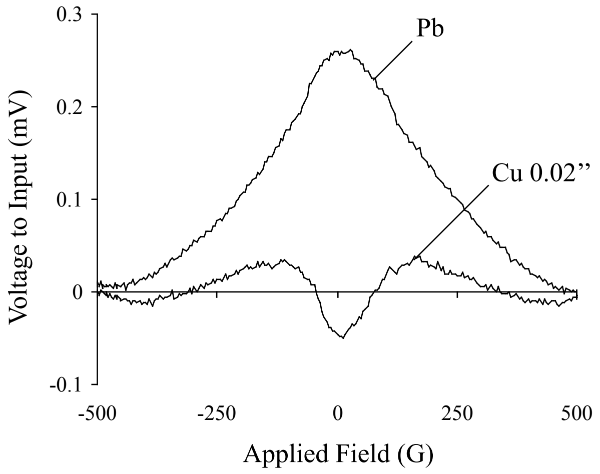

Figure D.13: Symmetric signals from different metal electrodes between ferrites. (a) 0.02" Cu, (b) 0.008" Pb.

D.3 Nickel-Zinc Ferrites

The first brace used to hold the Ni-Zn ferrites is the one designed for the long, YIG cylinder. We first used a mismatched pair of samples, one 3" long and the other 2". The YIG cylinder is 7" long, so we added plastic spacers at either end to account for the shorter overall length. We then repeated some of the tests performed with the YIG toroids, before moving to the entirely new brace designs described in chapter 5.

D.3.1 Electrode Signals

Symmetric signals are observed from metal electrodes compressed between the ferrites, without adhesive. These results are shown in Figure D.13. Their magnitudes are smaller than those observed in previous tests, and the signals tend to decay quickly; both of these observations agree with a decreased *RC* time of the circuit. The lead signal has a familiar shape, but the copper signal is unusual.

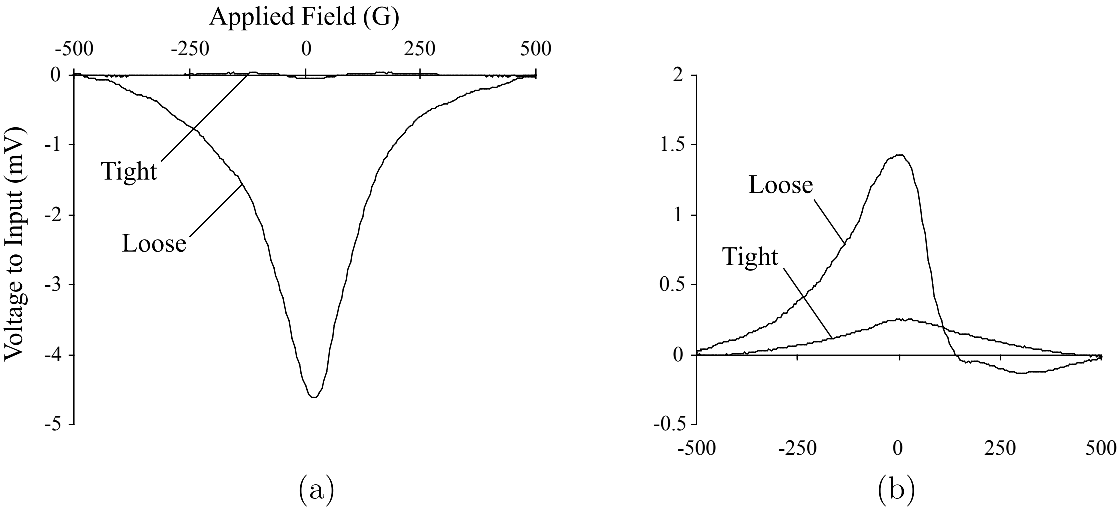

(a) (b)

Figure D.14: Signals from ferrites under variable brace pressure. (a) 0.02” Cu; the signal increases by two orders of magnitude. (b) 0.008” Pb

D.3.2 Brace Pressure Variation

Reducing brace pressure increases the sizes of the symmetric signals from the ferrites, as shown in Figure D.14. The signal from a 0.02” copper electrode increases by two orders of magnitude when the brace is fully loosened, and the lead signal increases by a factor of five. We have since examined the behavior of different electrodes under varying amounts of pressure, and these results are discussed in chapter 5.

D.4 YIG Cylinders

D.4.1 Size and Thickness

To test the dependence of the symmetric signals on electrode size and thickness, we repeated the tests described in §D.2.3 with the YIG cylinders. The data for these tests are shown in Figure D.15a. We note that the signal sizes and shapes are essentially independent of the electrode size and thickness. Loosening the brace on the small electrode produces large, symmetric signals with unusual shapes, as shown in Figure

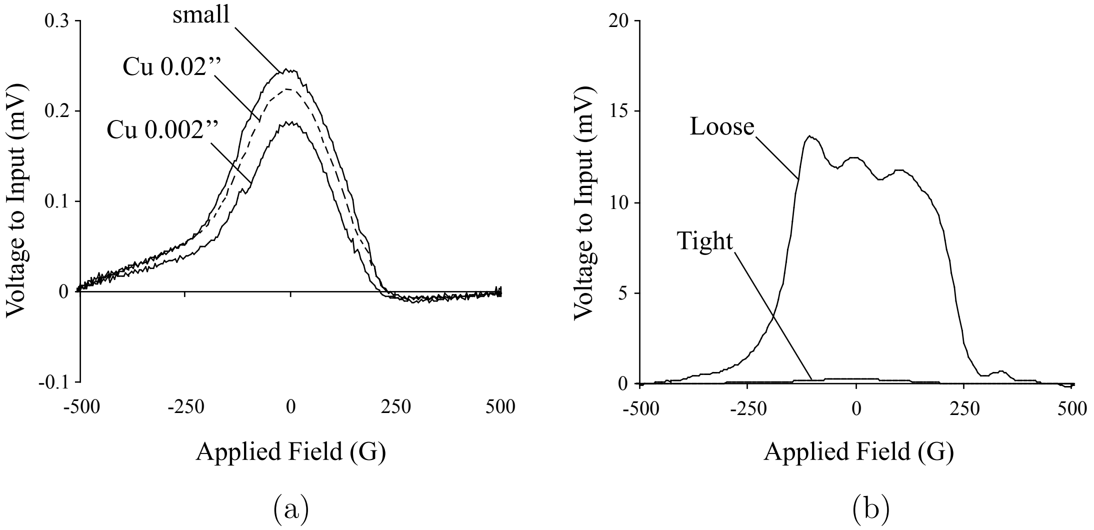

Figure D.15: (a) Signals from copper electrodes of various dimensions. (b) Varying brace pressure on the small, 0.02” Cu electrode.

D.15b. They are almost an order of magnitude smaller than those from full, 0.02” copper electrodes (Figure 5.6a).

D.5 Force Sensors

In addition to the electrode tests described above, we also measured the forces of attraction between various samples during magnetization. To do so, we employed FlexiForce Force Sensors manufactured by Tekscan, Inc. They are long, thin circuits with piezoresistors in a pad on which pressure is applied. The *conductance* (inverse resistance) is linear in the applied force, which allows us to construct a relatively simple circuit to output a voltage linearly proportional to the applied force. A picture of these sensors is shown in Figure D.16.

D.5.1 Sensor and Circuit

The circuit we designed is a modified version of that recommended in [46], and includes a differential amplifier as a second stage to subtract an arbitrary amount of

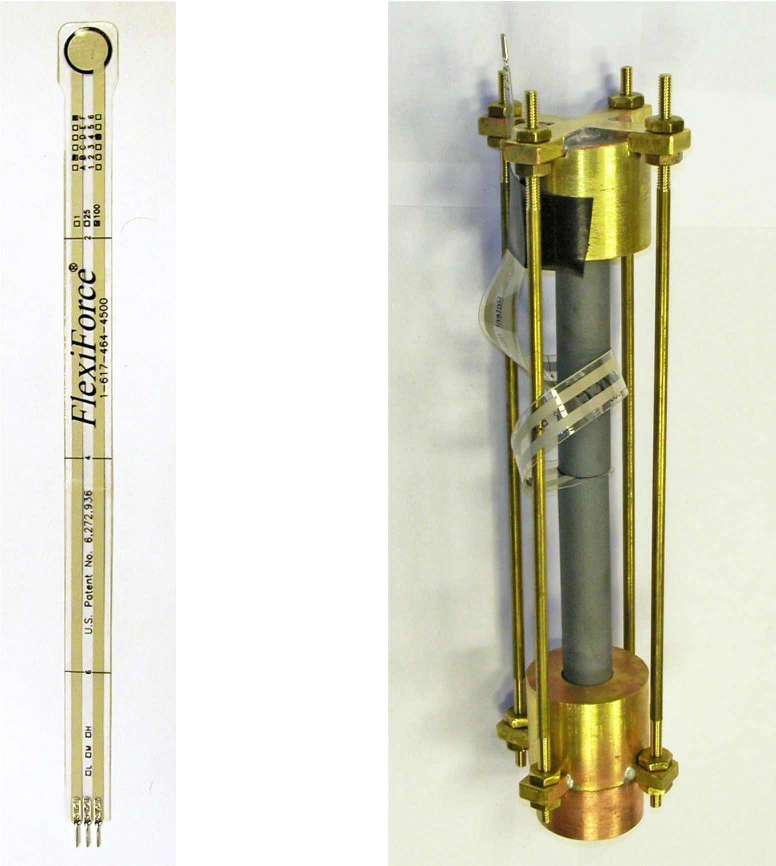

Figure D.16: FlexiForce sensors, shown isolated and mounted between ferrites.

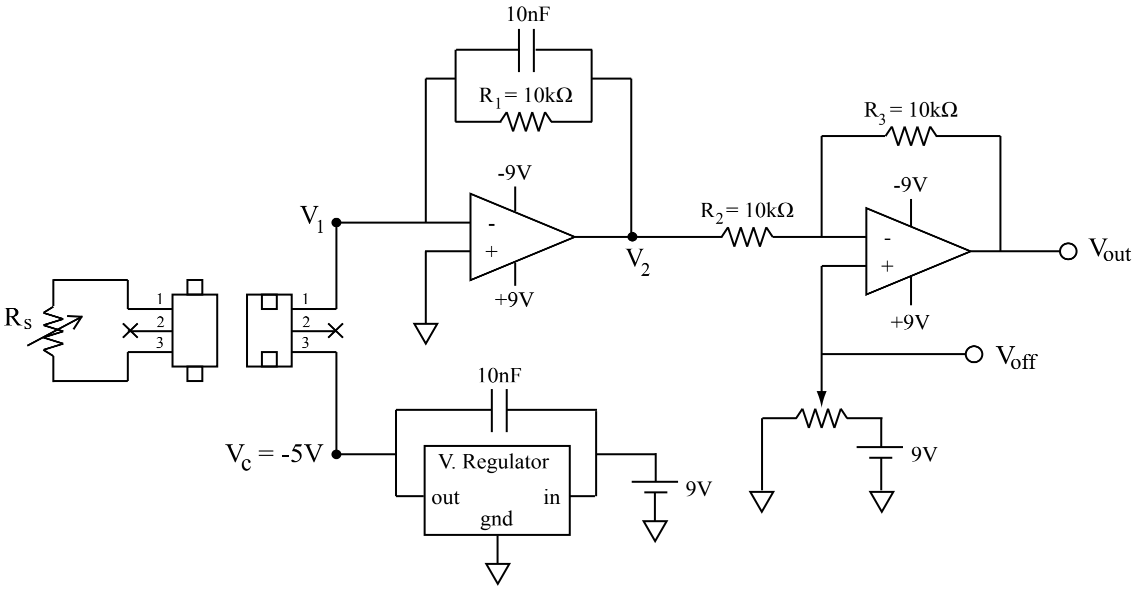

Figure D.17: The circuit built to read the force sensors.

force. Regarding our applications, we may subtract the constant force applied by the brace and see only the change in force due to the changing sample magnetizations. The circuit diagram is shown in Figure D.17. The piezoresistor R_s connects to the circuit via a jack, and the voltage regulator and op-amp maintain a constant voltage drop $V_\mathrm{c} = -5$ V across it. Each op-amp acts as an inverting, differential amplifier; the input voltage to the first op-amp is negative, so the output of the second is similarly negative. The offset voltage V_off is set by a potentiometer and is subtracted in the final stage. Two capacitors are added as low-pass filters to reduce noise.

To calculate the relationship between the applied force and the output, we analyze the circuit directly. (Relevant variables are labeled in the circuit diagram). Analysis of the currents through R_s and R_1 show that V_2 is related to V_c, the constant voltage applied by the voltage regulator, by

$$V_2 = -\frac{R_1}{R_s} V_c. \tag{D.1}$$

The next stage is similar, although the positive input of the second op-amp will not in general be grounded. Applying Ohm's law to R_2 and R_3, we find that V_{out} is given by

$$V_{\text{out}} = \left(1 + \frac{R_3}{R_2}\right) V_{\text{off}} - \frac{R_3}{R_2} V_2 \tag{D.2}$$

Combining this result with Equation D.1, we find V_{out} in terms of V_{c}, as

$$V_{\text{out}} = \left(1 + \frac{R_3}{R_2}\right) V_{\text{off}} + \frac{R_1 R_3}{R_2 R_{\text{s}}} V_{\text{c}}. \tag{D.3}$$

R_1, R_2, and R_3 all equal 10 kΩ, so the relationship simplifies further. As previously mentioned, the force sensors are designed such that the conductance of the piezoresistors is linear in the applied force, which we express as

$$\frac{1}{R_s} = kF, \tag{D.4}$$

where $k \approx 3.1 \times 10^{-5}$ N^{-1}kΩ^{-1} is calculated from manufacturer specifications. After some rearrangement, Equation D.3 therefore simplifies to

$$F = \frac{1}{kR_1V_{\text{c}}}\left(V_{\text{out}} - 2V_{\text{off}}\right) \tag{D.5}$$

and V_{out} is obviously linear in the applied force.

For convenience, we express F as the sum of two forces: a constant force F_b due to the brace, and a changing force ΔF due to the magnetization. When V_{off} is tuned to exactly cancel the potential due to F_b, V_{out} will depend only on ΔF and will vanish when the applied field is off. As the field flips, the force signal that we read is therefore due entirely to the magnetic attraction between the samples. In this case, F_b depends only on V_{off}, and ΔF depends only on V_{out}. We therefore split Equation D.5 into its two contributions and find expressions for the two contributions to the overall force:

$$F_b = -\frac{2}{kR_1V_\mathrm{c}}V_\mathrm{off}, \tag{D.6}$$

$$\Delta F = \frac{1}{kR_1V_\mathrm{c}}V_\mathrm{out}. \tag{D.7}$$

Data collected using the force sensors are analyzed using the above two equations. The force of magnetic attraction is shown in the figures, and F_b is typically given in the captions.

D.5.2 Results from the YIG toroids

We first mounted force sensors between the YIG toroids in their plastic brace. V_off was tuned to subtract the static, brace pressure, and its value was recorded. We then measured the force of attraction of the materials as a function of both applied field strength and brace pressure.

Results from the YIG toroids are presented in this section; pertinent data from the YIG cylinders and ferrites can be found in chapter 5. Because the toroids have holes down their vertical axes, we mounted the force sensor to one side and placed a brass spacer of equal thickness to the sensor (0.007”) on the opposite side. This is shown in Figure D.18a. Data from the sensor for two different brace pressures are shown in Figure D.18b. The changing force is shown here; we assume that the force of attraction does not change the brace pressure.

The samples attract each other with roughly 20N = 4.5 lbs of force close to saturation. We find that the samples display essentially no hysteresis, and so the force of attraction at a given value of the applied field is largely independent of its amplitude. We also note that the amplitude of the attractive force increases as the brace is loosened. The signals begin to plateau at higher field strengths, which we interpret as evidence that the samples nearly saturate in the applied field.

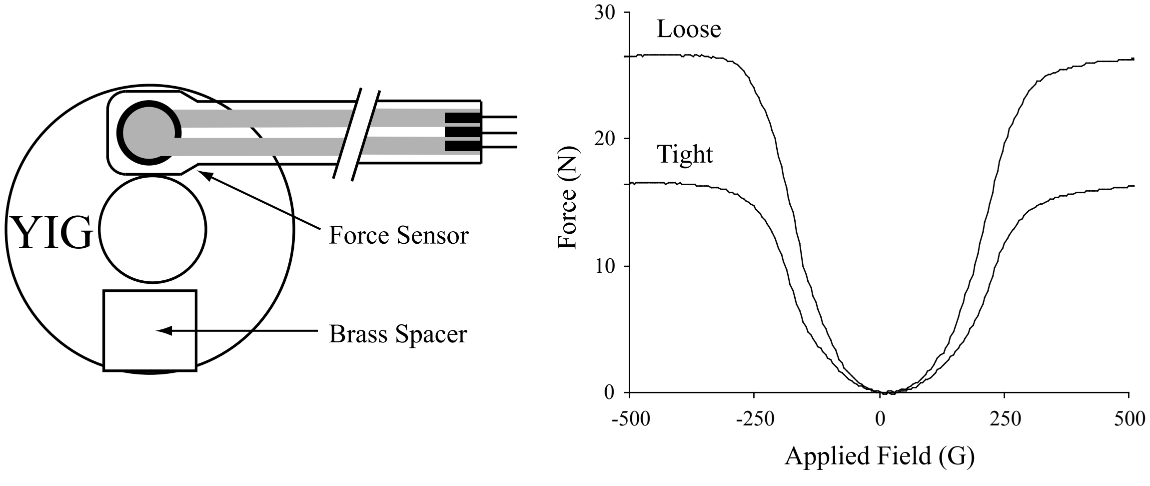

(a) (b)

Figure D.18: Force sensor data from the YIG toroids mounted in their plastic brace. (a) Placement of the sensor. (b) Force of attraction as a function of applied field. The tightened brace provided 1,500 N of pressure, and the loosened brace 350 N.

The data also show that the force of attraction between the samples increases as the pressure from the brace decreases. This is currently not understood; data from the ferrites (Figure 5.11) indicate the opposite trend.

Bibliography

[1] B. J. Heidenreich *et al.*, Phys. Rev. Lett. **95**, 253004 (2005).

[2] B. J. Heidenreich, *Searching for the Electron Electric Dipole Moment Using a Magnetically Polarized Solid* (Undergraduate Thesis, Amherst College, 2005).

[3] J. W. Norbury, Eur. J. Phys. **11**, 99 (1990).

[4] D. J. Griffiths, *Introduction to Elementary Particles* (John Wiley and Sons, 1987).

[5] I. I. Bigi and A. I. Sanda, *CP Violation*, Cambridge Monographs on Particle Physics, Nuclear Physics, and Cosmology No. 9 (Cambridge University Press, 2000).

[6] R. Shankar, *Basic Training in Mathematics* (Plenum Press, 1995).

[7] D. J. Griffiths, *Introduction to Quantum Mechanics*, 2nd ed. (Pearson Prentice Hall, 2005).

[8] L. E. Ballentine, *Quantum Mechanics: A Modern Development* (World Scientific, 1998).

[9] T. D. Lee and C. N. Yang, Phys. Rev. **104**, 254 (1956).

[10] C. S. Wu, E. Ambler, R. W. Hayward, D. D. Hoppes, and R. P. Hudson, Phys. Rev. **104**, 1413 (1957).

[11] T. D. Lee, R. Oehme, and C. N. Yang, Phys. Rev. **106**, 340 (1957).

[12] I. Khriplovich and S. Lamoreaux, *CP Violation Without Strangeness* (Springer-Verlag, 1997).

[13] D. J. Griffiths, *Introduction to Electrodynamics*, 3rd ed. (Pearson Prentice Hall, 1999).

[14] W. W. Havens, I. I. Rabi, and L. J. Rainwater, Phys. Rev. **22**, 634 (1947).

[15] E. M. Purcell and N. F. Ramsey, Phys. Rev. **78**, 807 (1950).

[16] J. H. Smith, E. M. Purcell, and N. F. Ramsey, Phys. Rev. **108**, 120 (1957).

[17] P. G. Harris *et al.*, Phys. Rev. Lett. **82**, 904 (1999).

[18] B. C. Regan, E. D. Commins, C. J. Schmidt, and D. DeMill, Phys. Rev. Lett. **88**, 71805 (2002).

[19] B. V. Vasil'ev and E. V. Kolycheva, Sov. Phys. JETP **47**, 243 (1978).

[20] S. Lamoreaux, Phys. Rev. A **66**, 022109 (2002).

[21] L. I. Schiff, Phys. Rev. **132**, 2194 (1963).

[22] P. G. H. Sandars, Phys. Lett. **14**, 194 (1965).

[23] S. A. Murthy, D. Krause, Z. L. Li, and L. R. Hunter, Phys. Rev. Lett. **63**, 965 (1989).

[24] C. W. Chen, *Magnetism and Metallurgy of Soft Magnetic Materials* (Dover Publications, 1986).

[25] E. E. Anderson, J. J. Richard Cunningham, and G. E. McDuffie, Phys. Rev. **116**, 624 (1959).

[26] C. Kittel, *Introduction to Solid State Physics*, 6th ed. (John Wiley and Sons, 1986).

[27] D. V. Schroeder, *An Introduction to Thermal Physics* (Addison Wesley Longman, 2000).

[28] L. Néel, R. Pauthenet, and B. Dreyfus, *The Rare Earth Garnets* (North-Holland, 1964).

[29] N. Fortson, P. Sandars, and S. Barr, Physics Today , 33 (2003).

[30] T. N. Mukhamedjanov, V. A. Dzuba, and O. P. Sushkov, Phy. Rev. A **68**, 042103 (2003).

[31] S. A. Kuenzi, O. P. Sushkov, V. A. Dzuba, and J. M. Cadogan, Phy. Rev. A **66**, 032111 (2002).

[32] S. Chikazumi, *Physics of Magnetism* (John Wiley and Sons, 1964).

[33] NAIS, Matsushita Electric Works, *PhotoMOS Relays Spec Sheet*, 2001.

[34] W. F. Brown, Phys. Rev. **58**, 736 (1940).

[35] Deltronic Crystal, *Yttrium Iron Garnet Advanced Material Datasheet*, URL: http://www.temlaser.com/Yttrium_Iron_Garnet.pdf. Accessed May 8, 2007.

[36] Burr-Brown, Inc., *INA116: Ultra Low Input Bias Current Instrumentation Amplifier*, 1994. URL: http://focus.ti.com/lit/ds/symlink/ina116.pdf. Accessed May 8, 2007.

[37] P. G. H. Sandars, Contemporary Physics **42**, 97 (2001).

[38] W. Bernreuther and M. Suzuki, Rev. Mod. Phys. **63**, 313 (1991).

[39] P. A. M. Dirac, *The Principles of Quantum Mechanics*, 4th ed. (Oxford University Press, 1958).

[40] P. G. H. Sandars, J. Phys. B (Proc. Phys. Soc.) **1**, 499 (1968).

[41] P. G. H. Sandars, J. Phys. B (Proc. Phys. Soc.) **1**, 511 (1968).

[42] P. Horowitz and W. Hill, *The Art of Electronics*, 2nd ed. (Cambridge University Press, 1989).

[43] K. Lacanette, *A Basic Introduction to Filters - Active, Passive, and Switched-Capacitor*, National Semiconductor, 1991.

[44] Burr-Brown Inc., *Universal Active Filter UAF42 Spec. Sheet*, 1990. URL: http://focus.ti.com/lit/ds/symlink/uaf42.pdf. Accessed May 8, 2007.

[45] D. R. Lide, editor, *CRC Handbook of Physics and Chemistry*, 87th ed. (Taylor and Francis, 2006).

[46] Tekscan, Inc., *FlexiForce Force Sensors*, URL: http://www.tekscan.com/flexiforce/flexiforce.html. Accessed April 15, 2007.